BEARING WORLD

www.bearingworld.org

Journal

Volume 8_2024

Editors: G. Poll _ B. Pinnekamp _ C. Kunze

FVA
sharing drive innovation

VDMA Verlag

Imprint

Bearing World Journal
Volume 8, December 2024

Published by:
Forschungsvereinigung Antriebstechnik e.V. (FVA)
Lyoner Straße 18
60528 Frankfurt am Main
Germany
www.fva-net.de

© 2024
VDMA Services GmbH
Lyoner Straße 18
60528 Frankfurt am Main
Germany
www.vdma-verlag.com

All rights reserved, particularly the right of duplication and disclosure, as well as translation. No part of the work may be reproduced in any form (print, photocopy, microfilm or any other method) without written consent from the publisher or saved, processed, duplicated or disclosed.

Online-ISSN 2566-4794

Volume 8_2024

Dear reader,

Globalization increasingly requires more and more international networking between research and development engineers. In response to this, the German Research Association for Drive Technology (FVA) launched the first Bearing World conference in 2016. With that inaugural meeting, the FVA initiated a very fruitful international dialogue in which researchers and developers from universities and bearing manufacturers came together with users and experts from the industry.

The Bearing World Journal, which is published annually, serves to foster exchange between international experts during non-conference years by featuring peer-reviewed, high-quality scientific papers on rolling element bearings as well as plain bearings. As an international expert platform for publishing cutting-edge research findings, the journal intends to contribute to technological progress in the field of bearings.

We are now starting to prepare the 2025 edition of Bearing World Journal and are looking forward to new contributions from the scientific and industrial communities. We would like to thank all authors for their fascinating contributions to Bearing World Journal No. 8.

_ **Prof. Dr.-Ing. Gerhard Poll,** **Initiator, Head of international Scientific Board**
_ **Dr.-Ing. Burkhard Pinnekamp,** **President of the FVA Management Board**
_ **Christian Kunze,** **Editor-in-chief**

Please send the paper you intend to publish in the next issue of the Bearing World Journal via e-mail as Word document to FVA (**submission@bearingworld.org**).
In addition please attach a PDF document.

Bearing World Scientific Board

Scott Bair, Georgia Institute of Technology, USA
Prof. Harry Bhadeshia, University of Cambrigde, Great Britain
Prof. Stefan Björklund, KTH Royal Institute of Technology, Stockholm, Sweden
Prof. Benyebka Bou-Said, Institut National Des Sciences Appliquées (INSA) Lyon, France
Prof. Bernd Bertsche, Universität Stuttgart, Germany
Prof. Ludger Deters, TU Magdeburg, Germany
Prof. Duncan Dowson, University of Leeds, Great Britain (†)
Prof. Rob Dwyer-Joyce, University of Sheffield, Great Britain
Prof. Michel Fillon, Université de Poitiers, France
Prof. Sergei Glavastkih, KTH Royal Institute of Technology, Stockholm, Sweden
Prof. Irina Goryacheva, Russian Academy of Sciences, Russia
Prof. Feng Guo, Qingdao Technological University, China
Prof. Martin Hartl, Brno University of Technology, Czech Republic
Prof. Stathis Ioannides, Imperial College London, Great Britain
Prof. Georg Jacobs, RWTH Aachen University, Germany
Prof. Michael M. Khonsari, Louisiana State University, USA
Prof. Ivan Krupka, Brno University of Technology, Czech Republic
Prof. Roland Larsson, Luleå University of Technology, Sweden
Prof. Antonius Lubrecht, Institut National Des Sciences Appliquées (INSA) Lyon, France
Prof. Piet Lugt, SKF Nieuwegin; University of Twente, Enschede, Netherlands
Prof. Jianbin Luo, State Key Laboratory of Tribology, Tsinghua University, China
Prof. Guillermo Morales-Espejel, INSA Lyon, France
Prof. Anne Neville, University of Leeds, Great Britain (†)
Prof. Hiroyuki Ohta, Nagaoka University of Technology, Japan
Prof. Gerhard Poll, Leibniz University Hanover, Germany
Prof. Martin Priest, University of Bradford, Great Britain
Prof. Farshid Sadeghi, Purdue University, Lafayette, Indiana, USA
Prof. Richard Salant, Georgia Institute of Technology, USA
Prof. Bernd Sauer, TU Kaiserslautern, Germany
Prof. Ian Sherrington, University of Central Lancashire, Great Britain
Prof. Hugh Spikes, Imperial College London, Great Britain
Prof. Gwidon Stachowiak, Curtin University Australia, Australia
Prof. Kees Venner, University of Twente, Enschede, Netherlands
Prof. Philippe Vergne, Institut National Des Sciences Appliquées (INSA) Lyon, France
Prof. Fabrice Ville, Institut National Des Sciences Appliquées (INSA) Lyon, France
Prof. Sandro Wartzack, Friedrich-Alexander-University Erlangen-Nürnberg, Germany
Prof. John A. Williams, University of Cambridge, Great Britain
Prof. Hans-Werner Zoch, IWT Stiftung Institut für Werkstofftechnik, Bremen, Germany

Contents

Low-Friction Surface Engineering for Railway Wheel-End Bearings
Victor Brizmer, SKF Research & Technology Development, The Netherlands 7

Approach towards the condition monitoring of journal bearings using surface acoustic wave Technology
Thomas Decker, Center for Wind Power Drives/ RWTH Aachen University, Germany 15

A Simple and Novel Method Determining the Suitability of a Grease Related to the White Etching Crack Phenomenon
Saba Mottaghi, TUNAP GmbH & Co. KG, Wolfratshausen, Germany 25

Novel analytical calculations in truncated point contact including misalignment
Luc Houpert, Wettolsheim, France 31

Tool chain for wear prediction of journal bearings in planetary gears in wind turbines
Benjamin Lehmann, Institute for machine elements and systems engineering/ RWTH Aachen University, Germany 63

Influence of deep rolling process at various temperatures on the fatigue life of rolling bearings
Simon Dechant, Leibniz Universität Hannover, Germany 77

Low-Friction Surface Engineering for Railway Wheel-End Bearings

Victor Brizmer, Esteban Broitman, Arnaud Ruellan, Ralph Meeuwenoord, Daan Nijboer, Roel van der Zwaan

SKF Research & Technology Development, 3992 AE Houten, The Netherlands

---

Abstract

To achieve the challenging environmental goals facing the railway market, wheel-end bearing units are being optimized to reduce power losses in operation without compromising reliability and maintenance interval. One of the different technical solutions to reduce friction in railway roller bearing units is the selection of the optimum surface coating for the bearing components. Today, inner and outer rings of railway bearing units are coated with chemical conversion layers designed specifically for anti-corrosion, anti-fretting and mounting properties but not optimized for friction reduction in the internal contacts. In the present study, frictional performance of different coatings and conversion layers (tribological black oxide, zinc-calcium phosphate, and manganese phosphate) has been compared to that of uncoated steel surface, based on full-bearing grease-lubricated tests ran under operating conditions relevant for railway application. Results demonstrate that the same optimum conversion layer can reduce the running torque by above 30% compared to the current products both at low and intermediate speeds relevant to intercity trains. Extra analysis shows that beneficial running-in properties of the conversion layers, governed by the hardness and roughness differentials of the contacting surfaces, dominate the friction reduction potential. It is also verified that the running-in wear of the soft conversion layers does not affect the reliability of the bearing units if applied to the rougher or both contacting surfaces. For this purpose, wear and surface distress screening tests were performed on a micropitting rig as well as dedicated grease ageing tests with conversion layer particle contamination.

Keywords – railway wheel-end bearings; conversion coating; manganese phosphate; black oxide; zinc-calcium-phosphate; friction; wear; surface distress.

---

1. Introduction

To meet the environmental requirements, the global railway market aims to half the final energy consumption and specific average CO_2 emissions from train operations by 2030 (vs 1990 baseline) [1]. For this reason, wheel-end bearing units are being optimized to reduce power losses in operation without compromising the other performance aspects that could influence the maintenance interval.

Among multiple potential solutions to reduce friction in railway bearing units (e.g., optimization of bearing contact, cage geometry, seal design, lubricant selection), low-friction surface engineering (including topography and coating) for the rings and/or rolling elements seems to be one of the most promising. There exist multiple types of coatings that can be used in rolling bearings [2] but only a few of them can be used on the raceways [3].

An example of raceway-applicable coatings is a group of them known as "conversion coatings" [4], which are produced by converting the bearing metallic surfaces into a coating by conducting electrolytic or non-electrolytic chemical reactions under specific conditions. These conversion coatings have been employed for quite a long time to prevent corrosion of metal parts and, when applied in lubricated tribological contacts, can also mitigate adhesive wear, enhance fatigue resistance, and reduce friction [5], [6].

The most commonly used types of conversion coatings on steel bearing substrate are phosphates and oxides that usually have rough and sometimes porous surface structure which facilitates adsorption of liquid lubricant. This mechanism is believed to enhance the corrosion protection and to promote the other abovementioned tribological benefits of conversion coatings [4].

The bearing phosphating conversion process includes several immersion steps in which the coating is created by chemical reactions where the iron on the surface reacts with manganese, zinc, or zinc-calcium cations, and the phosphate anions in the fluid. Addition of calcium to the zinc produces a smoother layer with smaller grains, providing properties more suitable to rolling/sliding contacts [2], [7]. When used for bearing applications, manganese phosphate (MnPh) or zinc-calcium phosphate (ZnCaPh) coatings have a thickness in the range of 2-15 μm [2], [8].

Another bearing conversion process, black oxidation, is also the result of a chain of chemical reactions with immersion of the bearing steel surfaces in different warm alkaline aqueous salt solutions. The reactions between the iron of the steel surface and the reagents produce a black layer, approximately 1 μm thick, consisting of a blend of FeO, Fe_2O_3, and Fe_3O_4 [9]. The total process consists of about 15 different immersion steps, in many of which it is possible to vary chemical contents, concentrations, temperatures, immersion times, and fluid behavior within the tanks, defined in DIN 50938 [10] and equivalent ISO 11408 [11]. In our experiments, we will use a "tribological black oxide" (TBO) coating, produced according to the proprietary production specifications in order to tailor the coating for optimum tribological behavior in rolling bearing applications [2].

Many of the published studies that address the tribological properties of black oxide, zinc-based phosphate, and manganese phosphate conversion coatings, are based on tests carried out in pure sliding conditions (see literature review in [8]) that do not represent the kinematics of rolling element bearing contacts.

There are several publications addressing the frictional performance and other tribological aspects of black oxide [8], [9], [12], [13] manganese phosphate [8], [14], [15] and zinc-calcium-phosphate [8] layers by carrying out different tests under rolling/sliding contact conditions.

The micropitting and wear performance of TBO in rolling/sliding contacts, lubricated with base oil or oil/additive solution, was studied in [9] and [12], respectively. It was observed that, under certain conditions, TBO can mitigate the micropitting accumulation, and it does not have negative impact on the total wear.

In the current study, three different conversion layers (ZnCaPh, MnPh, and TBO, see general properties in Table 1), are compared with each other and with reference uncoated steel samples concerning their friction performance. This comparison is based on experimental results of grease-lubricated double-row CRB friction rig tests under conditions typical for railway bearing application. Moreover, possible influence of these conversion layers on the bearing maintenance interval has been verified using micropitting and wear MPR component tests and grease ageing tests.

Table 1: Chemical composition and thickness of the layers used in the present study

Layer	Chemical composition	Thickness
TBO	Tribological Black Oxide FeO, Fe_2O_3, Fe_3O_4	~1 µm
ZnCaPh	Zinc Calcium Phosphating $Zn_3(PO_4)_2CaZn_2(PO_4)_2$	~5 µm
MnPh	Manganese Phosphating $(Mn,Fe)_5(PO_4)_2(PO_3OH)_2$	~10 µm

2. Experimental details

A full-bearing in-house test rig, shown schematically in Figure 1, designed to measure bearing friction torque under various speed and load conditions, has been employed to compare the different conversion layers under test conditions close to those in intercity train wheel-end bearing units [8].

Since wheel-end bearing units are typically double-row units, the tests were performed with a double CRB (cylindrical rolling bearing) setup (NU2207 ECP/C3 and NJ 2207 ECP/C3). The roller sets were kept with original rings to maintain C3 clearance. Before testing, every bearing was filled with 2.5 g of a typical railway grease providing the same initial grease distribution.

The overall test conditions for this study are specified in Table 2. In general, the test profiles are used by varying either the rotation speed or the axial load. The radial load has been set to reach contact pressures of 1.3 GPa and 1 GPa, respectively, on the inner (IR) and outer ring (OR).

The axial load for the speed cycles was set to reach 200 MPa on the flange contact. The speed cycle has been designed to represent typical linear speeds obtained in intercity railway wheel-end units and in order to minimize the effect of grease movements on the measured torque. The axial load cycle has been designed to assess the flange contribution yet staying below the maximum recommended axial-to-radial load ratio.

In this test campaign, the inner and outer rings of the bearings were either uncoated or coated with one of the conversion layers, while the rollers were kept uncoated.

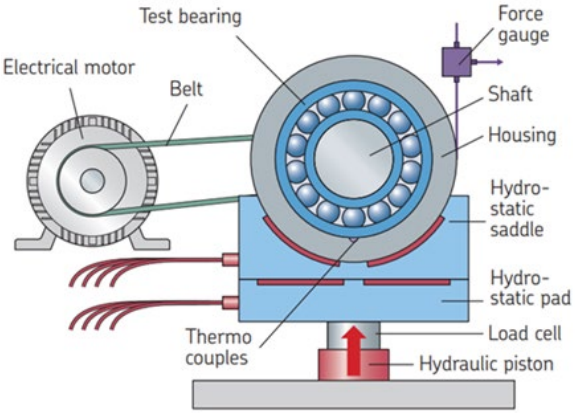

Figure 1: Schematics of the full bearing test rig, used in the present study [8]

Table 2: Summary of full-bearing testing conditions

Bearings	**NU2207 + NJ2207**
Radial load (N)	7000
Axial load (N)	100-1000
Lubrication	Railway Grease (PAO base oil ISO VG100)
Temp (°C)	60
Speeds	from 300 to 4500 rpm with 0.5 hrs CW and 0.5 hrs CCW
Repeats	Speed cycle repeated minimum 7 times

To investigate the possible influence of conversion layers on the maintenance interval by affecting the surface distress and/or wear resistance, a micropitting test rig (MPR, produced by PCS Instruments, UK) was used in the present study. The principal part of the MPR is its load unit which consists of three rings in contact with a small roller in the middle, rotating with fixed sliding in oil-lubricated conditions, as shown in Figure 2.

This contact design forces the roller to accumulate fatigue macro-cycles 13.5 times faster than any of the three rings during the test. Moreover, contacting surfaces of the rings are transversely grinded to facilitate the accumulation of micropitting on the roller that was polished to create a tenfold roughness differential (typically, the R_q roughness values are 50nm and 500nm for the roller and the rings, respectively) between the contacting surfaces (before applying the conversion layer on one or both of them). Under these conditions, the roller becomes much more exposed to micropitting than its larger and rougher contact mates [16].

The MPR tests were designed in such a way to provide mixed lubrication during the test and to be with the maximum Hertzian contact pressure typical for railway wheel-end bearing units.

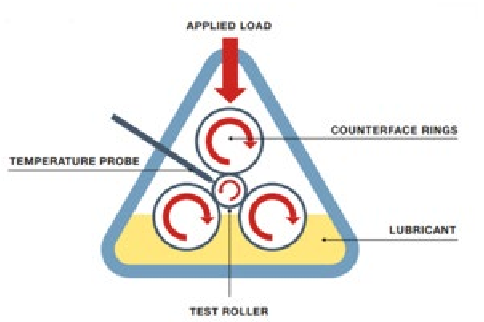

Figure 2: MPR – schematics of the load unit.

3. Results and discussion

The microstructural aspects and mechanical characteristics of the three conversion layers, their influence on the frictional torque in the dedicated full bearing tests and evaluation of their possible influence on the bearing maintenance interval (concerning the micropitting, wear, and grease ageing aspects) will be discussed separately, in three sections of the present Chapter.

3.1. Morphology and mechanical properties of the conversion layers

SEM images with typical morphology of the three conversion layers are presented in Figure 3.

The TBO coating (Figure 3(a)) shows presence of voids and cracks that can be attributed, respectively, to the nature of the oxide conversion process and to the fact that the TBO has a different thermal expansion coefficient than the steel substrate (see discussion in [8]). The ZnCaPh coating (shown in Figure 3(b)) has a compact microstructure with a uniform distribution of grains (thanks to the incorporation of calcium during the phosphating process), while the MnPh coating (see Figure 3 (c)) has a polycrystalline microstructure with prismatic-shaped crystals with a typical size of 5-10μm [8].

The hardness and the reduced Young's moduli of the three conversion layers, obtained by nano-indentation [8], are shown in Table 3 in comparison with the mechanical properties of the reference AISI 52100 bearing steel. It can be seen that all the conversion layers are much softer and less stiff than the steel. This could imply enhanced running-in of the coated surfaces and mitigated contact stresses in the near-surface zone.

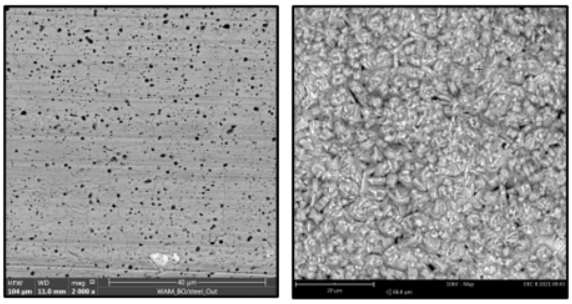

(a) TBO (b) ZnCaPh

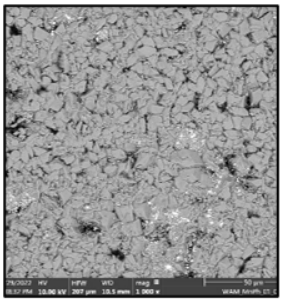

(c) MnPh

Figure 3: SEM images showing typical morphology of the three conversion coatings: (a) TBO, (b) ZnCaPh, (c) MnPh. Note that the magnification in (b) is half the magnification in the other images.

Table 3: Mechanical properties of the conversion layers vs the reference AISI 52100 steel [8]

	H, GPa	E_r, GPa
Steel	8.98 ± 0.97	197.6 ± 8.4
TBO	2.5 ± 1.1	71 ± 22
MnPh	1.49 ± 0.44	88 ± 14
ZnCaPh	2.73 ± 0.79	58 ± 11

3.2. Full bearing tests

The relative average bearing torque, obtained from the full-bearing speed cycle tests (see test rig in Figure 1), is presented in Figure 4 for various speeds within the bearing friction speed cycle under constant axial load of F_a=250N (except the last step under F_a=100N). The torque is normalized with respect to that for uncoated steel bearings at 3,1krpm and represents the average values of at least 9 speed cycle repeats (see actual R-numbers on the right). It should be mentioned that the duration of each speed step was 1 hour (i.e., 6 hours per speed cycle) and that these measurements were taken after the initial running-in stage of 10 hours.

Notice in Figure 4 that the use of the TBO (black columns) leads to prominent and consistent friction reduction compared to the reference all-steel case (grey columns) throughout the speed cycle. This friction reduction is more prominent at lower speeds, ranging from about 30% at 4,5krpm to 50% at 0,3krpm.

ZnCaPh coating (blue columns) shows less consistent friction reduction than the TBO, while MnPh (green columns) does not reduce the torque compared to the all-steel case case.

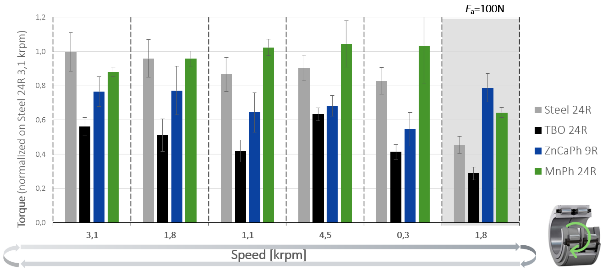

* R = number of repeats of speed cycles → Std deviation bars around average torque of R repeats

Figure 4: Relative average torque for different speeds within the bearing friction speed cycle at F_a=250N (if not stated otherwise)

After the tests, the roughness of the bearing raceways was scanned by using light interferometry microscope, and the corresponding results are presented in Table 4 in dimensionless form, normalized with respect to the reference R_a value of untested steel rings without conversion layer.

Data presented in Table 4 imply that the friction reduction with TBO, seen in Figure 4, can be explained by the enhanced running-in ability: there is a 52% reduction in the R_a value on the TBO coated surface vs. 29% reduction on the raceway steel surface in the all-steel bearing under identical conditions. This observation also explains why the TBO benefits reduce at higher speeds, where the larger film thickness separates the solid surfaces in a better way.

The corresponding R_a reduction on the flange track is 25% for the TBO whereas the steel flange surface does not show any signs of run-in.

For the other conversion layers, the R_a / $R_{a\text{-ref}}$ ratios were above one in all the cases, meaning that the initial surface roughening due to the coating process has not been compensated by the running-in.

Table 4: Surface roughness R_a measured inside the inner ring raceway and flange tracks after testing, normalized vs. the reference R_a of "virgin" steel rings, prior to coating

Surface	Raceway track, R_a / $R_{a\text{-ref}}$	Flange track, R_a / $R_{a\text{-ref}}$
Steel	0,71	1,07
MnPh	1,49	1,68
ZnCaPh	1,40	1,41
TBO	0,48	0,75

In Figure 5, the results of load cycles at constant speed (of 1,8krpm) are presented, demonstrating the influence of the axial load on torque reduction effect of the TBO vs. the reference all-steel bearings, for 2 different greases, used as the lubricant (standard and low-friction). It is apparent that in the case of all-steel bearing, the frictional torque grows almost linearly with the axial load, underlining the flange contact contribution [8]. The fivefold increase in F_a from 0,2kN to 1kN results in about fourfold increase in the torque with both the standard and the low-friction grease (the grey and the light brown columns, respectively). It can also be seen that the low-friction grease gives 25-30% friction reduction, compared to the standard one, for all-steel bearings. On the other hand, with the TBO (black and dark brown columns for standard and low-friction grease, respectively), the frictional torque only slightly increases with the axial load. It can be seen that the use of TBO results in friction reduction from 50% at lower loads to 75% at higher loads, compared to all-steel bearing with standard grease. It is obvious that, from torque reduction viewpoint, applying the TBO gives more prominent effect than using a low-friction grease [8].

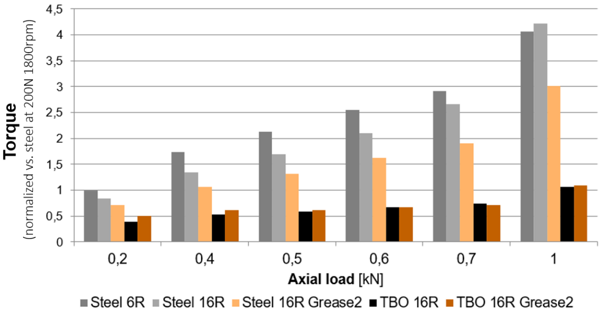

* Same bearing used for both greases with regreasing in between 2 tests.
** 16 repeats per average point (with avg std deviation of 14% for all points)
*** Grease2 known to provide lower friction under such conditions

Figure 5: Relative average frictional torque for different axial loads at 1800 rpm

The results in Figure 5 imply the relative torque values averaged over 6 or 16 load cycles (see legend below the Figure). An important question that remains to be answered if the TBO gives stable and consistent friction reduction, i.e., if the torque does not change much from cycle to cycle and if it does not increase towards the end of the test.

The results of Figure 5 are replotted in Figure 6, showing the time evolution of the dimensionless torque, from cycle to cycle, instead of its average value. As can be seen, with the TBO (right) the torque is even more stable than in the reference all-steel bearings (left), within the whole tested range of the axial loads (from 0,4kN to 1,0kN), for both greases.

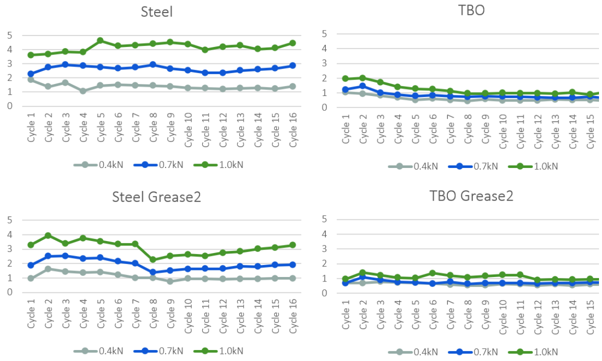

Figure 6: Time evolution of relative frictional torque for different axial loads at 1800 rpm

3.3. Beyond friction – other tribological aspects

Low-friciton solutions do not make practical sense if they compromise the other tribological performance or lubrication aspects that can negatively influence the bearing maintenance interval. These aspects could imply increased risk of surface-initiated fatigue (micropitting), reduced antiwear resistance or acceleration of grease ageing due to the presence of conversion layer. To evaluate possible influence of the considered coatings on these performance factors, special component and lubricant tests were carried out in the present study.

The MPR wear test results, showing the mass loss of the steel roller during the test, in contact with the different rings are presented in Figure 7. It can be easily seen that none of the conversion layers has compromised the antiwear resistance of the sample. In fact, being much softer thant the bearing steel (see Table 3), they appear much less “aggressive” to their steel contact mate, mitigating its wear mass loss by a factor of 5-6.

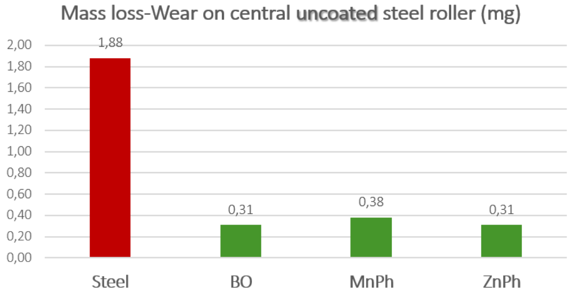

Figure 7: MPR wear test results – mass loss of the steel roller in contact with different uncoated (steel) and coated rings

The MPR surface distress test results, showing typical appearance of the steel roller surface, tested in contact with different sets of rings, can be seen in Figure 8. As can be noticed, all the three converison layers inhibit or highly mitigate the micropitting accumulation on the steel roller, compared to the all-steel contact (top left) where promonent micropitting damage is present.

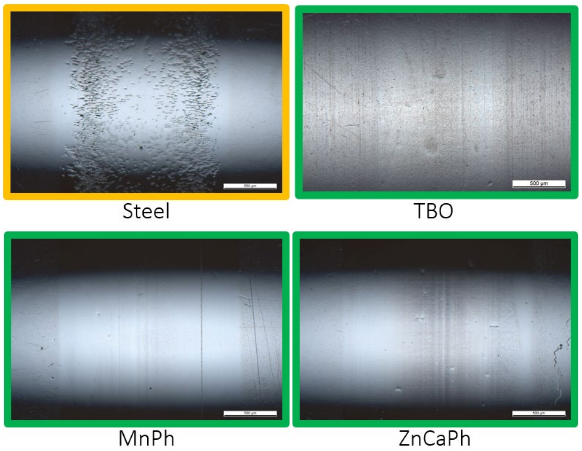

Figure 8: MPR micropitting test results – surface of the tested steel roller in contact with different uncoated (steel) and coated rings

The results of Figure 8 correspond to the case of smooth steel roller in contact with different coated rough rings. The influence of conversion layer location (on the smooth sample, on the rough counterbody or on both) vs. the reference all-steel contact is presented in Figure 9 for the case of TBO.

It can be seen that the double TBO (top right) and TBO produced only on the rough counterbody (bottom left) enhance the anti-micropitting protection of the contact, compared to the reference all-steel case (top left). However, if TBO is produced on the smooth sample only (bottom right), higher risk of micropitting, combined with severe abrasive wear, can be expected in the contact due to the unfortunate combination of roughness and hardness (soft and smooth TBO vs. hard and rough bearing steel, see Table 3).

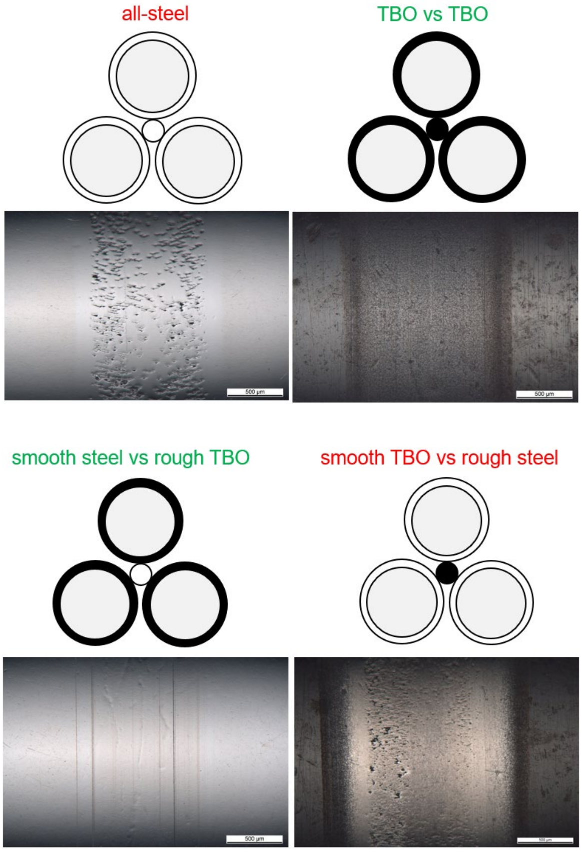

Figure 9: Influence of TBO location on micropitting – MPR test results with four possible configuratios under identical conditions

Possible influence of the conversion layers on grease ageing has also been evaluated. For this purpose, identical samples of fresh grease were mixed with Fe, FeO (mimicking TBO), MnPh and ZnPh particles (each 2% wt) and placed in an oven at 130°C (see Figure 10, left), along with some reference samples of pure grease. Once a week, the samples were taken from the oven for visual inspection and XPS (X-ray photoelectron spectroscopy) analysis. After four weeks, it was found that the grease samples mixed with Fe particles show signs of oil bleeding, as shown in Figure 10, right, while all the samples mixed with the conversion layer particles remained identical to the reference ones of the pure grease. These results imply that none of the three considered conversion layers is likely to facilitate grease ageing.

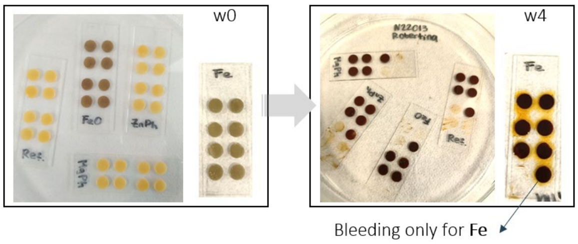

Figure 10: Possible influence of conversion layers on grease ageing – oil bleeding occurred for Fe particles only

4. Conclusions

In the present study, the frictional performance of three different conversion layers (TBO, ZnCaPh and MnPh) has been experimentally investigated under conditions typical for railway bearing application. The following observations have been made:

- The tribological black oxide (TBO) coating shows consistent low friction (when applied to the rougher or both surfaces), mainly thanks to its enhanced running-in ability.
- In this case, friction reduction is not compromised by higher wear or micropitting risk nor shorter grease life, as was verified by additional component MPR and grease ageing tests.
- In the case of high roughness difference between the contacting surfaces (e.g., smooth rolling elements vs. rough rings), TBO should not be applied to the smoother surface only. This can mitigate or cancel the expected friction reduction and compromise the tribological performance by e.g., increasing the risk of micropitting and/or abrasive wear.
- The other conversion layers, considered in the present study (MnPh and ZnCaPh), have not demonstrated a prominent and robust friciton reduction in the full bearing tests, compared to the reference all-steel bearings.

5. References

[1] N. Craven, "UIC Low Carbon Rail Challenge - Technical Report," International Union of Railways, Paris, 2014.

[2] *SKF Coating Catalogue,* SKF.

[3] E. Broitman, "Coatings to Improve Bearing Performance," *Evolution,* pp. 1-7, 2022.

[4] J. Gregory, "Chemical coatings of metals to resist scuffing and wear," *Tribology International,* vol. 11, pp. 105-112, 1978.

[5] M. George, "Factors Influencing Friction of Phosphate Coatings," Springfield Armory, Geneseo, IL, USA, 1964.

[6] P. Saffarzade, A. Amadeh and N. Agahi, "Study of tribological and friction behaviour of magnesium phosphate coating and comparison with traditional zink phosphate under dry and lubricated conditions," *Tribology International,* vol. 144, p. 106122, 2019.

[7] G. Bhar, N. Debnath and S. Roy, "Effects of Calcium Ions on the Morphology and Corrosion Resistance of Zinc-Phosphated Steel," *Surface Coating Technology ,* vol. 35, pp. 171-179, 1988.

[8] E. Broitman, A. Ruellan, R. Meeuwenoord, D. Nijboer and V. Brizmer, "Comparison of Various Conversion Layers for Improved Friction Performance of Railway Wheel-End Bearings," *Coatings,* vol. 13, p. 1980, 2023.

[9] V. Brizmer, K. Stadler, M. van Drogen, B. Han, C. Matta and E. Piras, "The Tribological Performance of Black Oxide Coating in Rolling/Sliding Contacts," *STLE Tribology Transactions,* vol. 60, no. 3, pp. 557-574, 2017.

[10] *DIN 50938 - Black Oxide Coatings on Ferrous Metal Components - Requirements and Test Methods,* Berlin, Germany: Deutsches Institut fur Normung e.V., 2018.

[11] *ISO 11408; Chemical Conversion Coatings - Black Oxide Coating on Iron and Steel - Specification and Test Methods,* Geneva, Switzerland: International Organization for Standardization, 1999.

[12] M. Ueda, H. Spikes and A. Kadiric, "Influence of Black Oxide Coating on Micropitting and ZDDP Tribofilm Formation," *STLE Tribology Transactions,* vol. 65, no. 2, pp. 242-259, 2022.

[13] C. Hager and R. Evans, "Friction and wear properties of black oxide surfaces in rolling/sliding contacts," *Wear,* Vols. 338-339, pp. 221-231, 2015.

[14] L. Zang, Q. Zhong, Y. Chen, W. Hou, B. Zhao and Y. Wu, "Effect of coating thickness on tribological properties of manganese phosphate conversion coating in different motion conditions," *Tribology International,* vol. 176, p. 107894, 2022.

[15] Y. Tamura, K. Kobayashi, K. Aratani, S. Tanaka, M. Kikuchi, M. Masuko and N. Ohtake, "Influence of Wear Surface Morphology and Phosphorus-Containing Tribofilm on Crack Initiation of Manganese Phosphate Coated Steel under Rolling–Sliding Contact," *Tribology Online,* vol. 15, pp. 154-169, 2020.

[16] G. E. Morales-Espejel and V. Brizmer, "Micropitting Modelling in Rolling-Sliding Contacts: Application to Rolling Bearings," *STLE Tribology Transactions,* vol. 54, pp. 625-643, 2011.

Approach towards the condition monitoring of journal bearings using surface acoustic wave technology

Thomas Decker[1], Georg Jacobs[2], Philipp Arneth[3], Julian Röder[4], Malte Raddatz[4]
[1] *Chair for Wind Power Drives RWTH Aachen University, thomas.decker@cwd.rwth-aachen.de*
[2] *Chair for Wind Power Drives RWTH Aachen University, georg.jacobs@cwd.rwth-aachen.de*
[3] *BestSens AG, philipp.arneth@bestsens.de*
[4] *Chair for Wind Power Drives RWTH Aachen University, julian.röder@cwd.rwth-aachen.de*
[5] *Chair for Wind Power Drives RWTH Aachen University, malte.raddatz@cwd.rwth-aachen.de*

Abstract–The use of journal bearings for the planetary bearings in wind turbine gearboxes is advantageous compared to rolling bearings in terms of drive train power density and expected lifetime. To reduce the downtime and increase the reliability of a planetary journal bearing suitable condition monitoring approaches for journal bearings are needed. Those condition monitoring systems (CMS) are still subject to current research efforts and often consist of temperature and vibration measurements. This work presents a new approach towards the monitoring of journal bearings using the Surface Acoustic Wave (SAW) technology. The measurement setup is installed and tested on a journal bearing test rig operating in full hydrodynamic and mixed friction conditions. The measurement results show a correlation between mixed friction as well as dry-running of the bearing and the propagation speed and amplitude damping of surface acoustic waves on the sliding surface of the bearings. The correlation can be used for condition monitoring purposes. Thus, a machine learning algorithm is trained with the SAW measurement data to autonomously detect different lubrication conditions.

Keywords – condition monitoring, journal bearings, surface acoustic waves, tribology

1. Introduction

Wind energy is the most important renewable energy source in Germany, producing around 50 % of the country's renewable electricity in 2022 [1]. In recent years the rated power output of new turbine generations increased steadily. If an increase of turbine power and steady capital and operating expenses (e.g. through increased reliability) can be achieved, a further reduction of the levelized costs of electricity (LCOE) for wind energy is possible. It can be assumed that turbine power ratings of up to 20 MW will be achieved in the next few years [2]. This development is pushing the drive train design to higher power densities, since the drive train's weight cannot increase indefinitely (e.g. due to limitations of the tower). The power density in the planetary stages of a wind turbine gearbox can be increased by the use of journal bearings as planet gear bearings instead of rolling bearings due to their more compact design [3]. In addition, journal bearings are characterized by their long service life compared to rolling bearings. If they are designed and operated correctly, journal bearings can be operated almost indefinitely. This is a significant advantage, particularly in the view of the high operational expenditures (OpEx) for wind energy (around 33 % of the LCOE for offshore wind power plants in the year 2021 [4]).

For the safe operation of journal bearings and reduced downtime, a reliable condition monitoring system (CMS) that communicates with the turbine controller is of great importance (e.g. derate turbine power to prevent bearing seizure). The integration of condition monitoring systems into the turbine control is currently still a challenge for the wind industry, but offers great economic potential [5]. Although condition monitoring methods for rolling bearings and gear contacts already exist [6], monitoring methods for journal bearings (e.g. journal bearings for wind turbine gearboxes) have a significantly lower technology readiness level and are therefore currently still subject to research.

One example for a simple monitoring method for journal bearings is the measurement of the bearing temperature, as friction in the bearing can be detected by an increase in temperature [7]. Another frequently discussed measurement method is the so-called Acoustic Emission (AE). The AE emitted by a tribological contact in case of mixed friction can be measured using highly sensitive piezoelectric transducers. Examples for the application of AE measurements for condition monitoring purposes are journal bearings and rolling bearings [8, 9] as well as gear flank contacts [10]. The disadvantage of the AE measurement method is the high sampling rate required to capture the high frequencies. In addition, passive acoustic measurement methods recording structure borne sound emitted by the tribological contact of interest are susceptible to interference, which is a significant disadvantage, especially for applications in wind energy gearboxes. The Surface Acoustic Wave (SAW) technology offers an alternative to this, since it measures actively emitted ultrasonic signals with a specific frequency which are less prone to acoustic disturbance. The use of artificially generated sound signals for condition monitoring is especially suitable for journal bearings due to the lack of natural excitation (e.g. bearing frequencies).

The SAW technology is already proven in the non-destructive testing of various materials for mechanical defects. Cracks and impurities in the material of a wave guide can be detected since they alter the propagation behavior of SAW [11]. The properties of a fluid which is in contact with the wave guide material can also be quantified through the propagation behavior of SAW. This can be used to monitor tribological contacts like bearings or seals using the SAW technology. SAW based condition monitoring of rolling bearings and seals has already been proposed before [12]. The technology has been tested and improved in several investigations:

In an investigation on linear friction contacts and rolling bearings by Linder et al. the SAW propagation speed and amplitude has found to be sensitive to lubricant viscosity [12]. This result was later confirmed by Tyreas et al. [13]. Lindner et al. also showed that the SAW propagation characteristics (amplitude and transmission time) in a rolling bearing depend on the amount of lubricant in the bearing, which enables the monitoring of lubrication conditions [14]. Chmelar et al. demonstrated that the propagation speed of SAW excited in a rolling bearing outer ring is sensitive to the film thickness and thus the load [15].

Nohyu et al. demonstrated experimentally that the propagation velocity of SAW in a solid-solid interface changes in agreement with the contact load [16]. This effect has the potential to enable the monitoring of solid contact in bearings by means of SAW measurements.

Drinkwater et al. proved that the reflection characteristics of an ultrasonic signal in a lubricated contact can be used to measure the film thickness in bearings [17].

There is little literature on the use of SAW technology on journal bearings in the state of the art. This work contributes to transferring the findings from the aforementioned investigations to journal bearings for the purpose of condition monitoring. This is done by performing experiments on a journal bearing component test rig equipped with a SAW measurement setup. The aim of these experiments is the identification of signal features sensitive to operating conditions of the bearing. Secondly, these findings are used to showcase an oil film height classification based on a machine learning algorithm utilizing the SAW measurement data. The results of this classification approach are presented and discussed.

2. Experimental Setup

For the experimental investigation of SAW on journal bearings in this work a component test rig is used (Figure 1). It comprises an electric motor for the application of a specific sliding speed v and hydraulic actuator for the application of a radial force F_N. The friction torque between bearing and shaft is measured with a force transducer (in combination with the lever arm) mounted to the rotatable bearing enclosure.

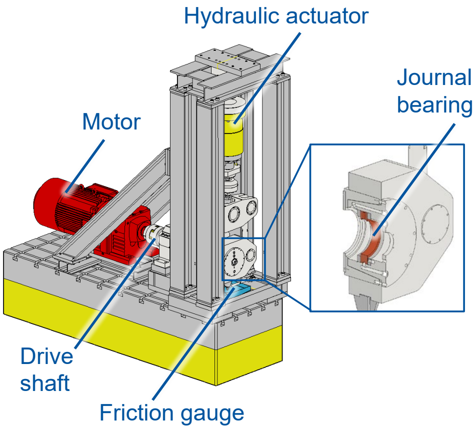

Figure 1: Journal bearing test rig

In addition to the SAW measurement the sliding speed v, friction moment M_{Fr} and temperature ϑ of the bearing are recorded during testing. All experiments shown in this work are performed using an ISO VG 320 wind turbine gearbox oil (PAO) as the lubricant to create comparability to the real WT application. The specification of the overall test setup (bearing geometry) can be found in Table 1.

Table 1: Specifications of the test setup

Parameter	**Symbol**	**Value**	**Unit**
Diameter	D	120	mm
Width	B	30	mm
Nominal clearance	S	80	µm
Bearing surface roughness	$R_{a,B}$	0.4	µm
Shaft surface roughness	$R_{a,S}$	0.6	µm

3. Method

SAW propagate along the surface of a solid substrate, which can have both transverse and longitudinal components. Their propagation behavior highly depends on the elastic properties of the substrate (so-called wave guide) they propagate on.

One example for a type of SAW is the so-called Rayleigh wave (see also Figure 2). Rayleigh waves propagate along the surface of solids (X - Direction) and include both longitudinal and transverse motion. Their amplitude decays exponentially with increasing distance from the surface to a penetration depth of a few wave lengths [18, 19].

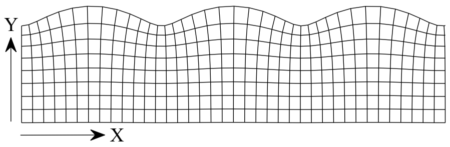

Figure 2: Schematic visualization of a Rayleigh wave

Rayleigh waves are non-dispersive, which means that their velocity c_R is not dependent on their wave frequency. For materials with a Poisson ratio ν above 0.3 the Rayleigh wave speed c_R can be approximated as

$$c_R = c_S \cdot \frac{0.87 + 1.12 \cdot \nu}{1 + \nu} \qquad \textit{(Eq. 1)}$$

with c_S being the shear wave velocity in the corresponding material [18].

Another type of acoustic wave mode worth mentioning for the context of this work are the so-called Lamb waves. Lamb waves occur when the thickness of the guiding substrate (plate thickness d) is within a similar scale as the wavelength λ. Therefore Lamb waves can emerge on thin plates, rings and spheres [20]. There exist two fundamental vibration modes of Lamb waves: the asymmetrical vibration (A0-mode shown in Figure 3 a)) and the symmetrical vibration (S0-mode shown in Figure 3 (b)) [19, 21]. Both wave forms and modes with order can occur in superposition.

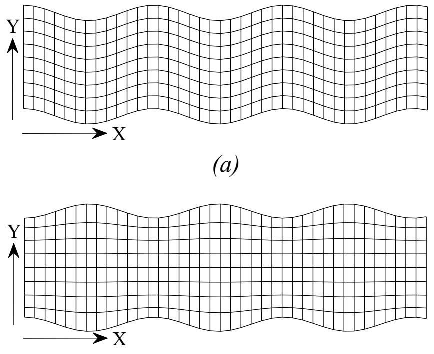

(a)

(b)

Figure 3: (a) A0 asymmetrical fundamental Lamb wave mode, (b) S0 symmetrical fundamental Lamb wave mode

Lamb waves are dispersive, which means that the propagation speed c of a specific mode form depends on the product of the wave frequency ω and the plate thickness d [19]. Thus, lamb wave mode forms have different propagation speeds.

Through an active excitation, for example using a piezoelectric transducer, the aforementioned wave modes (both Rayleigh and Lamb waves) can be excited in solid materials [12, 14, 22]. In this work the SAW measurement setup consists of two piezoelectric probes (emitter and sensor) mounted to the stationary part of the journal bearing [12, 13] (see also Figure 4).

The test bearings are machined to have two radially inward facing boreholes into which the piezoelectric probes are glued with a permanent bonding. The probes are aligned perpendicular to the sliding surface. Afterwards, the piezo probes are encapsulated with a polymer compound to protect them from external influences.

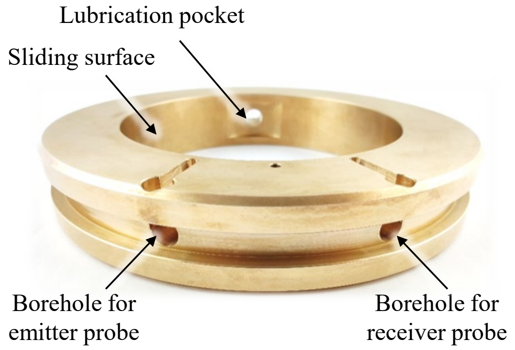

Figure 4: Journal bearing with radial boreholes for the application of the piezoelectric probes for the SAW measurement

The measurement setup is shown in Figure 5. In this work the journal bearing itself acts as the wave guide with the SAW propagating on the sliding surface. The emitter probe excites acoustic waves in the journal bearing material. This is illustrated through the exemplary finite-element simulation result of the wave amplitude propagating through the journal bearing in Figure 5. The probes are spaced 40° (bow length $b_l = 42\,mm$) apart such that the load zone of the journal bearing (area of maximum pressure) is located in the center between the probes. A similar setup has been used by Chmelar et al. for the monitoring of the oil film height in a rolling bearing [15]. In the case of mixed friction asperity contact would occur in the area between the two probes.

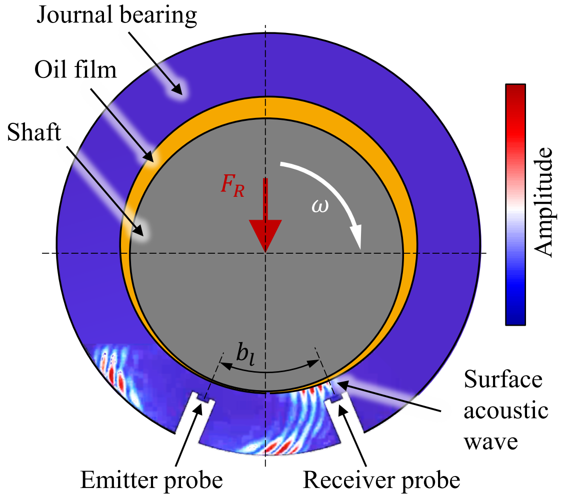

Figure 5: Schematic visualization of the SAW measurement setup on a radial journal bearing

The specimen used in this work are journal bearings manufactured from the bronze alloy CuSn12Ni2-C. The specifications of the material are given in Table 1.

Table 1: Specifications of the bearing material

Parameter	**Symbol**	**Value**	**Unit**
Young's modulus	E	100	GPa
Possion's number	ν	0.33	-
Shear wave velocity [23]	c_S	2044.12	m/s

If at least one surface side of the wave guiding substrate (in this case the journal bearing) is in contact with a fluid (in this case the oil film), Lamb and Rayleigh waves can leak energy into the fluid. Hereby acoustic pressure waves are generated in the fluid. The liquid waves propagate under the so-called Rayleigh angle at an angle to the surface of the wave guide. [18]. This causes the wave on the wave guide to decay as it propagates along the surface. This phenomenon of a decoupling Lamb or Rayleigh wave in a solid-fluid half space is also known as a Leaky Lamb wave or Leaky Rayleigh Wave respectively [21]. A schematic example for a Leaky Lamb wave in a solid-fluid interface is shown in Figure 6.

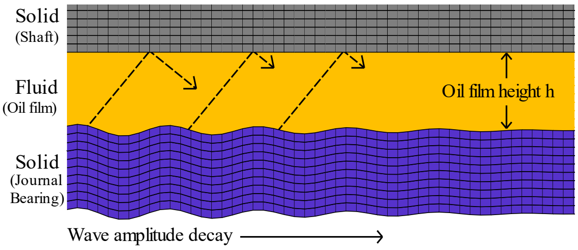

Figure 6: Schematic visualization of a Leaky Lamb wave in a solid-fluid interface

In the context of this work the solid-fluid interface consists of the bearing material and the oil film that separates the bearing from the shaft. As shown in Figure 6 the pressure wave generated in the liquid through the Leaky Lamb wave eventually reaches the shaft material. When the pressure wave in the liquid film reaches the shaft, another surface wave is excited on the shaft and will partly couple back a certain proportion of its energy into the fluid. The distance traveled by the acoustic waves in the liquid is therefore dependent on the oil film height h (Figure 6).

When solid contact between the bearing and the shaft occurs due to mixed friction the transfer behavior is changed again, since a direct acoustic coupling occurs between the two solids. Thus, the propagation behavior of the SAW on the bearing's sliding surface is influenced by the operating condition of the bearing. The propagation behavior can be measured via the following approach:

The emitter probe excites SAW on the bearing's sliding surface through an excitation signal $\hat{x}_i$ containing a short sinusoidal wavelet. The excitation form is shown in Figure 7. This wavelet function $u(t)$ is created through the multiplication of a sine wave and a hann-window function according to (Eq. 2.

$$u(t) = \sin(2\pi \cdot f_E \cdot t) \cdot \frac{1}{2}\left[1 - \cos\left(\frac{2\pi n}{M-1}\right)\right] \qquad \textit{(Eq. 2)}$$

The excitation wavelet has a constant carrier frequency of $f_E = 350$ kHz and is emitted every 1.0 ms, which is also the evaluation interval for the feature extraction on the recorded signal.

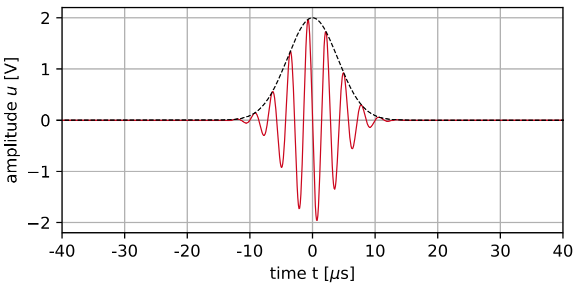

Figure 7: Excitation wavelet with excitation frequency $f_E = 350\ kHz$

The receiver probe repeatedly measures the response signal x(t) at t=0.0 µs of the excitation at a sampling frequency of 10 MHz. Due to the aforementioned dispersion effect the original signal from Figure 7 is decomposed into several wave groups. An example for the measured signal in the journal bearing during operation is shown in Figure 8. In this case two significant wave groups appear in the measured signal between 10 and 30 μs as well as 35 and 50 μs.

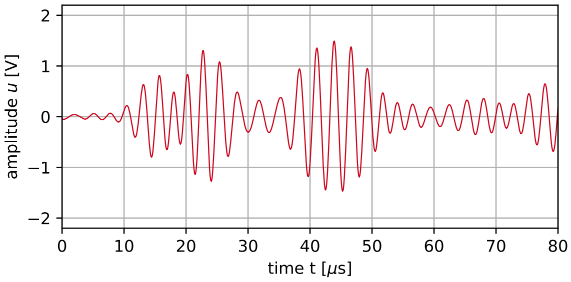

Figure 8: Exemplary measured response signal corresponding to an excitation frequency of $f_E = 350\ kHz$

For a precise measurement, a monomodal signal or a signal with distinguishable modes must be achieved preferably, since a superposition of several wave modes can disturb the measurement. Therefore, an excitation frequency f_E must be found that causes minimal modal superposition and disturbance. The longer the distance travelled by a SAW on the wave guide (e.g. multiple cycles over the full bearing circumference), the more susceptible the measurement is to interference. For this reason, the Rayleigh wave passing directly through the load zone is preferably evaluated in this work. For the abovementioned bearing material (Table 1) and probe distance b_l and according to (Eq. 1 the propagation duration t_R of the Rayleigh wave passing through the load zone can be expected to be:

$$t_R = \frac{b_l}{c_R} \approx 23\mu s \qquad \textit{(Eq. 3)}$$

This corresponds to the response signal in Figure 8, where the most significant peak of the first wave group reaches the sensor after approximately 23 µs. In Figure 9 an example for an unfavorable response signal is demonstrated. This particular signal has been measured under the exact same operating conditions of the bearing as the above shown signal, but was excited with an excitation frequency of $f_E = 400$ kHz. The signal in Figure 9 contains modal superpositions well recognizable through the phase shifts at $t = 35$ µs and $t = 42$ µs.

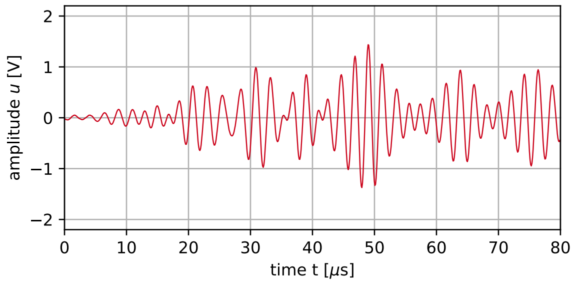

Figure 9: Exemplary measured response signal corresponding to an excitation frequency of $f_E = 400\ kHz$

3.1. Signal processing

Under the influence of different operating conditions and lubrication regimes the wave propagation behavior changes [15]. The change in propagation behavior is evaluated using several signal features:

The propagation time of the signal τ as well as the wave amplitude value A is measured by tracking the zero-crossing point of one particular phase from the measured signal. The phase to be tracked is specified by the so-called gate position $\mathrm{t_G}$ (e.g. indicated in Figure 11). The gate position should always be set to a phase of the received signal that has a significant amplitude [14].

The modulation width of the propagation time signal τ, also known as propagation time modulation Δτ, specifies the maximum available delay difference / delay modulation within a defined time window $t_{W,0}$ to $t_{W,1}$. This time window contains numerous excitation cycles, such that the propagation time modulation $\Delta\tau$ describes the change in modulation over time. In simpler terms, it is the difference between the maximum and minimum propagation time value in a defined time window ge of the analyzed measurand (Runtime). It can be calculated according to Eq. 4 [6].

$$\Delta\tau = \max_{\{\mathrm{t} \in [\mathrm{t_{W,0}}, \mathrm{t_{W,1}}]\}} \tau(\mathrm{t}) - \min_{\{\mathrm{t} \in [\mathrm{t_{W,0}}, \mathrm{t_{W,1}}]\}} \tau(\mathrm{t}) \qquad \textit{(Eq. 4)}$$

In addition to measuring the acoustic wave behavior in terms of the propagation time τ and the wave amplitude value A a third signal feature is noteworthy. The integral value σ describes the amplitude energy of the received signal x_i in a time interval with a specific duration Δt (integral width) starting at t_0.

$$\sigma = \int_{t_0}^{t_0+\Delta t} x\, dt \qquad \textit{(Eq. 5)}$$

The so-called center of energy also referred to as decay time γ indicates the elapsed time until the decay of the measured signal x_i to half its initial energy

$$\gamma = \frac{1}{M} \sum_{i=1}^{n} n \cdot x_i \qquad \textit{(Eq. 6)}$$

with M being the total energy of the signal in one evaluation interval. All of the abovementioned signal features are extracted from the measurement every 1.0 ms.

4. Results and discussion

This chapter discusses measurement results from the presented journal bearing test equipped with a SAW measurement system. Firstly, results from an experimental pre-study are shown. The aim of the experiments is a basic understanding of the nature of the SAW propagation behavior in a journal bearing and identified characteristic features of the measurements that can indicate mixed friction. Secondly, an approach for the determination of the oil film height using SAW measurement is discussed.

4.1. SAW measurements during operation

The experiment shown in Figure 10 demonstrates the load dependency of the SAW measurement. While maintaining a constant sliding speed v the specific pressure

$$\bar{p} = F_N/(B \cdot D) \qquad \textit{(Eq. 7)}$$

was varied in four intervals between 5 and 60 MPa with a duration of 20 sec. per interval. The bearing's sliding speed v is kept constant at 0.3 m/s during the experiment.

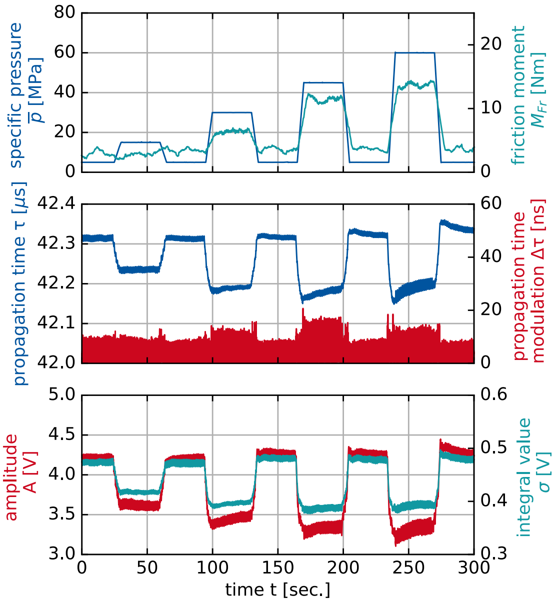

Figure 10: SAW measurement results under swelling loads and constant sliding speed ($v = 0.3\ m/s$*)*

The bearing temperature and thus oil viscosity is kept constant as well. The friction in the journal bearing per load step is indicated by the friction moment M_{Fr} varying from 2 to 12 Nm.

The received signal x(t) corresponding to the experiment shown above is presented in Figure 11. For the evaluation of propagation time τ and amplitude A a particular phase in x(t) with a significant amplitude is chosen. In this experiment the gate is set at $t_G = 23$ µs according to Eq. 3 (see also Figure 11).

The integral value σ is evaluated over the time period that contains the mode in which the gate is set. The boundaries for the evaluation of the integral value are set be 10 µs and 30 µs capturing the first wave group in the received signal (see also Figure 11).

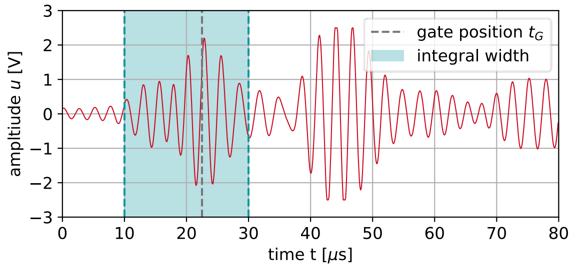

Figure 11: measured response signal

The propagation time τ of the SAW is shown in Figure 10. The measurements show a correlation between the applied load $\bar{p}$ and the propagation time τ. Another significant observation is that both the signal of the amplitude A and the propagation time τ, are subject to a certain modulation. A closer look at the signals reveals that the carrier frequency of the modulation corresponds to the rotational frequency f_N of the shaft and thus the sliding speed v of the journal bearing. The effect is shown in Figure 12. The modulation can be explained by the eccentric position of the shaft in the bearing.

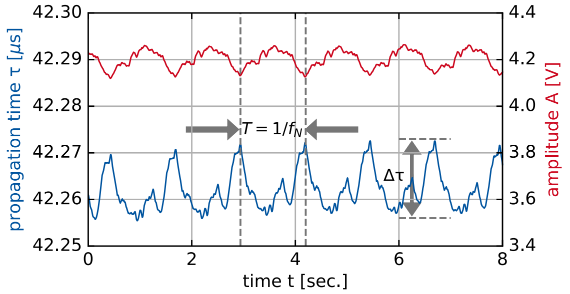

Figure 12: Periodic modulation of the propagation time and amplitude signals ($v = 0.3\ m/s$)

The modulation signal $\Delta\tau$ of the wave propagation time τ is shown in Figure 10. A clear correlation can be observed between the modulation width $\Delta\tau$ and the frictional moment M_{Fr} resulting from the applied specific pressure $\bar{p}$. The variance of the modulation width $\Delta\tau$ is between 10 and 20 µs. This can be explained as follows:

When mixed friction occurs in the journal bearing, individual asperities of the bearing and shaft are in contact. Consequently, the sound wave can propagate significantly faster. This corresponds to the findings described in [16]. The asperity contact events in a journal bearing are randomly distributed, which causes the wave propagation time signal τ to modulate strongly.

One operating event in which journal bearings typically exhibit high levels of mixed friction is starting up from a standstill. Figure 13 shows an excerpt from an experiment in which cyclical start-stop processes are carried out under constant specific pressure ($\bar{p} = 10\ MPa$ corresponding to a radial force F_N of $36kN$). The upper plot shows the sliding speed v and the friction moment M_{Fr}. It can be observed that the start-up under load causes a high breakaway torque ($\sim 150Nm$) which indicates high amounts of friction. The effect of modulation of the acoustic wave properties under the influence of friction is even more pronounced here. The modulation width of the wave propagation time $\Delta\tau$ is one order of magnitude greater than in the above shown experiment. The breakaway moment is caused by the high asperity contact. The intense mixed friction at the moment of breakaway causes a notable decrease of measured wave amplitude A and integral value σ.

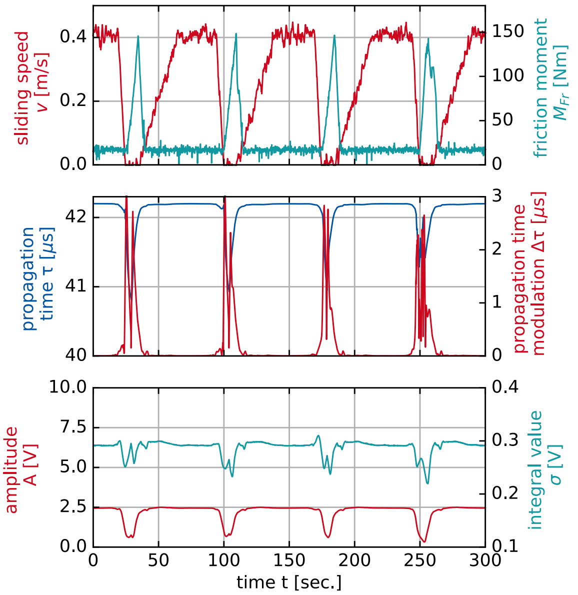

Figure 13: SAW measurement results under start-stop conditions at constant load ($\bar{p} = 10MPa$)

The observed behavior of the acoustic waves can be explained as follows: when the journal bearing is loaded with a constant radial force at standstill no oil film can be build up. This causes large amounts of both sliding surfaces to be in solid contact without a separating oil film. This causes the acoustic wave energy to couple directly into the shaft material without any fluid film interaction, which causes the propagation time to drop drastically from about 42 µs to 40 µs (Cf. Figure 10 with a variation of propagation time τ between 42.3 µs to 42.15 µs). The start-stop operation shown in Figure 13, was carried out over a total duration of 9 hours to evaluate the correlation of the SAW measurement and running-in wear of the bearing. The time-averaged trends of the friction moment M_{Fr} and the propagation time modulation $\Delta\tau$ are shown in Figure 14.

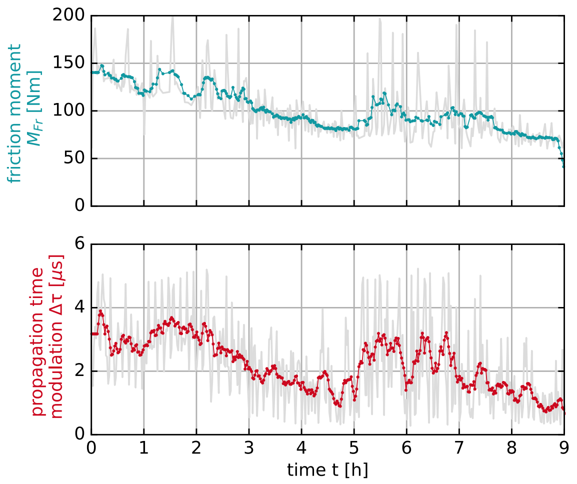

Figure 14: Time average trends of the friction moment and propagation time modulation during repetitive start-stop operation

A decrease in the friction moment from the initial 150 Nm to around 70 Nm can be observed. This indicates running-in of the bearing. Similarly, the runtime modulation is also reduced over time. This emphasizes the assumption that the propagation behavior of the SAW is directly dependent on the amount of friction in the bearing.

In summary the above shown results indicate that the SAW measurement is sensitive to mixed friction in a journal bearing setup. The propagation time modulation width $\Delta\tau$ in particular appears to react especially sensitively to mixed friction.

4.2. Oil film height classification

For a CMS, separation-effective signal features are needed for the detection of mixed friction. In the above shown experiment the runtime modulation $\Delta\tau$, integral value σ and wave amplitude A have been proven to be such features. A frequently discussed parameter that can be used to quantify the momentary condition of a journal bearing is the oil film height h [24]. Different lubrication regimes in a journal bearing can be expressed by the specific oil film height Λ, which is the relation of the minimal oil film height h_{min} and the roughness values $R_{q,i}$ of the sliding surfaces [24, 25].

$$\Lambda = \frac{h_{min}}{\sqrt{R_{q,1}^2 + R_{q,2}^2}} \qquad \text{(Eq. 8)}$$

Illner et al. suggest $\Lambda = 3$ for the smallest permissible value of the minimum specific oil film height for hydrodynamic operation [26]. For values below this threshold mixed friction can be expected. Monitoring the specific oil film height Λ is therefore a frequently addressed condition monitoring approach for journal bearings [17]. The suitability of a CMS can be assessed by the following two target values: low confusion (high classification accuracy) and low latency (fast reaction time). In the following classification approach for the specific oil film height Λ based on SAW measurements using a machine learning method is presented and evaluated with respect to confusion and latency:

Due to the effect of the leaky Lamb Waves in a solid-fluid half space the distance covered by an acoustic wave theoretically is a function of the oil film height h (Figure 6). Figure 15 shows two maps of averaged measured results at constant operating conditions for the center of energy γ (a) and integral value σ (b). The lower plot (c) shows the minimum oil film height h_{min} calculated by means of an elasto-hydrodynamic (EHD) simulation of the test rig.

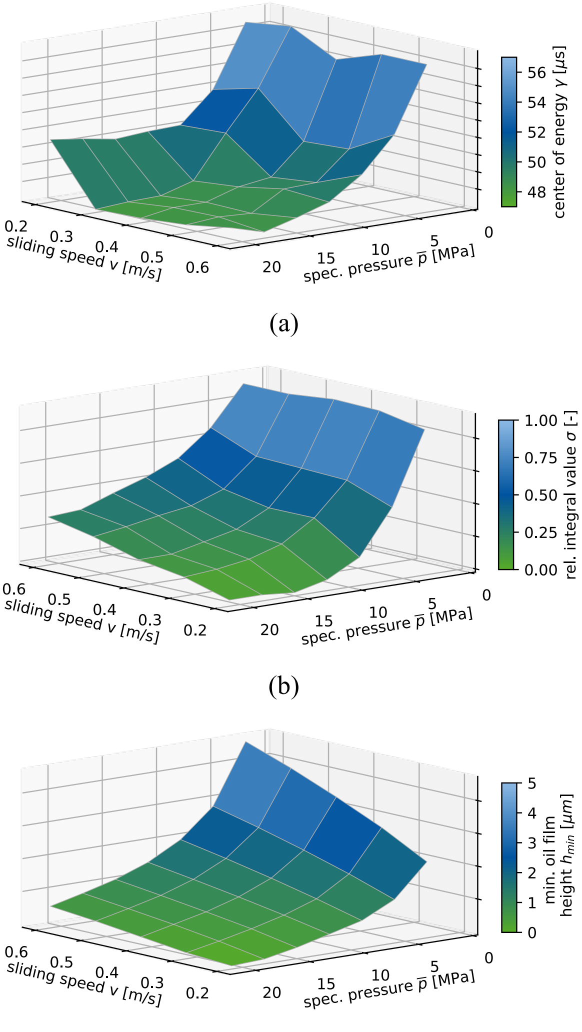

(a)

(b)

(c)

Figure 15: Measurement results for the SAW center of energy (a) and wave amplitude (b) and EHD-simulation result for the minimum oil film height of the bearing (c)

By comparing the measurements to the simulation results it can be observed that with an increase in specific pressure $\bar{p}$ and thus decrease in oil film height h (and Λ value respectively) the SAW amplitude A is reduced and smaller values for the center of energy γ can be observed. This corresponds to the findings described before. The measurements from Figure 15 are used to train a machine learning algorithm for the detection of different friction states.

Since the specific oil film height Λ is an important indicator for describing the friction state of a journal bearing, it is assumed, that SAW measurements can be used to detect different oil film heights and thus potentially critical operating conditions.

In this work, a distinction is made between three different friction states expressed by Λ. These three states are described in Table 2.

Table 2: Friction states to be distinguished by the classifier

Specific oil film height	**Interpretation**
$1 > \Lambda$	Severe mixed friction
$3 > \Lambda > 1$	Mild mixed friction
$\Lambda > 3$	Hydrodynamic condition

A classification algorithm based on a multi-layer perceptron (MLP) neural network is trained to detect different values for Λ. Since this method is a supervised machine learning, the training data set must be labeled with the corresponding value for Λ at each data point. The labelling data y is generated using the aforementioned EHD-simulation results. The generated labels are shown in Figure 16.

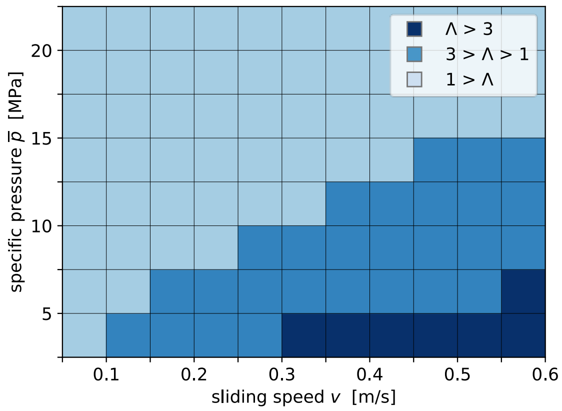

Figure 16: Map for the specific oil film height λ

The neural network's architecture is shown in Figure 17. The input data x to the classifier contains SAW information (integral value σ and runtime modulation $\Delta\tau$) as well as the sliding speed v and bearing temperature T. The sliding speed and temperature are used as additional input data to the classifier since they have a substantial influence on the oil film height h.

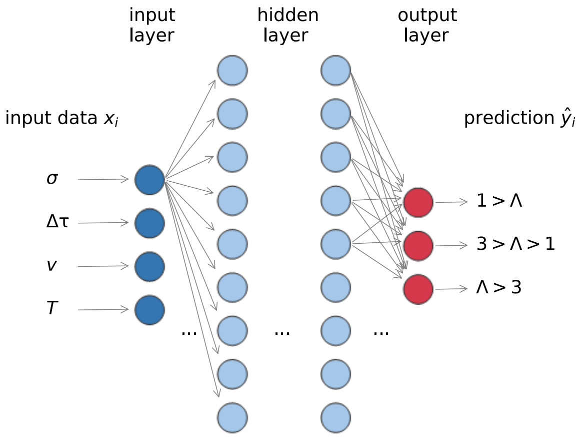

Figure 17: Schematic depiction of the multi-layer perceptron network used for state classification

The measured data x to the MLP-classifier is scaled according to (Eq. 9 to achieve a balanced input dataset.

$$x_{i,scaled} = \frac{x_i - x_{min}}{x_{max} - x_{min}} \qquad \text{(Eq. 9)}$$

Several consecutive experiments are conducted on the test rig. Resulting in a training and validation dataset. For both training and validation two datasets from different test runs are used with an overall duration of approximately 3.5 h including 36 different operating points each. After the generation of the labels the training dataset is resampled to remove class imbalance. This procedure generates a dataset containing an equal amount of datapoints for each friction state, which can increase the overall accuracy [27]. After training with the first dataset, the MLP-classifier is validated using the second dataset. The accuracy of the classification is one of the aforementioned target values for a condition monitoring system. The achieved accuracy on the validation dataset is shown in the confusion matrix in Figure 18.

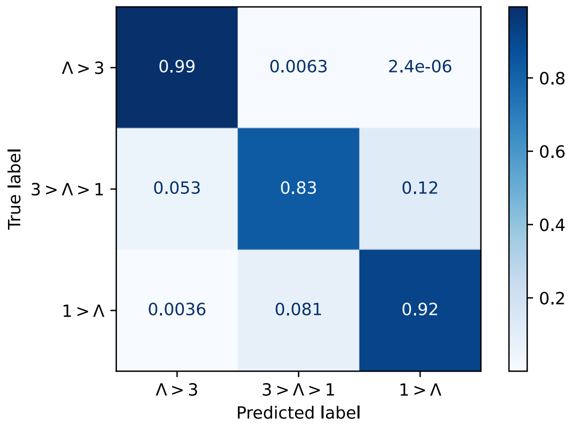

Figure 18: Confusion matrix of the friction state classification using a multi-layer perceptron classification algorithm

The more a confusion matrix resembles a diagonal matrix, the better the classification result. Overall, each individual class is recognized with good accuracy. Only few datapoints are classified as false positives (upper right corner of the matrix).

In addition to the above shown confusion matrix the overall accuracy A of the classification is evaluated as the ratio of the number of correctly predicted datapoints $n_{correct}$ and the overall number of executed predictions $n_{\hat{y}}$.

$$A = \frac{n_{correct}}{n_{\hat{y}}} \qquad \text{(Eq. 10)}$$

After the training of the MLP classifier a test accuracy of $A_{test} = 99.6\ \%$ is achieved. The classification accuracy on the validation dataset reaches a score of $A_{validation} = 89.9\ \%$.

In Figure 19 the signals of y (label) and $\hat{y}$ (prediction) over time are presented for an excerpt of the validation experiment. In the upper plot the specific pressure $\bar{p}$ and sliding speed v are shown over time. The stepwise decrease in load at constant sliding speed from 180 sec. onwards causes the oil film height h to increase (cf. Figure 15 a). An increase in oil film height is favorable for the bearing and therefore the label value y transitions from $1 > \Lambda$ (180 sec. to 290 sec.) to $\Lambda > 3$ (1250 sec. to 1400 sec.). For every datapoint in time measured during the test procedure the MLP classifier performs one corresponding classification. A low latency time is advantageous here, as mentioned above. At 180 sec. a rapid transition in the sliding speed v (falling flank) and specific pressure $\bar{p}$ (rising flank) occurs. This event causes a short period of confusion in the oil film height prediction. This can be identified in the plot through the deviation of the signals for y and $\hat{y}$ between 180 sec. to 200 sec.

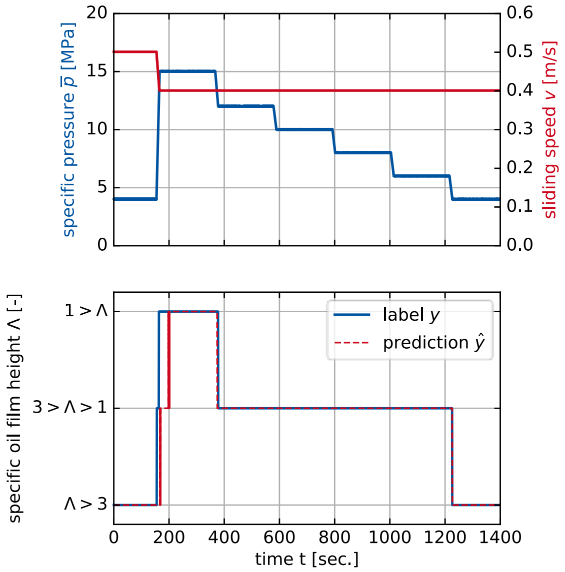

Figure 19: Comparison between the label and predicted state over time

It is assumed that such high dynamic load changes do not occur in the operation of wind turbines due to the high inertia of the drive train. For the remaining time of the shown test procedure a far more accurate prediction is achieved. Between 200 and 1400 sec. both signal y and $\hat{y}$ coincide.

Consequently, the prediction of the oil film height h using the method presented in this work is valid primarily for stationary operating conditions. A simultaneous transition in sliding speed and load remains challenging.

5. Conclusion

A reliable monitoring technique for journal bearings as planetary bearings in WT gearboxes is still subject to research. This work proposes a new approach for the condition monitoring of journal bearings using the SAW method, which is a technology already in commercial use for numerous monitoring (e.g. rolling bearings) and inspection tasks (e.g. structural health monitoring). The main advantage of the presented method is the measurement of actively excited SAW on the bearing's sliding surface since journal bearings have no natural excitation sources that could be used for monitoring purposes (compared to roller bearings and gear meshes). The waves are excited using piezoelectric transducers and the amplitude and propagation time behavior of the waves passing through the bearing's load zone are measured. The active sound measurement makes the method presented robust against acoustic interference. This distinguishes it from conventional condition monitoring methods such as vibration measurement.

The aim of this work is the successful application of the SAW method to journal bearings and the prediction of the oil film height of a journal bearing by means of a machine learning approach using SAW measurements.

Experimental studies are carried out on a component test rig for journal bearings under different load scenarios. The results show a good correlation between the measured friction moment and the characteristic features of the SAW measurements being wave amplitude and propagation time.

For the prediction of the oil film height, a machine learning approach was used. The MLP neural network was trained with measurement data from experiments on the journal bearing test rig equipped with the SAW measurement technology and then validated afterwards. Training labels for the specific oil film height result from EHD-simulations of said bearing. It was shown, that a good accuracy (mean classification accuracy 89.9 %) could be achieved with this approach. The presented approach works best for stationary conditions and shows minor confusion during transient changes between operating points.

6. Outlook

This work's data evaluation is solely done in a post-processing. In future work the presented setup will be extended to feature real-time capable anomaly detection based on SAW measurements paving the way towards an online CMS for WT gearbox journal bearings. A fast detection of operational anomalies (e.g. shortfall of bearing lubrication or particle contamination in the lubricant) is of special importance since such events can lead to a rapid deterioration of the bearing [28].

Secondly the method will be transferred to a planetary journal bearing application. Since planetary journal bearings have a larger width-to-diameter ratio than the bearings investigated in this work, the acoustic coverage of the entire sliding surface of a planetary bearing still poses a challenge to be addressed. For these purposes special gear stage test rigs for planetary journal bearings are eligible.

Finally, the method will be applied in a full-size WT gearbox. Extensive tests on system level will follow. In these future studies, the remaining challenges for the in-situ monitoring of planetary gear bearings will be addressed. These include the energy self-sufficiency of the measurement hardware and telemetric data transmission from the rotating gear stage in the gearbox to the turbine controller.

Acknowledgment

The authors would like to thank the Ministry of Economic Affairs and Climate Action of Germany, for the financial support granted. They also thank their project partners for the equipment, insight as well as expertise they have provided, which contributed to this joint project.

Supported by:

Federal Ministry
for Economic Affairs
and Climate Action

on the basis of a decision
by the German Bundestag

7. Literature

[1] Arbeitsgruppe Erneuerbare Energien: Erneuerbare Energien in Deutschland. Daten zur Entwicklung im Jahr 2022. 2023

[2] Siddiqui, M. O., Feja, P. R., Borowski, P., Kyling, H., Nejad, A. R. u. Wenske, J.: Wind turbine nacelle testing: State-of-the-art and development trends, Bd. 188. 2023

[3] K. Lubenow: Requirements for wind turbine gearboxes with increased torque density with special attention to a low-noise turbine operation. Conference for Wind Power Drives 2019 - Conference Proceedings (2019)

[4] Stehly, T. u. Duffy, P.: 2021 Cost of Wind Energy Review. 2022

[5] Tchakoua, P., Wamkeue, R., Ouhrouche, M., Slaoui-Hasnaoui, F., Tameghe, T. u. Ekemb, G.: Wind Turbine Condition Monitoring: State-of-the-Art Review, New Trends, and Future Challenges. Energies 7 (2014) 4, S. 2595–2630

[6] J. Kolerus u. J. Wassermann: Zustandsüberwachung von Maschinen. 7. Auflage. expert verlag 2017

[7] Baszenski, T., Kauth, K., Kratz, K.-H., Gutiérrez Guzmán, F., Jacobs, G. u. Gemmeke, T.: Sensor integrating plain bearings: design of an energy-autonomous, temperature-based condition monitoring system, Bd. 87. 2023

[8] König, F., Marheineke, J., Jacobs, G., Sous, C., Zuo, M. J. u. Tian, Z.: Data-driven wear monitoring for sliding bearings using acoustic emission signals and long short-term memory neural networks. Wear 476 (2021), S. 203616

[9] Mokhtari, N., Pelham, J. G., Nowoisky, S., Bote-Garcia, J.-L. u. Gühmann, C.: Friction and Wear Monitoring Methods for Journal Bearings of Geared Turbofans Based on Acoustic Emission Signals and Machine Learning. Lubricants 8 (2020) 3, S. 29

[10] Leaman, F.: A Review on Acoustic Emissions of Gear Transmissions: Source, Influencing Parameters, Applications and Modeling. 2024

[11] Yu, L. u. Giurgiutiu, V.: Piezoelectric Wafer Active Sensors in Lamb Wave-Based Structural Health Monitoring, Bd. 64. 2012

[12] Lindner, G., Schmitt, M., Schubert, J., K., S. u. Faustmann, H.: On-line surveillance of lubricants in bearings by means of surface acoustic waves. IEEE transactions on ultrasonics, ferroelectrics, and frequency control 57 (2010) 1, S. 126–132

[13] Tyreas, G., Dwyer-Joyce, R. S., Notay, R. S. u. Durham, D. J.: Measuring lubricant viscosity at a surface and in a bearing film using shear-horizontal surface acoustic waves. Proceedings of the Institution of Mechanical Engineers, Part J: Journal of Engineering Tribology 236 (2022) 8, S. 1511–1530

[14] Lindner, G., Brückner, C. u. Schmitt, M.: Online Bearing Lubricant Sensing by Mode Conversion of Surface Acoustic Waves. In: Sensor + Test Conference 2011 - Conference Proceedings

[15] Chmelar, J., Petr, K., Mossoczy, P. u. Dynybyl, V.: Experimental study of lubrication film monitoring in a roller bearing by utilization of surface acoustic waves. Tribology International 141 (2020), S. 105908

[16] Nohyu, K., Taejong, L. u. Soowhan, K.: Monitoring of Contact Pressure of Solid-Solid Interface using Acoustic Nonlinearity. In: Proceedings of the 11th euspen International Conference – Como. 2011

[17] Drinkwater, B. W., Dwyer-Joyce, R. S. u. Harper, P.: On-Line Measurement of Lubricant Film Thickness Using Ultrasonic Reflection Coefficients. Review of Quantitative Nondestructive Evaluation Vol. 23 (2004), S. 984–991

[18] Lerch, R., Sessler, G. u. Wolf, D.: Technische Akustik. Berlin, Heidelberg: Springer Berlin Heidelberg 2009

[19] Worden, K.: Rayleigh and Lamb Waves - Basic Principles, Bd. 37. 2001

[20] Lamb, H.: On the Vibrations of an Elastic Sphere, s1-13. 1881

[21] Nazarchuk, Z., Skalskyi, V. u. Serhiyenko, O.: Acoustic Emission. Cham: Springer International Publishing 2017

[22] Yu, L. u. Giurgiutiu, V.: Piezoelectric Wafer Active Sensors in Lamb Wave-Based Structural Health Monitoring, Bd. 64. 2012

[23] Huber, A.: Dispersion Calculator. German Aerospace Center 2023

[24] Vogelpohl, G.: Betriebssichere Gleitlager. Berechnungsverfahren für Konstruktion u. Betrieb. Berlin: Springer 2012

[25] Dowson, D.: Elastohydrodynamic and micro-elastohydrodynamic lubrication, Bd. 190. 1995

[26] Illner, B. u. Bartel, D.: Übergangsdrehzahl von Radialgleitlagern - Analytische Bestimmung unter Berücksichtigung der Lagerdeformation. Antriebstechnik. 2016

[27] Johnson, J. M. u. Khoshgoftaar, T. M.: The Effects of Data Sampling with Deep Learning and Highly Imbalanced Big Data, Bd. 22. 2020

[28] Chandrasekaran, S., Khemchandani, M. V. u. Sharma, J. P.: Effect of abrasive contaminants on scuffing, Bd. 18. 1985

A Simple and Novel Method Determining the Suitability of a Grease Related to the White Etching Crack Phenomenon

Saba Mottaghi[1], Julian Wald[1], Christian Spaeth[1], Walter Holweger[2]

[1] *TUNAP GmbH & Co. KG, Industry@tunap.com*
[2] *National Centre for Advanced Tribology at Southampton (nCATS), University of Southampton, walter.holweger@t-online.de*

Abstract– This paper introduces a simple methodology to predict conflicts in grease-lubricated bearings basically due to the formation of complex structures related to the thickener. In high-speed bearings, especially outer ring rotating deep groove ball bearings (DGBB), centrifugal forces cause grease loss, affecting lubrication. This grease may randomly re-enter the contact zone through incidental vibrations. Hence, the re-entering appears to be crucial and is a matter of structural re-arrangements at low shear rates as being present in the starvation. Traditional rheometry overlooks temperature-induced structural rearrangements in grease. The study examines representative grease candidates (A, B, C, and D) to study the structural rearrangement related to the operational temperature in application. Our methodology highlights changes in the internal structure of the said greases at low shear rates varying the temperature. Future research will focus on predictive computations of grease performance related to WEC.

Keywords – Lubrication, Bearings, Greases, White Etching Cracks, Rheometry

---

1. Introduction

The purpose of lubricants is to support the prevention of damages that might occur in bearings. As such, they are established within the ISO 281 as a part of the scale factor a_{ISO} **[1]**, which states that, in addition to factors describing the presence of impurities, the L10 life expectation is related to the replenishment of the contact zone by the lubricant. For White Etching Crack (WEC) failures it is well accepted, that, running a bearing under boundary lubrication ($\kappa < 1$) is one of the critical factors in bearing operation that may lead to WEC **[2]** **[3]** **[4]**. Even more, when lubricating bearings with greases, the aspect of boundary lubrication due to channelling, churning and starvation caused by centrifugal displacement of the grease under operation is of high importance. Solely bleeding oil out of the grease, as assumed to be important for bearing life may not always compensate these effects. Hence, in addition to oil bleeding properties, it is of importance to know how greases might be susceptible to starvation, especially at the operating temperature. Even more, as stated in early studies, greases might undergo complex structural transformations like hardening under temperature **[5]**. As stated in **[5]** these structural related transformations are seen by the use of rheometrical investigations (cone to plate or plate to plate configuration). This has brought us to study whether WEC damage maybe caused by structural anomalies within the grease at the operational temperature.

The current paper states a novel, but simple methodology to predict conflicts that might appear in the life cycle of grease lubricated bearings. Greases in high-speed bearings, namely outer ring rotating DGBB are exposed to high centrifugal forces leading to grease loss in the contact zone by slinging. This grease will stay out of the contact zone and will not contribute further to lubrication. The re-entry of the grease from starving to the contact, is random and will happen incidentally, e.g., by casual vibration. While standard rheometry simulates the shear and temperature related viscosity, less attention is paid on the aspect of the structural rearrangement caused by temperature and at low shear rates. Grease loss by centrifugal force displacement in sensitive applications such as high-speed bearings may be crucial in regard to White Etching Cracks (WEC). As WEC amongst other causes, e.g. friction and static electricity the aspect of centrifugal force induced grease loss becomes also critical Following this aspect it is presented how to measure the changes in the “inner” structure of a grease, hence the propensity of grease availability in the contact zone by a simple methodology. The methodology applied to the measurements may be an important factor to predict conflicts that appear in the life cycle, namely White Etching Cracks (WEC) in grease lubricated bearings.

2. Structural investigations

In this study the leading hypothesis behind relates to the fact that greases which undergo a structural rearrangement by temperature, may lead to starvation and a lack of lubrication in the contact zone as shown in Figure 1. We have tried to determine the structural change of the grease at low shear rate as a function of temperature in order to prove the hypothesis. The mentioned changes in the grease structure are measured using a rheometer device.

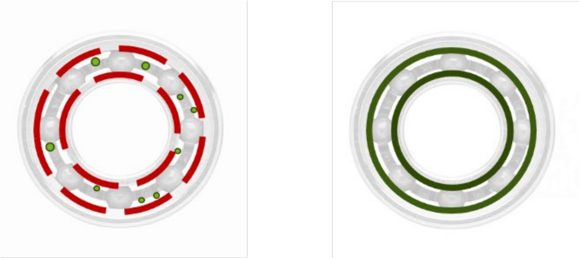

Figure 1: left, failure state (grease unavailability); right, ideal state (balanced grease availability)

2.1. Investigated greases

Within the current investigations four greases (A, B, C and D) are examined with respect to their structural changes under temperature as a measure for the capability to prevent WEC, for example present in high speed DGBB automotive applications. The technical data of the greases are presented in Table 1. This table includes characteristics that are typically found in the data sheets of commodity greases.

The greases are different within their base oil and thickener, but all are commodity standards. Grease A contains a synthetic base oil with a viscosity of approx. 100 mm^2/s at 40°C and a special lithium soap thickener. Grease B is composed by polyalphaolefin with a viscosity of approx. 46 mm^2/s at 40°C and calcium sulphonate complex soap as thickening agent. Grease C, also a polyalphaolefin base with the viscosity of approx. 30 mm^2/s at 40°Cuses lithium soap as a thickener. Lastly, Grease D, an ester-based lubricant with a polyurea thickener and the base oil viscosity of approx. 80 mm^2/ at 40°C.

Table 1: Properties of the used greases.

Characteristics	**Grease A**	**Grease B**	**Grease C**	**Grease D**
Base oil	Synthetic	Polyalphaolefin	Polyalphaolefin	Ester
Thickener	Special lithium soap	Calcium sulfonate complex soap	Lithium soap	Polyurea
Kinematic viscosity of base oil, DIN 51562-1, 40°C	approx. 100 mm^2/s	approx. 46 mm^2/s	approx. 30 mm^2/s	approx. 80 mm^2/s
Viscosity Index, DIN ISO 2909	>130	>130	>130	>130
Worked penetration, DIN ISO 2137, 25°C, [min., max.]	[265-295] x 0.1 mm	[265-295] x 0.1 mm	[310-340] x 0.1 mm	[250-280] x 0,1 mm
FAG rolling bearing testing apparatus FE9, DIN 51821-2	B/1500/6000-160 F50 > 100h	B/1500/6000-140 F50 > 100h	n.d.	B/1500/6000-180 F50 > 100h
Dropping point, DIN ISO 2176, IP 396	>= 180 °C	>= 270 °C	>= 185 °C	>= 250 °C
Flow pressure, DIN 51805-2	< 1400 mbar at -40°C	< 1400 mbar at -50°C	< 1400 mbar at -50°C	< 1400 mbar at -45°C
Shear Viscosity DIN 51810-1, 25 °C, shear rate 300 s^{-1} [min., max.]	[4523-4086] Pa·s	[4581-4367] Pa·s	n.d.	[4966-4382] Pa·s

In the course of these investigations, we found, that grease A passes a WEC test related to an automotive application while greases B, C and D fail, as shown in Table 2. The operational temperature at these tests reaches 120-130°C. The detailed results of WEC testing are confidential and not presented here. Obviously, the standard technical data do not correspond with the propensity of these Greases toward WEC induced failures.

Table 2: WEC test results at 120-140°C

Grease	**WEC failure**
Grease A	No
Grease B	Yes
Grease C	Yes
Grease D	Yes

2.2. Test device and methodology

In this study, the structural characteristics of the mentioned greases were comprehensively investigated using the Modular Compact Rheometer MCR 302 by Anton Paar, as shown in Figure 3. The experimental methodology employed a measurement system consisting of a 25mm diameter cone with a precise 1° angle, paired with a flat plate. A shear rate of 1 s^{-1} was maintained to induce controlled deformation within the greases. The low shear rate reflects the conditions of a starved grease within a bearing, wherein shear stresses are virtually absent. This offers insights into the structural behaviour unaffected by significant shear forces.

A temperature profile ranging from 20°C to 150°C, with a controlled temperature ramp of 1°C per 5 minutes, was employed.

This approach enabled a systematic exploration of the thermal responses of the greases, contributing insights into their structural properties under thermal environments.

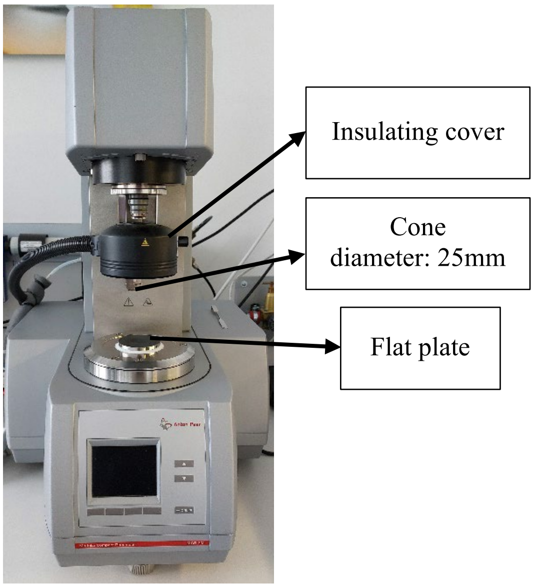

Figure 3: Measurement device MCR 302 by Anton Paar.

2.3. Expected grease behaviour

As the dynamic viscosity describes the flow properties, it is an indicator of the flow behaviour back into the contact zone. It is expected that the dynamic viscosity of the grease decreases by increasing the temperature as shown in Figure 2. Greases with lower dynamic viscosity ensure a better availability.

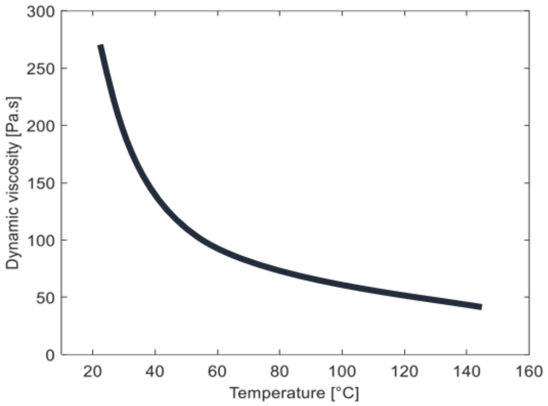

Figure 2: Expected course of dynamic viscosity over temperature

3. Results and discussion

The test results are presented in Figure 4 to Figure 7 within a temperature range in between 20°C and 150°C under the given shear rate of 1 s^{-1}.

Figure 4 shows that the dynamic viscosity of Grease A decreases almost exponentially and thus comes very close to the expected behaviour as shown in Figure 2. Above temperatures of 120°C, the dynamic viscosity increases only slightly.

Figure 5 illustrates that the dynamic viscosity of Grease B steadily decreases until it reaches a temperature of 130°C. Beyond 130°C, the dynamic viscosity rises steeply.

Figure 6 shows that the dynamic viscosity of Grease C is almost similar to Grease A. However, just before reaching temperature of 120°C the dynamic viscosity increases significantly. Notably, the dynamic viscosity of Grease C at 150°C is higher than at 20°C

Figure 7 shows that the dynamic viscosity of Grease D decreases up to 80°C. The dynamic viscosity then changes with temperature, following a U-shaped curve with both exponential decrease and increase. It is worth noting that the dynamic viscosity of Grease D at 150°C is higher than at 20°C.

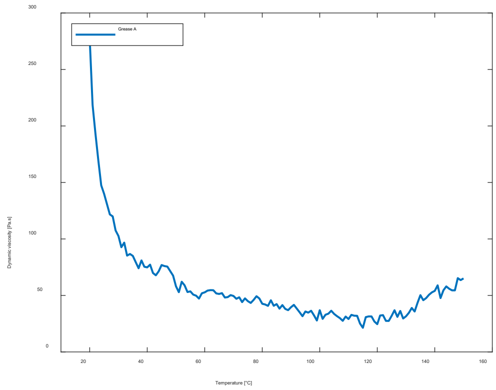

Figure 4: Course of dynamic viscosity over temperature for Grease A.

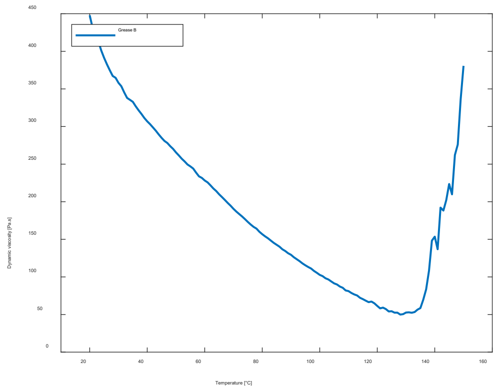

Figure 5: Course of dynamic viscosity over temperature for Grease B.

While Grease A shows a steep exponential drop over the temperature range, greases B, C and D undergo a steep ascent at approximately 100°C, exceeding even values at the start (C and D). The ascent in Grease B is remarkable, however not as massive as seen in C and D, shown as auto scaled y-axis overlay in Figure 8. The measurements are repeatable from batch to batch and do not reflect a production mismatch.

Greases B, C and D cause massive WEC-related failures at an operating temperature of 120°C - 140°C, which occur within about 1/10 of the service life of L10 ISO 281. In contrast Grease A repetitively does not fail under the same conditions. It becomes apparent that a factor indicating the unavailability of the grease must be integrated into the grease life model

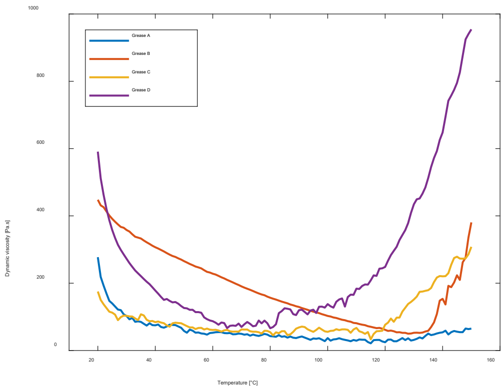

Figure 8: Comparison of dynamic viscosity behaviour over temperature for greases A, B, C, and D.

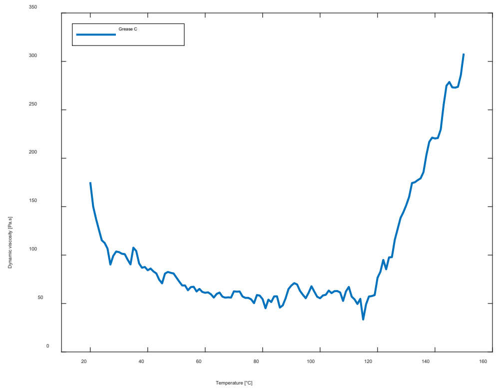

Figure 6: Course of dynamic viscosity over temperature for Grease C.

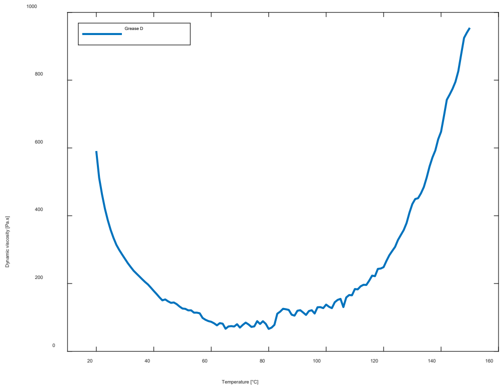

Figure 7: Course of dynamic viscosity over temperature for Grease D.

4. Conclusions and outlook

A novel, but simple methodology to predict conflicts, probably due to the formation of self-organizing suprastructres that might appear in the life cycle grease lubricated bearings is presented. Greases in high-speed bearings, namely outer ring rotating DGBB are exposed to high centrifugal forces leading to grease loss in the contact zone by slinging. This grease will stay and not contribute further to lubrication. The re-entry of the grease from starving to the contact, is random and will happen incidentally, e.g., by casual vibration. While standard rheometry tries to simulate the shear and temperature related viscosity (as G' elastic modulus and G'' viscous modulus) less attention is paid on the aspect of the structural rearrangement of a grease by temperature. Grease loss in high-speed bearings by centrifugal force displacement may be crucial in sensitive applications related to WEC. As WEC is commonly attributed to marginal lubrication, friction and static electricity the aspect of centrifugal force induced grease loss becomes critical. It is notable that none of the standards, applied for characterization of the grease are showing the bias comparing Grease A (WEC pass) and Greases B, C and D (WEC fail). The methodology presented here shows the changes in their “inner” structure by the formation and disruption of long-range interactions, that might occur by thermal and low shear motion. The current results are validated by test rig using outer ring speeded DGBB running at 120°C – 140°C leading to WEC for grease B, C and D while not for Grease A. The test rig configuration stays confidential for compliance reasons and not presented here.

We are suggesting taking standard deviation on viscosity-temperature curves as a measure for predicting WEC. Such results are presented in Figure 9 by comparing the standard deviation for greases A to D with A as the lowest value and D as the highest respectively. Further research, however, is needed to come to a concise understanding of WEC risk prediction.

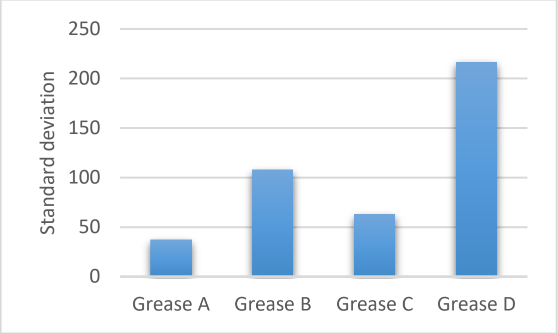

Figure 9: Standard deviation of viscosity in the given temperature range

The reasons for grease unavailability in the contact zone require detailed investigation, as factors such as process chemicals (e.g., base oil, thickener) and the production process (e.g., heating and cooling) have an impact. It became apparent that a factor indicating the unavailability of the grease has to be integrated into the grease life model. However, due to the many parameters that determine grease life, machine learning (ML) tools could be useful as a method in order to take all parameters into account.

Acknowledgment

This research was funded by the German Research Centre, Juelich, at the section of the Bavarian Ministry of Economics supported by TUNAP GmbH & Co. KG and the institute of Process, Machinery and Application Technology at the university of Erlangen, Germany.

References

[1] International Organization for Standardization, “ISO 281:2007: Rolling bearings – Dynamic load ratings and rating life,” *ISO,* 2007.

[2] A. D. Richardson, M.-H. Evans, L. Wang, M. Ingram, Z. Rowland, G. Llanos and R. Wood, “The effect of over-based calcium sulfonate detergent additives on white etching crack (WEC) formation in rolling contact fatigue tested 100Cr6 steel,” vol. Volume 133, pp. 246-262, 2019.

[3] J. Franke, J. Fritz, T. Koenig and D. Merk, “Influence of Tribolayer on Rolling Bearing Fatigue Performed on an FE8 Test Rig—A Follow-up.,” vol. 11, no. 3, p. 123, 2023.

[4] J. Wranik, W. Holweger, T. Lutz, P. Albrecht, B. Reichel and L. Wang, “A Study on Decisive Early Stages in White Etching Crack Formation Induced by Lubrication,” *Lubricants,* vol. 10, no. 5, p. 96, 2022.

[5] D. Klamman, Lubricants and Related Products :synthesis, properties, applications, international Standards, Germany: Verlag Chemie (Wiley-VCH), 1984, p. 389.

Novel analytical calculations in truncated point contact including misalignment

Luc Houpert[a],* and Oliver Menck [b,c]

[a]Luc Houpert Consulting, 1 rue de Fleurie, 68920 Wettolsheim, France

[b] Fraunhofer Institute for Wind Energy Systems IWES, Am Schleusengraben 22, 21029 Hamburg, Germany

[c] Leibniz University Hannover, Institut für Maschinenkonstruktion und Tribologie (IMKT), An der Universität 1,
Gebäude 8143, 30823 Garbse, Germany

*Corresponding author: luc.houpert@orange.fr

ABSTRACT

This paper provides novel analytical relationships for calculating the load and moment in a roller – race contact as a function of the crown profile, central contact deformation and relative roller – race misalignment, the novelty being the derivation of the moment. Past efforts, limited to the calculation of the load only and without misalignment, are first summarized in a chronological or logical order. Hertzian non-truncated point contact calculations required the calculation of complex elliptical integrals, replaced herein by accurate curve-fitted factors called CA, CB, CD, CP, f_1, f_2 and f_3 (function of the equivalent radii ratio k only) used for calculating the contact ellipse dimensions, deformation and maximum pressure as a function of a dimensionless load W and equivalent radius R_{x_eq} for example. Also, a line contact load was defined as a function of the deformation, equivalent roller length and outer race – housing thickness. An initial transition from point to line contact could be suggested as the contact gets truncated at high load. Then, a means of defining the deformation in each slice (using any profile), as well as the derivation of a linear load -deflection model is suggested. This suggestion offers the possibility of calculating analytically (via an integration) a first estimate of the roller load and moment in single crowned contact. The effects on the load and moment of the coupling between slices and pressure spikes at the edges of truncated contact have then been considered using miscellaneous numerical tools and results. The numerical results are used as reference for deriving an appropriate correction factor $Coef_3$ (for the load) and $Coef'_3$ (for the moment). Also, when no misalignment occurs, a single relationship (describing all cases ranging from point to truncated point and line contact) can be suggested for defining a dimensionless load function of a dimensionless deformation or truncation level. Finally, a novel simplified numerical approach (called New Modified Teutsch) is also suggested for calculating the load and contact pressure (including pressure spikes) using any profile.

1. OBJECTIVES

Calculating the rolling element – race contact load and pressure is an important step for correctly defining the bearing stiffness and bearing life.

Standard bearing life can be described using simplified models based on a summation of the roller – race load raised to the exponent 4 for example or using the load and corresponding pressure in each contact slice, especially when the pressure distribution is skewed because of a relative race misalignment.

More advanced numerical calculations also consider pressure spikes at the edge of the contact. Miscellaneous numerical approaches can be described when trying to predict pressure spikes and it is obvious that CPU time increases when using analytical, slices and numerical approaches.

Before calculating the bearing life, several iterations are required for solving the bearings-shaft-housing equilibrium and roller equilibrium between two races (on all loaded rollers).

During these iterations, it is useful and CPU time effective to rely on analytical relationships for correctly describing the roller – race load and moment. Alternatively, analytical relationships for calculating the load and pressure on all roller – race slices are also useful (when using complex profiles) before considering, at the end of this exercise, numerical approaches including pressure spikes.

Houpert developed several rolling element – race contact models, the latest one offering the possibility of calculating analytically the load when single crown profile and zero misalignment are considered. Also, the effect on load of the pressure spikes and coupling between slices were considered. This coupling was included via an appropriate correction factor called *Coef*, defined using a numerical tool (including pressure spikes) and an appropriate curve-fitted relationship.

The objective of this paper is to pursue this analytical effort by including now misalignment when describing the roller load and moment (via refined factors *Coef*), directly on the contact when single crown profile is used, or on each slice when a complex profile is used.

As said above, several approaches have been developed by Houpert and the authors thought that it would be useful to summarize them next in a chronological or logical order before describing the new model developed in the frame of this project.

2. PREVIOUS MODELS

Miscellaneous models have been described distinguishing Hertzian point contact from line contact, and truncated point contact. The use of analytical relationships versus the use of contact slices can also be mentioned.

2.1. Non-truncated point contact (standard point contact)

Standard Hertzian point contact calculations have been described by Tripp [1] or Dalmaz [2].

The point contact geometry is described by 4 radii R_{x1} , R_{y1}, R_{x2} and R_{y2} or their curvatures (inverse of radius), the index *x* corresponding for example to the rolling direction. R_{x1} and R_{y1} are used for describing the rolling element radii, always positive, while the race radius R_{x2} is positive for the inner (convex contact) and negative for outer race (concave contact) respectively. R_{y2} describes the lateral race radii, positive for a TRB (Tapered Roller Bearing, convex contact) and negative for a BB or SRB (Ball Bearing or Spherical Roller Bearing, concave contact).

Four curvatures are therefore used by Hertz, but Houpert suggested in Ref. [3] to use two equivalent radii and their ratio *k*:

$$\frac{1}{R_{x\_eq}}=\frac{1}{R_{x1}}+\frac{1}{R_{x2}} \qquad \frac{1}{R_{y\_eq}}=\frac{1}{R_{y1}}+\frac{1}{R_{y2}} \qquad k=\frac{R_{y\_eq}}{R_{x\_eq}} \tag{1}$$

The elastic contact is described by an ellipse of dimensions *a* and *b*, *a* being larger than *b* when *b* defines half of the contact width in the rolling direction in a rolling element – race contact. Of interest to us is the calculation of the contact dimensions, but also contact pressure P_{max} and deformation δ_{max} to calculate as a function of the applied load *Q* and contact geometry.

Inputs in Hertz initial calculations are the sum of the curvature $\Sigma\rho$ as well as the ratio $\kappa = a/b$.

Hertzian calculations have been done as a function of the parameter $F(\rho)$ and two elliptical integrals, *E* and *F*:

$$\sum\rho=\frac{1}{R_{x1}}+\frac{1}{R_{x2}}+\frac{1}{R_{y1}}+\frac{1}{R_{y2}}=\frac{1}{R_{x\_eq}}+\frac{1}{R_{y\_eq}}=\frac{1}{R_{x\_eq}}.\left(1+k^{-1}\right)$$

$$F(\rho)=\frac{\dfrac{1}{R_{x1}}+\dfrac{1}{R_{x2}}-\dfrac{1}{R_{y1}}-\dfrac{1}{R_{y2}}}{\sum\rho}=\frac{\dfrac{1}{R_{x\_eq}}-\dfrac{1}{R_{y\_eq}}}{\dfrac{1}{R_{x\_eq}}+\dfrac{1}{R_{y\_eq}}}=\frac{1-k^{-1}}{1+k^{-1}} \tag{2}$$

$$\kappa=\frac{a}{b} \qquad \text{(input)}$$

$$E=\int_0^{\frac{\pi}{2}}dE=\int_0^{\frac{\pi}{2}}\left[1-\left(1-\frac{1}{\kappa^2}\right).\sin^2\psi\right]^{\frac{1}{2}}.d\psi \qquad F=\int_0^{\frac{\pi}{2}}dF=\int_0^{\frac{\pi}{2}}\left[1-\left(1-\frac{1}{\kappa^2}\right).\sin^2\psi\right]^{-\frac{1}{2}}.d\psi \tag{3}$$

Hertz showed that the contact dimensions, maximum contact deformation and pressure are finally defined by:

$$a=a^*.\left(\frac{3.Q}{2.E_{eq}.\sum\rho}\right)^{\frac{1}{3}} \quad b=b^*.\left(\frac{3.Q}{2.E_{eq}.\sum\rho}\right)^{\frac{1}{3}} \quad \delta_{\max}=\delta^*.\left(\frac{3.Q}{2.E_{eq}.\sum\rho}\right)^{\frac{2}{3}}.\frac{\sum\rho}{2} \quad P_{\max}=\frac{3}{2}.\frac{Q}{\pi.a.b}$$

with

$$E_{eq}=\frac{1}{2}.\left(\frac{1-\upsilon_1^2}{E_1}+\frac{1-\upsilon_2^2}{E_2}\right)\approx 2.26*10^5\ \text{N/mm}^2 \ \text{ when } \upsilon_1=\upsilon_2=0.3 \text{ and } E_1=E_2\approx 2.06*10^5\ \text{N/mm}^2 \tag{4}$$

and with a^*, b^*, and d^* defined as a function of the elliptical integrals and the input $\kappa = a/b$:

$$a^*=\left[2.\kappa^2.\frac{E}{\pi}\right]^{\frac{1}{3}} \qquad b^*=\frac{a^*}{\kappa} \qquad \delta^*=\frac{2.F}{\pi}.\left[\frac{\pi}{2.\kappa^2.E}\right]^{\frac{1}{3}} \tag{5}$$

Using the *k* ratio and equivalent radius ratio R_{x_eq}, one can introduce Houpert's factors *CA*, *CB*, *CD* and *CP* (only function of *k*) used for calculating *a*, *b*, δ and P_{max} as a function of the non-truncated dimensionless load W_{NT}:

$$
\begin{aligned}
&W_{NT}=\frac{Q}{E_{eq}.R_{x\_eq}^{2}}\\
&\frac{a}{R_{x\_eq}}=\left(\frac{3.k}{1+k}\right)^{\frac{1}{3}}.a^{*}.W_{NT}^{\frac{1}{3}} \qquad =CA.W_{NT}^{\frac{1}{3}}\quad \text{with}\quad CA=\left(\frac{3.k}{1+k}\right)^{\frac{1}{3}}.a^{*}=\left(\frac{3.k}{1+k}\right)^{\frac{1}{3}}.\left[2.\kappa^{2}.\frac{E}{\pi}\right]^{\frac{1}{3}}\\
&\frac{b}{R_{x\_eq}}=\left(\frac{3.k}{1+k}\right)^{\frac{1}{3}}.b^{*}.W_{NT}^{\frac{1}{3}} \qquad =CB.W_{NT}^{\frac{1}{3}}\quad \text{with}\quad CB=\left(\frac{3.k}{1+k}\right)^{\frac{1}{3}}.b^{*}=\left(\frac{3.k}{1+k}\right)^{\frac{1}{3}}.\frac{a^{*}}{\kappa}\\
&\frac{\delta_{\max}}{R_{x\_eq}}=\left(\frac{3^{2}.(1+k)}{k}\right)^{\frac{1}{3}}.\frac{\delta^{*}}{2}.W_{NT}^{\frac{2}{3}}=CD.W_{NT}^{\frac{2}{3}}\quad \text{with}\quad CD=\left(\frac{3^{2}.(1+k)}{k}\right)^{\frac{1}{3}}.\frac{\delta^{*}}{2}=\left(\frac{3^{2}.(1+k)}{k}\right)^{\frac{1}{3}}.\frac{F}{\pi}.\left[\frac{\pi}{2.\kappa^{2}.E}\right]^{\frac{1}{3}}\\
&\frac{P_{\max}}{E_{eq}}=\frac{1.5}{\pi.a^{*}.b^{*}}.\left(\frac{1+k}{3.k}\right)^{\frac{2}{3}}.W_{NT}^{\frac{1}{3}}=CP.W_{NT}^{\frac{1}{3}}\quad \text{with}\quad CP=\frac{1.5}{\pi.a^{*}.b^{*}}.\left(\frac{1+k}{3.k}\right)^{\frac{2}{3}}
\end{aligned}
\tag{6}
$$

In his initial effort, Houpert [3] did not calculate any elliptical integrals but simply used Dalmaz's results [2] giving in a table a^{*}, b^{*} and d^{*} as a function *F(ρ)*. The corresponding *k* values (defined using eq. (2) were ranging from 1 to 13577. Houpert curve-fitted in [3] the corresponding four factors *CA*, *CB*, *CD* and *CP* as a function of *k*, in three ranges of *k*, perhaps not well selected since *k* is of the order of 25 for ball bearings range, 300 for spherical roller bearings, 1500 for tapered or cylindrical roller bearings and 15000 for needle roller bearings.

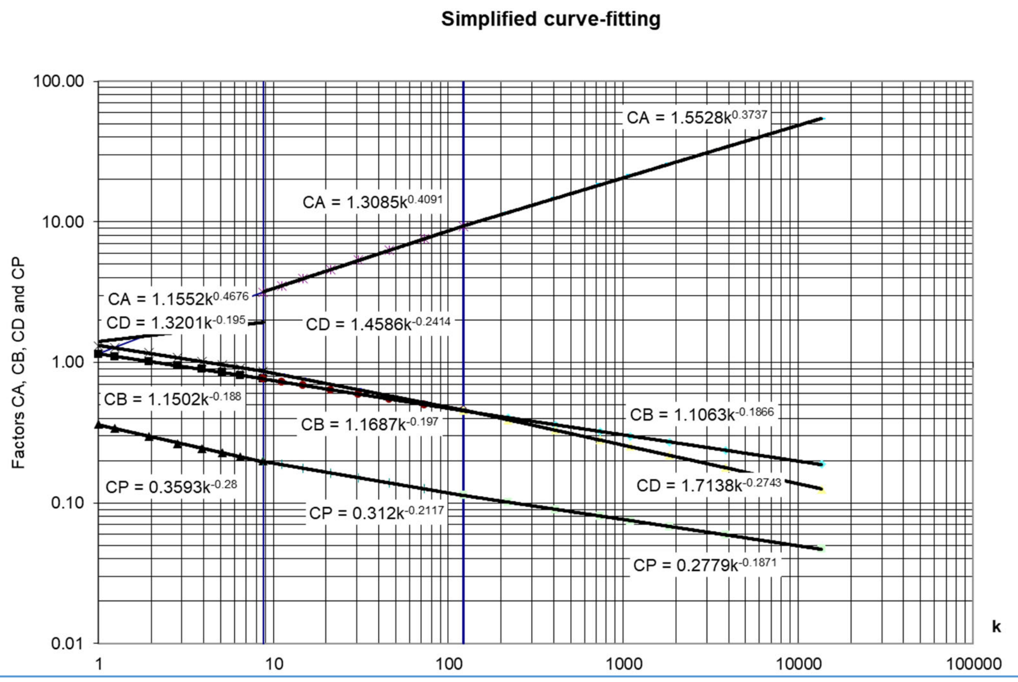

Figure 1 : Simplified curve-fitting of the factors CA, CB, CD and CP initially suggested in [3].

Later on, Houpert calculated himself in [4] the two elliptical integrals *E* and *F* in a very large range of *k*, see for example Fig. 2 and 3, via a summation of the *dF* and *dE* values in each slice plotted next as an example corresponding to k=1*10^{7}. A sharp increase of *dF* can be noticed near $\psi=\pi/2$, explaining why the integration has been conducted using 10000 slices in two ranges or two steps, see the appendix of [4], the last range corresponding to ψ values close to $\pi/2$, see the following Figures.

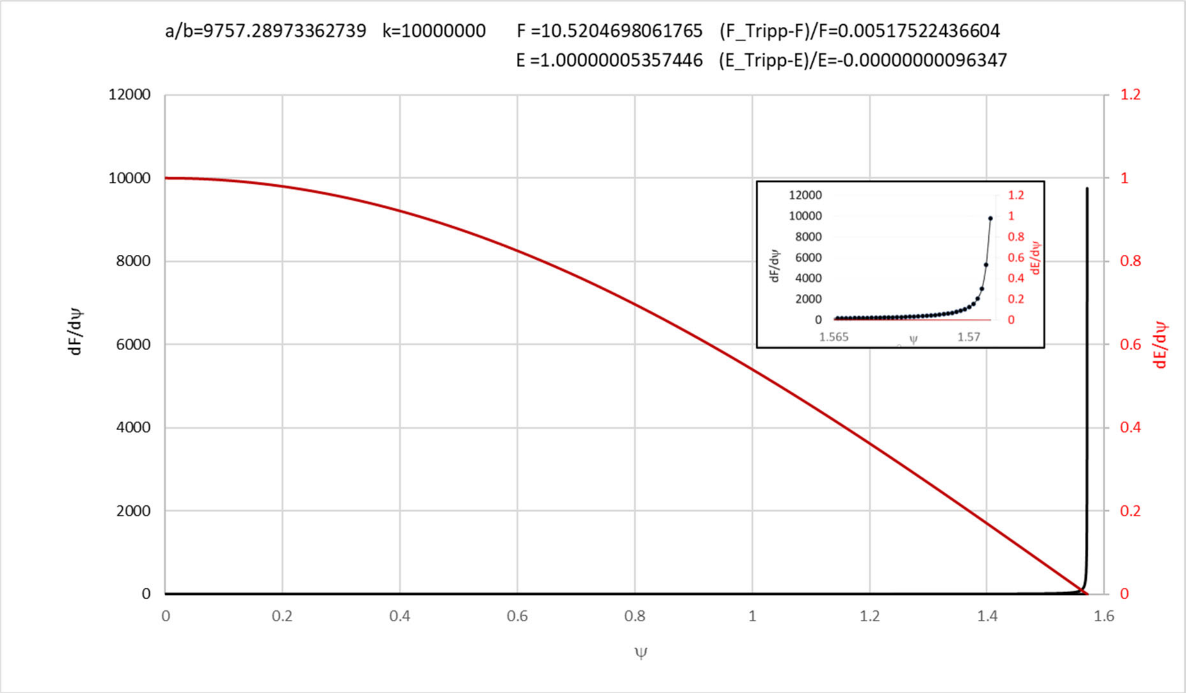

*Fig. 2: dF/dψ & dE/dψ distribution for k = 1*107 as shown in [4]*

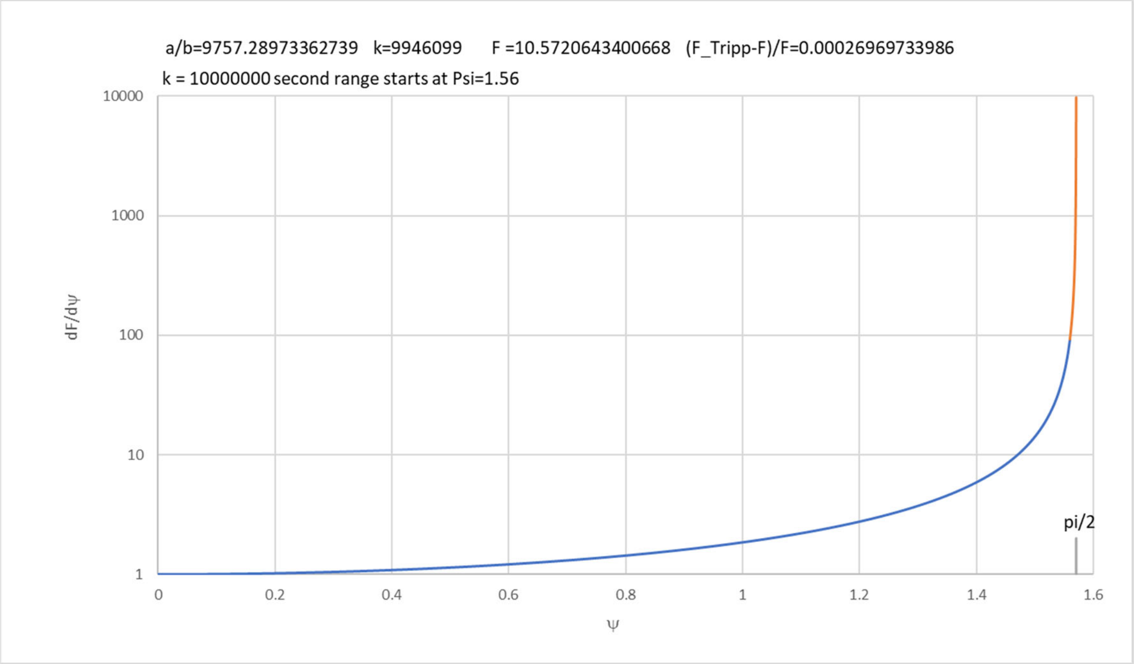

*Fig. 3: dF/dψ distribution for k = 1*10^7 using a log scale*

The calculated integrals can be compared to some asymptotic analytical values of E_{Tripp} and F_{Tripp} defined by Tripp [1] using expansion series expansion valid at large κ values only.
For large κ or k values only, Tripp suggested indeed two analytical relationships for calculating E and F:

$$\Lambda = \ln(4.\kappa)$$

$$At\ \text{large}\ \kappa: \tag{7}$$

$$E_{Tripp} \approx 1 + 0.5*(\Lambda - 0.5).\kappa^{-2} \qquad F_{Tripp} \approx \Lambda + 0.25*(\Lambda - 1).\kappa^{-2}$$

Houpert has also been able to impose in [4] the k ratio as input. The previous input ($\kappa = a/b$) is then an unknown that can be calculated using iterations on κ until the new value of κ is equal to the previous one used for defining E and F:

$$\kappa_{new} = \left[(k+1).\frac{F}{E} - k \right]^{\frac{1}{2}} \tag{8}$$

The next figure shows the accuracy of Houpert’s numerical integration versus Tripp’s analytical solution.

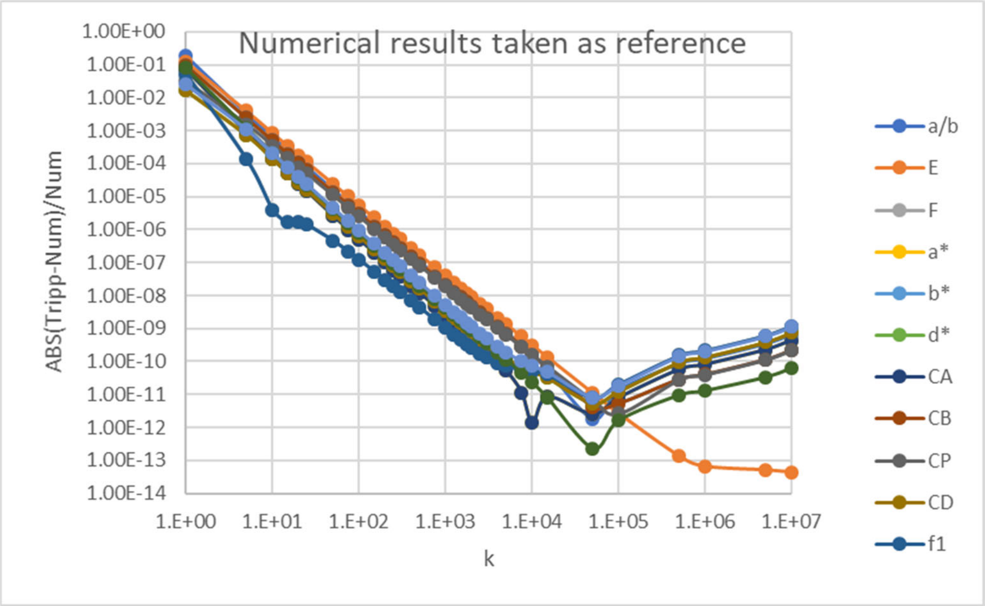

Fig. 4: Difference of Tripp’s results to those obtained using a numerical integration in two steps; [4]

One sees that Tripp’s error is large (of the order of 10%) when *k* is very small (which is expected) and that Houpert’s numerically calculated integrals is equal to Tripp’s ones (error < $1*10^{-10}$) when *k* is of the order of 3000. Above this value, the relative error increases versus *k* because of the limitation of the numerical integration, indicating that Tripp’s solution can or should be kept when *k* > 3000.

The following very accurate table, taken from [4], can therefore be suggested:

FINAL Proposal using two steps integration and Tripp's results when k > 3000

k	CA	CB	CP	CD	r	f1	f2	f3
1.00E+00	1.14471424	1.14471424	0.36437386	1.31037070	1.4142	0.50000000	2.00000000	0.66666667
5.00E+00	2.46053706	0.85134358	0.22793269	0.96781720	1.2643	0.31494739	5.00222517	1.05029184
1.00E+01	3.33986185	0.74228269	0.19259435	0.83322566	1.2223	0.26950705	7.31774349	1.31478896
1.50E+01	3.97089212	0.68467792	0.17561717	0.75999140	1.2025	0.24852180	9.10990283	1.50933965
2.00E+01	4.47978509	0.64655670	0.16484569	0.71072964	1.1902	0.23555897	10.62759414	1.66895012
2.50E+01	4.91342257	0.61851121	0.15711212	0.67411249	1.1816	0.22643564	11.96872603	1.80676406
5.00E+01	6.51084808	0.53937279	0.13596114	0.56937293	1.1589	0.20231444	17.25715303	2.32758086
7.50E+01	7.65098079	0.49822729	0.12525549	0.51436526	1.1481	0.19057789	21.33591598	2.71076928
1.00E+02	8.56832945	0.47112118	0.11828035	0.47805893	1.1412	0.18309803	24.78480088	3.02536546
1.50E+02	10.03544718	0.43562375	0.10921772	0.43058469	1.1325	0.17356652	30.58703869	3.53925718
2.00E+02	11.21529527	0.41221732	0.10327720	0.39941868	1.1270	0.16742572	35.49167710	3.96147977
2.50E+02	12.21896450	0.39500829	0.09892380	0.37662196	1.1231	0.16297509	39.82094651	4.32654813
3.00E+02	13.10133968	0.38152865	0.09552093	0.35885723	1.1200	0.15952320	43.74061196	4.65176168
4.00E+02	14.61741123	0.36126617	0.09041565	0.33234251	1.1155	0.15438493	50.71162320	5.21940687
5.00E+02	15.90668494	0.34635345	0.08666469	0.31300298	1.1122	0.15063750	56.86374232	5.71054147
7.50E+02	18.53194145	0.32093108	0.08028024	0.28045362	1.1068	0.14430431	69.98748602	6.73299723
1.00E+03	20.64104761	0.30411515	0.07606268	0.25926943	1.1032	0.14014519	81.07483456	7.57483225
1.25E+03	22.43391678	0.29172286	0.07295681	0.24386336	1.1006	0.13709121	90.85771703	8.30386271
1.50E+03	24.00922260	0.28199847	0.07052069	0.23190916	1.0986	0.13469928	99.71239398	8.95412491
1.75E+03	25.42388151	0.27404636	0.06852917	0.22222892	1.0970	0.13274520	107.86276927	9.54551016
2.00E+03	26.71409639	0.26735087	0.06685275	0.21414898	1.0956	0.13110063	115.45492918	10.09080897
2.50E+03	29.01273490	0.25654714	0.06414836	0.20125597	1.0934	0.12844695	129.34340063	11.07584397
3.00E+03	31.03197496	0.24806372	0.06202528	0.19126505	1.0917	0.12636192	141.91281072	11.95491713
4.00E+03	34.49819571	0.23527614	0.05882570	0.17644312	1.0891	0.12321403	164.25704841	13.49251507
5.00E+03	37.44302076	0.225837215	0.056464436	0.165699204	1.0871	0.120884317	183.9673121	14.82584193
7.50E+03	43.43223094	0.209691781	0.052426135	0.147742567	1.0839	0.116880883	225.9900473	17.60927753
1.00E+04	48.23784308	0.198974222	0.049745831	0.136139846	1.0817	0.114205792	261.4720362	19.90774728
1.50E+04	55.90271418	0.184832185	0.04620946	0.121251917	1.0789	0.110647029	321.0839401	23.684656
5.00E+04	86.38684272	0.148687643	0.037172255	0.085680874	1.0715	0.101328071	590.2495361	39.8725647
1.00E+05	110.8118104	0.131282444	0.032820764	0.070013827	1.0679	0.096669929	837.5758337	53.97893067
5.00E+05	196.8368809	0.098502499	0.024625648	0.043596129	1.0608	0.08739908	1885.439089	109.8570946
1.00E+06	251.7627473	0.087097332	0.021774343	0.035485213	1.0582	0.083950324	2672.992597	149.5990631
5.00E+06	444.6916228	0.065534682	0.016383672	0.021922461	1.0529	0.07693306	6006.815447	308.0817944
1.00E+07	567.6039966	0.058006673	0.014501669	0.017791102	1.0509	0.074269923	8510.871175	421.4011625

Table 1: Results obtained using the two-step integration process and Tripp’s models when k > 3000

Also shown in the latter table are the ratio *r* and the factors *f₁, f₂* and *f₃* explained later.

2.1.1. Curve-fitting of all factors:

Single powerful curve-fitted relationships, valid in the entire range of *k* has also been suggested in [4].
Each factor can be calculated using:

$$V_{cf} = V_{k=1} * k^{a_0 + a_1.X + a_2.X^2 + a_3.X^3 + a_4.X^4 + a_5.X^5 + a_6.X^6} \quad with \;\; X = \ln(k) \tag{9}$$

and:

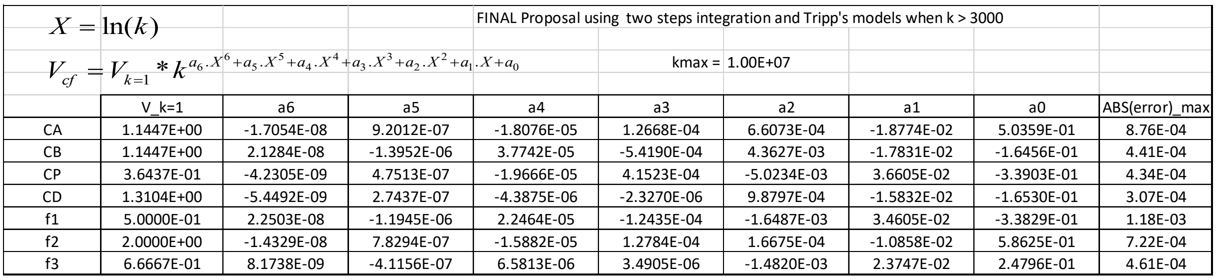

$$X = \ln(k)$$

$$V_{cf} = V_{k=1} * k^{a_6.X^6 + a_5.X^5 + a_4.X^4 + a_3.X^3 + a_2.X^2 + a_1.X + a_0}$$

FINAL Proposal using two steps integration and Tripp's models when k > 3000

kmax = 1.00E+07

	V_k=1	a6	a5	a4	a3	a2	a1	a0	ABS(error)_max
CA	1.1447E+00	-1.7054E-08	9.2012E-07	-1.8076E-05	1.2668E-04	6.6073E-04	-1.8774E-02	5.0359E-01	8.76E-04
CB	1.1447E+00	2.1284E-08	-1.3952E-06	3.7742E-05	-5.4190E-04	4.3627E-03	-1.7831E-02	-1.6456E-01	4.41E-04
CP	3.6437E-01	-4.2305E-09	4.7513E-07	-1.9666E-05	4.1523E-04	-5.0234E-03	3.6605E-02	-3.3903E-01	4.34E-04
CD	1.3104E+00	-5.4492E-09	2.7437E-07	-4.3875E-06	-2.3270E-06	9.8797E-04	-1.5832E-02	-1.6530E-01	3.07E-04
f1	5.0000E-01	2.2503E-08	-1.1945E-06	2.2464E-05	-1.2435E-04	-1.6487E-03	3.4605E-02	-3.3829E-01	1.18E-03
f2	2.0000E+00	-1.4329E-08	7.8294E-07	-1.5882E-05	1.2784E-04	1.6675E-04	-1.0858E-02	5.8625E-01	7.22E-04
f3	6.6667E-01	8.1738E-09	-4.1156E-07	6.5813E-06	3.4905E-06	-1.4820E-03	2.3747E-02	2.4796E-01	4.61E-04

Table 2: Curve-fitted results obtained using the very large k range ($k_{max} = 1*10^7$).

Simplified curve-fitted relationships can of course be suggested when narrowing the *k* range. For example, when using 5 < k < 50 (applicable to ball bearing), Houpert recently suggested in [5]:

$$\begin{gathered} For\;\; 5 \le k \le 50 \;\; (applicable\; to\; ball\; bearing): \\ CA \approx 1.2568 * k^{0.4227} \quad CB \approx 1.1716 * k^{-0.198} \quad CD \approx 1.4116 * k^{-0.23} \quad CP \approx 0.3243 * k^{-0.224} \end{gathered} \tag{10}$$

In summary, when studying non-truncated point contact, the following relationships are suggested:

$$\begin{gathered} W_{NT} = \frac{Q}{E_{eq}.R_{x\_eq}^2} \quad k = \frac{R_{y\_eq}}{R_{x\_eq}} \qquad CA, CB, CD\; and\; CP\; defined\;\; as\;\; a\;\; function\;\; of\;\; k\;\; and: \\ \frac{a}{R_{x\_eq}} = CA.W_{NT}^{\frac{1}{3}} \qquad \frac{b}{R_{x\_eq}} = CB.W_{NT}^{\frac{1}{3}} \qquad \frac{\delta_{\max}}{R_{x\_eq}} = CD.W_{NT}^{\frac{2}{3}} \qquad \frac{P_{\max}}{E_{eq}} = CP.W_{NT}^{\frac{1}{3}} \end{gathered} \tag{11}$$

$$W_{NT}^{\frac{1}{3}} = \left(\frac{1}{CD} . \frac{\delta_{\max}}{R_{x\_eq}} \right)^{\frac{1}{2}}$$

$$\frac{a}{R_{x\_eq}} = CA.\left(\frac{1}{CD} . \frac{\delta_{\max}}{R_{x\_eq}} \right)^{\frac{1}{2}} = \frac{f_2}{2.R_{x\_eq}} . \sqrt{R_{x\_eq}.\delta_{\max}} \qquad \frac{b}{R_{x\_eq}} = CB.\left(\frac{1}{CD} . \frac{\delta_{\max}}{R_{x\_eq}} \right)^{\frac{1}{2}} \qquad \frac{P_{\max}}{E_{eq}} = CP.\left(\frac{1}{CD} . \frac{\delta_{\max}}{R_{x\_eq}} \right)^{\frac{1}{2}}$$

In the latter, *a, b* and P_{max} are also defined as a function of δ_{max}, a useful point used later.
The Hertzian non-truncated point contact stiffness is non-linear and can be easily derived using:

$$W_{NT} = \left(\frac{1}{CD} . \frac{\delta_{\max}}{R_{x\_eq}} \right)^{\frac{3}{2}} \qquad Q = \frac{E_{eq}.R_{x\_eq}^{0.5}}{CD^{\frac{3}{2}}} . \delta_{\max}^{\frac{3}{2}} = f_3.E_{eq}.\sqrt{R_{x\_eq}} . \delta_{\max}^{1.5} = K_{PC}.\delta_{\max}^{1.5} \tag{12}$$

Note also the introduction in the previous relationships of some useful factors (*f₂* and *f₃*) described and curve-fitted in Table 1 and 2 respectively, factors that will be used later for calculating *a* and *Q* as a function of *δ*.
It is also useful to mention that the mean contact pressure is equal to $P_{max}/1.5$ while the contact area is equal to *π.a.b*, leading to:

$$Q = \frac{P_{\max}}{1.5}.\pi.a.b = \frac{2}{3}.\pi.E_{eq}.R_{x\_eq}^{2}.CP.CA.CB.W_{NT} = \frac{2}{3}.\pi.CP.CA.CB.Q \Rightarrow$$

$$\frac{2}{3}.\pi.CP.CA.CB = 1 \tag{13}$$

The latter product will be used in eq. (30). It can also be used for checking in Table 1 the accuracy of *CP*, *CA* and *CB* whose product should be equal to 1.5/π.

2.2. Line contact

Line contact relationships are available for the contact half width b and maximum pressure P_{max}, but not for the elastic deformation δ (assumed uniform along the contact length):

$$\frac{P_{\max}}{E_{eq}} = \sqrt{\frac{W_{LC}}{2.\pi}} \qquad \frac{b}{R_{x\_eq}} = \sqrt{\frac{8}{\pi}.W_{LC}} \qquad W_{LC} = \frac{Q}{E_{eq}.R_{x\_eq}.L} \tag{14}$$

where L is the effective race or roller length and W_{LC} the dimensionless load.

Several semi-empirical relationships are described in [3] (published by Timken, FAG or Harris) leading to surprising variations (of the order of 30%) of the calculated deformation in some selected examples. The most widely used relationship is the so-called Palmgren relationship which reads (when studying a single roller – race contact and assuming the deformation at both contact to be equal):

$$\delta_{Palmgren} \approx 2.59 * \left(\frac{Q}{E_{eq}}\right)^{0.9}.\frac{1}{L^{0.8}} \qquad Q_{Palmgren} \approx 0.347 * E_{eq}.L^{\frac{0.8}{0.9}}.\delta^{\frac{10}{9}} \tag{15}$$

In the latter relationship, the equivalent Young modulus E_{eq}, initially missing, has been introduced and fixed to $2.261*10^5$ N/mm^2.

The Palmgren load will be shown later as slightly too large in the examples considered.

More rigorous calculations of the deformation in line contact have been conducted by Houpert in [3] using some analytical models suggested by Tripp [1]:

The deformation of a rigid cylinder on an elastic half space reads:

$$\delta_1 = \frac{2.(1-\upsilon_1^2).Q}{\pi.E_1 L}.\left\{\ln\left(\frac{2.d_1}{b}\right) - \frac{\upsilon_1}{2.(1-\upsilon_1)}\right\} \tag{16}$$

while the deformation of a rigid flat surface on an elastic circular cylinder is:

$$\delta_2 = \frac{2.(1-\upsilon_2^2).Q}{\pi.E_2 L}.\left\{\ln\left(\frac{2.d_2}{b}\right) - \frac{1}{2}\right\} \tag{17}$$

so that the total roller - race deformation is equal to d_1+d_2.

In the latter, d_1 and d_2 represent the depth corresponding to zero deformation.

d_2 has been defined in [3] as equal to the roller diameter (although one could debate if the roller radius should be used instead of the diameter, but the effect of d_2 on δ will be shown as small) while d_1 has been defined as equal to the inner race diameter (again, one could debate if the inner race radius, instead of the diameter, should be used). When studying the roller – outer race contact, d_2 can also be fixed as equal to the outer race – housing section thickness t, an interesting novelty although the effect of t on δ will be shown to be small.

By scanning on some dimensionless terms and curve-fitting the results obtained, the following relationships have finally been suggested in [3].

At the roller – inner race contact:

$$\delta_i \approx 3.3576 * \left(\frac{d_m}{\cos\alpha_i}\right)^{0.0689}.\left(\frac{Q}{E_{eq}.L}\right)^{0.9311} \qquad Q \approx 0.2723 * E_{eq}.L.\left(\frac{\cos\alpha_i}{d_m}\right)^{0.074}.\delta_i^{1.074} \tag{18}$$

showing a small effect of the bearing pitch diameter d_m and roller – inner race contact angle α_i.

Also, the final exponent applied on the deformation is now 1.074 instead of 1.111 usually accepted.

At the roller – outer race contact, the deformation has been defined as a function of t and validated experimentally:

$$\delta_o \approx 3.2734 * \left(\frac{Q}{E_{eq}.L}\right)^{0.9276} . \left(\frac{t}{1+\dfrac{D.\cos\alpha_o}{d_m}}\right)^{0.07236} \qquad Q \approx 0.2785 \;\; E_{eq}.L.\left(\frac{1+\dfrac{D.\cos\alpha_o}{d_m}}{t}\right)^{0.078} .\delta_o^{1.078} \tag{19}$$

showing a minor effect of the outer race – housing section thickness *t*.

In summary, the Hertzian line contact stiffness is slightly non-linear and can be written:

$$Q = K_{LC}.\delta^{n} \tag{20}$$

where miscellaneous models are available for defining K_{LC} and n, with n being of the order of 1.1

2.3. Truncated point contact load; initial model

Houpert studied in [3] a standard roller – race contact using a single crown equivalent radius (or *k* ratio) and effective roller length *L*.

When increasing the deformation, the contact ellipse length 2**a* increases until reaching its maximum length *L*.

When further increasing the deformation, the contact is truncated and calculating the load 'exactly' requires a numerical approach with a double integration of the pressure over the contact area:

$$\delta(x,y) = \frac{1-\upsilon}{2.\pi.G}.\iint_A \frac{P(x,y)}{\sqrt{(x-x')^2+(y-y')^2}}.dx'.dy' \approx \sum_j \sum_i A(i,j).P(i,j) \tag{21}$$

where *G* is the elastic shear modulus.

Several authors (for example Hoeprich [6], Cretu [7], Reusner [8] and Guo [9]) developed appropriate numerical tools. Using a few examples, the authors had the opportunities of comparing their analytical results to some numerical results obtained initially by Cretu and Hoeprich and later, in the frame of this project, Reusner and Guo, see Table 4 given next in chapter "5.NEW MODELS". Showing the details of the numerical models and results is not the scope of this chapter devoted to simplified analytical approaches for defining the load. It can however be said that similar results have been obtained using for example Hoeprich's tool (called CST), Cretu's tool and Guo's tool.

As described in [3], when zero misalignment is assumed, Hoeprich also suggested a simplified approach for calculating analytically the load above a certain transition level defined by the deformation δ_T and the load Q_T.

The deformation δ_T corresponds to the deformation where the point contact local slope ($dQ/d\delta$) is equal to the line contact one leading to:

$$\frac{dQ}{d\delta} = 1.5 * K_{PC}.\delta_T^{0.5} = n.K_{LC}.\delta_T^{n-1}$$

$$\delta_T = \left(n.\frac{K_{LC}}{K_{PC}}\right)^{\frac{1}{1.5-n}} \qquad Q_T = K_{PC}.\delta_T^{1.5} \qquad \Delta Q = K_{LC}.\delta_T^{n} - K_{PC}.\delta_T^{1.5} \tag{22}$$

Below δ_T, a standard non-truncated point contact occurs. Above this value, the behavior tends towards a line contact. To avoid any discontinuity at the transition, use is made of a load translation ΔQ by writing:

$$\begin{aligned} &if \;\; \delta \le \delta_T : Q_{PC\_LC} = Q_{PC} &&= K_{PC}.\delta^{1.5} \\ &if \;\; \delta > \delta_T : Q_{PC\_LC} = Q_{LC} - \Delta Q &&= K_{LC}.\delta^{n} - \Delta Q \end{aligned} \tag{23}$$

The following figure shows a TRB example extracted from [3] with a satisfactory match between Cretu's numerical results and the simplified suggested truncated point contact load calculated analytically, the selected line contact model being described by eq. (18).

It should however be reminded that this simplified approach can only be used when no roller – race misalignment occurs. Also, a minor inconsistency will be demonstrated later, the inconsistency being that the load of transition does not exactly correspond to *2*a=L* at the transition.

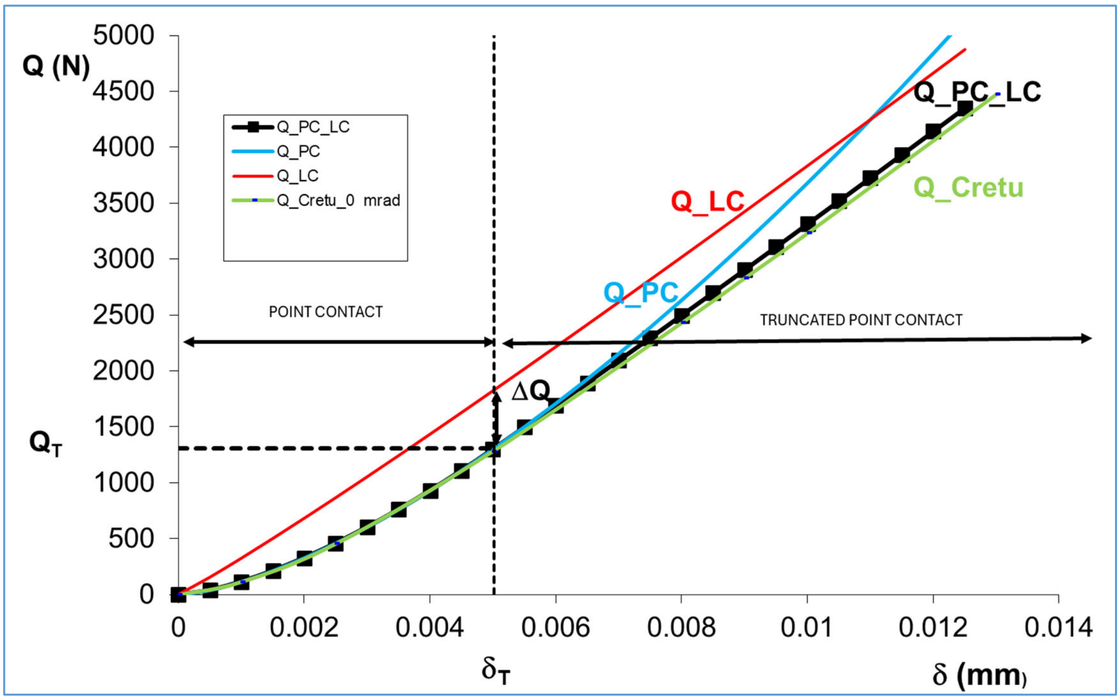

Fig. 5: Example of load calculated using a non-truncated and truncated point contact initial model.

In the latter, Q_{Cretu} corresponds to the numerical solution while Q_{PC_LC} has been obtained using the previously defined point to line contact transition model with Q_{LC} described using eq. (18).

2.4. Load in slices

Let's first calculate the load dQ on a slice of width dy and located at the contact center submitted to the maximum deformation δ_{max}.

Using equation (11), we know that P_{max} and b can be calculated as a function of δ_{max} so that the load dQ in this center slice is a linear function of the maximum deformation.

$$P_{\max} = E_{eq}.\frac{CP}{\sqrt{CD}}.\left(\frac{\delta_{\max}}{R_{x\_eq}}\right)^{\frac{1}{2}} \quad b = \frac{CB}{\sqrt{CD}}.\left(R_{x\_eq}.\delta_{\max}\right)^{\frac{1}{2}}$$

$$\bar{P}_{\max} = \frac{\pi}{4}.P_{\max} \tag{24}$$

$$dQ = \bar{P}_{\max}.2.b.dy = \frac{\pi}{2}.E_{eq}.\frac{CP.CB}{CD}.dy.\delta_{\max} = E_{eq}.f_1.dy.\delta_{\max}$$

Note in the latter the introduction of the factor f_1, shown in Table 1 and curve-fitted in Table 2 as a function of k.

One will now demonstrate that the latter linear load – deformation relationship can be used in any slice (providing the deformation in each slice is known) for retrieving the final load applied on the point contact. This final load is obtained by an analytical integration and will be shown equal the non-truncated Hertzian analytical load, a non-linear function of the central deformation.

For calculating the deformation in any slice, one can use as a starting point the geometrical interference Δ calculated at any abscissa y using a single crown radius $R_{y\_eq}=k*R_{x\_eq}$ with no misalignment:

$$\Delta = \Delta_{\max} - \frac{y^2}{2.R_{y\_eq}} = \delta_{\max} - \frac{y^2}{2.R_{y\_eq}}$$

$$\Delta = 0 \ when \ \ y = A_{geom} = \sqrt{2.R_{y\_eq}.\delta_{\max}} = \sqrt{2.R_{y\_eq}.\delta_{\max}} = \sqrt{2.k.R_{x\_eq}.\delta_{\max}} \tag{25}$$

The geometrical length A_{geom} can be compared to the elastic length a, via their ratio r:

$$a = \frac{CA}{\sqrt{CD}}.\left(R_{x\_eq}.\delta_{\max}\right)^{\frac{1}{2}} \qquad r = \frac{A_{geom}}{a} = \frac{\sqrt{2.k.CD}}{CA} \tag{26}$$

One sees that the geometrical interference is nil at abscissa $y=A_{geom}$ while the elastic deformation is nil at the abscissa $y=a$. The ratio $r = A_{geom}/a$ is always larger than 1, decreasing from $\sqrt{2}$ to 1 as k increases from 1 to infinity, see table1.

It is possible to estimate the deformation at any abscissa and to retrieve a deformation nil at abscissa a by replacing the abscissa y by the product $r.y$, leading to:

$$\delta = \delta_{\max} - \frac{(r.y)^2}{2.R_{y\_eq}} \tag{27}$$

Using the latter, one can test the use of the linear relationship applied in any slice.

$$\begin{gathered} Y = \frac{y}{a} \qquad dy = a.dY \\ dQ = \frac{\pi}{2}.E_{eq}.a.\frac{CP.CB}{CD}.dY.\delta = \\ dQ = \frac{\pi}{2}.E_{eq}.a.\frac{CP.CB}{CD}.\left(\delta_{\max} - \frac{r^2.a^2.Y^2}{2.R_{y\_eq}}\right).dY \\ Q_{\text{integral}} = \frac{\pi}{2}.E_{eq}.\frac{CP.CB}{CD}.a.\int_{-1}^{1}\left(\delta_{\max} - \frac{r^2.a^2.Y^2}{2.R_{y\_eq}}\right).dY = \pi.E_{eq}.\frac{CP.CB}{CD}.a.\delta_{\max}.\left(1 - \frac{1}{3}.\frac{r^2.a^2}{2.k.R_{x\_eq}.\delta_{\max}}\right) \end{gathered} \tag{28}$$

Using $A_{geom} = r.a = \sqrt{2.k.R_{x\_eq}.\delta_{\max}}$, one obtains after integration:

$$Q_{\text{integral}} = \pi.E_{eq}.\frac{2}{3}.\frac{CP.CB}{CD}.a.\delta_{\max} \tag{29}$$

Using now W_{NT} and eq. (11), one obtains:

$$\begin{gathered} a = CA.R_{x\_eq}.W_{NT}^{\frac{1}{3}} \qquad \delta_{\max} = CD.R_{x\_eq}.W_{NT}^{\frac{2}{3}} \\ Q_{\text{integral}} = \pi.E_{eq}.\frac{2}{3}.CP.CB.CA.R_{x\_eq}^{2}.W_{NT} = \frac{2}{3}.\pi.CP.CB.CA.Q = Q_{Hertz} \end{gathered} \tag{30}$$

$$\begin{gathered} because: \\ \frac{2}{3}.\pi.CP.CB.CA = 1 \text{ as shown in (13)} \end{gathered}$$

The latter demonstration is important because it shows that a linear load – deformation model can be used for calculating analytically the load dQ, moment dM as well as, after an analytical integration, the final load and moment. The corresponding maximum contact pressure (using the Hertzian point or line contact model) can also be calculated in any slice:

$$\begin{gathered} dQ = \frac{\pi}{2}.E_{eq}.\frac{CP.CB}{CD}.dy.\delta = E_{eq}.f_1.dy.\delta \qquad dM = dQ.y \\ P_{lc} = E_{eq}.\sqrt{\frac{dQ}{2.\pi.E_{eq}.R_{x\_eq}.dy}} = \frac{E_{eq}}{2}.\sqrt{\frac{CP.CB}{CD}}.\sqrt{\frac{\delta}{R_{x\_eq}}} \\ P_{pc} = E_{eq}.\frac{CP}{\sqrt{CD}}.\sqrt{\frac{\delta}{R_{x\_eq}}} \end{gathered} \tag{31}$$

knowing that $P_{pc} \approx P_{lc}$ at large k ratios, because:

$$\frac{P_{pc}}{P_{lc}} = 2.\sqrt{\frac{CP}{CB}} \approx 1 \tag{32}$$

As explained above, this linear model will be used next in truncated contact with or without misalignment for deriving, via some analytical integrations, appropriate analytical load and moment relationships.

Note that the suggestion of using the product (*r.y*) instead of *y* also applies to any profile (LOG profile multi radii, also called MRD, profile for example), the ratio *r* being then defined using the main crown radius often describing 60 % of the contact.

$$\text{Profile} = f(geometry,\ y) \qquad \delta = \delta_{\max} - f(geometry,\ r.y) \tag{33}$$

A LOG profile is a kind of optimum profile corresponding to a uniform pressure distribution along the roller – race contact length. It applies however to a specific load value and no misalignment.

An MRD profile is described using 4 radii and 3 lengths and offers more flexibility for controlling the contact pressure.

$$\begin{aligned}\text{Profile}_{Log} &= \frac{\left(\dfrac{1-\upsilon_1^2}{E_1} + \dfrac{1-\upsilon_2^2}{E_2}\right)}{\pi} . \frac{Q}{L} . \ln\left[\frac{1}{1-\left(\dfrac{2.y}{L}\right)^2}\right] \\ &= f_{Log}\left(y, Q, L\right)\end{aligned} \tag{34}$$

$$\text{Profile}_{MRD} = f_{MRD}(y, R_1, L_1, R_2, L_2, R_3, L_3, R_4)$$

An Example of LOG and MRD profile has been given in [10], knowing that it is always possible to define a MRD profile replacing a LOG one as shown in the next Figure:

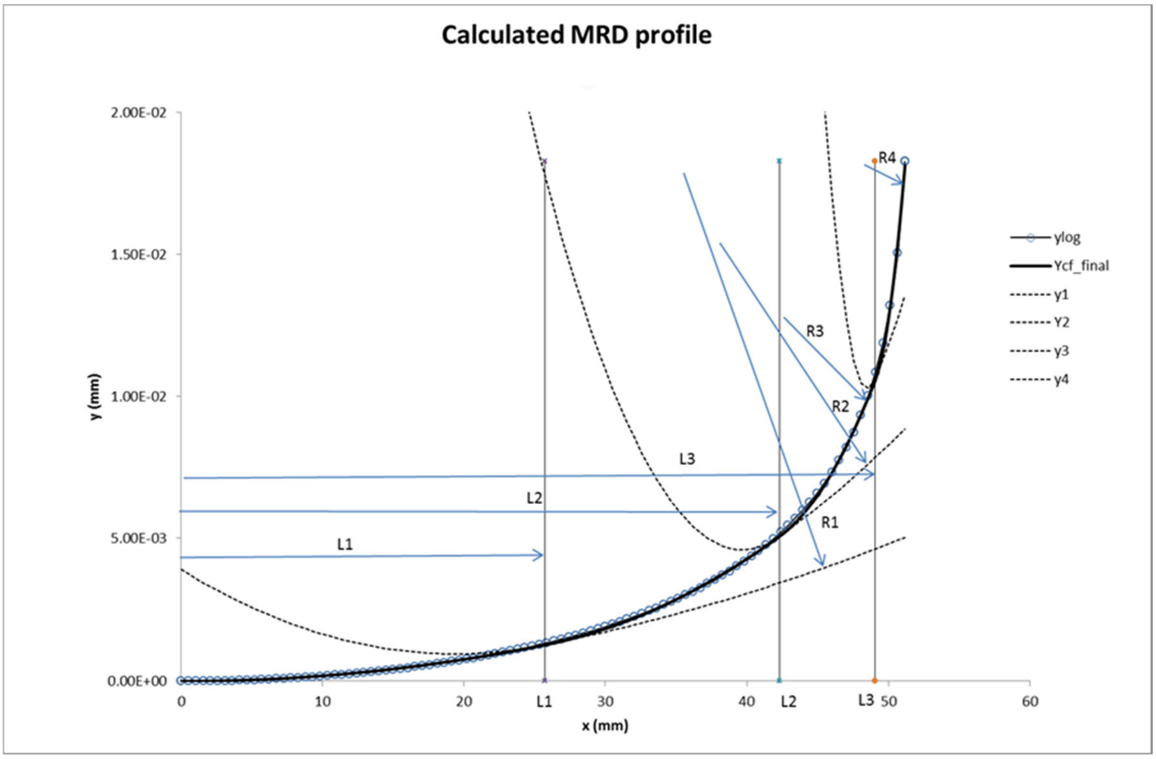

Fig. 6: Example of MRD profile duplicating a LOG profile, as shown in [10]. y corresponds to Profile and x corresponds to y in this paper.

Detailed analytical relationships describing an MRD profile are not shared in this report to avoid any potential confidentiality issues.

In the above Figure (extracted from [10], *y* and *x* represent the profile and abscissa respectively. They should be replaced by *Profile* and *y* respectively in this paper.

2.5. Initial analytical load in truncated point-contact including or not misalignment.

This exercise was initially conducted by Houpert in [12] using the geometrical interference and then in [10] using the elastic deformation via the use of the product (*r.y*).

When using the relative roller – inner race misalignment (roller tilt considered positive when rotating counterclockwise), the final deformation at the roller – inner race contact reads:

$$\delta = \Delta_0 - \theta.(r.y) - \frac{(r.y)^2}{2.R_{y\_eq}} \tag{35}$$

As a reminder, y is the axis along the roller length going from left to right (or along the large contact ellipse) while x and z are the axis used along the small contact ellipse and equivalent profile height respectively, z going from the bottom to top when drawing the roller on the inner race for example. A positive roller rotation around the x axis corresponds to a counterclockwise rotation, the y axis rotating towards the z axis.

Contact ellipse truncation can occur when the geometrical interference Δ_0 at the race center is too large for example.

The contact left and right boundaries are then defined by:

$$y_{1end} = \max\left[\frac{R_{y\_eq}\cdot\left(-\theta - \sqrt{\theta^2 + 2.\frac{\Delta_0}{R_{y\_eq}}}\right)}{r}; -\frac{L}{2}\right] \quad y_{2end} = \min\left[\frac{R_{y\_eq}\cdot\left(-\theta + \sqrt{\theta^2 + 2.\frac{\Delta_0}{R_{y\_eq}}}\right)}{r}; \frac{L}{2}\right] \tag{36}$$

When using an MRD profile and its four radii in four zones, the left and right contact boundaries as well as the corresponding load obtained by integration of the load in four zones can be calculated analytically too (the boundaries are the root of a polynomial degree 2 equation.

Alternatively, a summation of the load dQ in 101 or 1001 slices for example can be recommended because of its simplicity and applicability to any profile.

The following Figure, extracted from [10] shows as example the contact pressure calculated in an SRB using zero misalignment and two profiles: a single crown radius (defined by the osculation ratio) or the same one but with a drop radius at the edge of the roller.

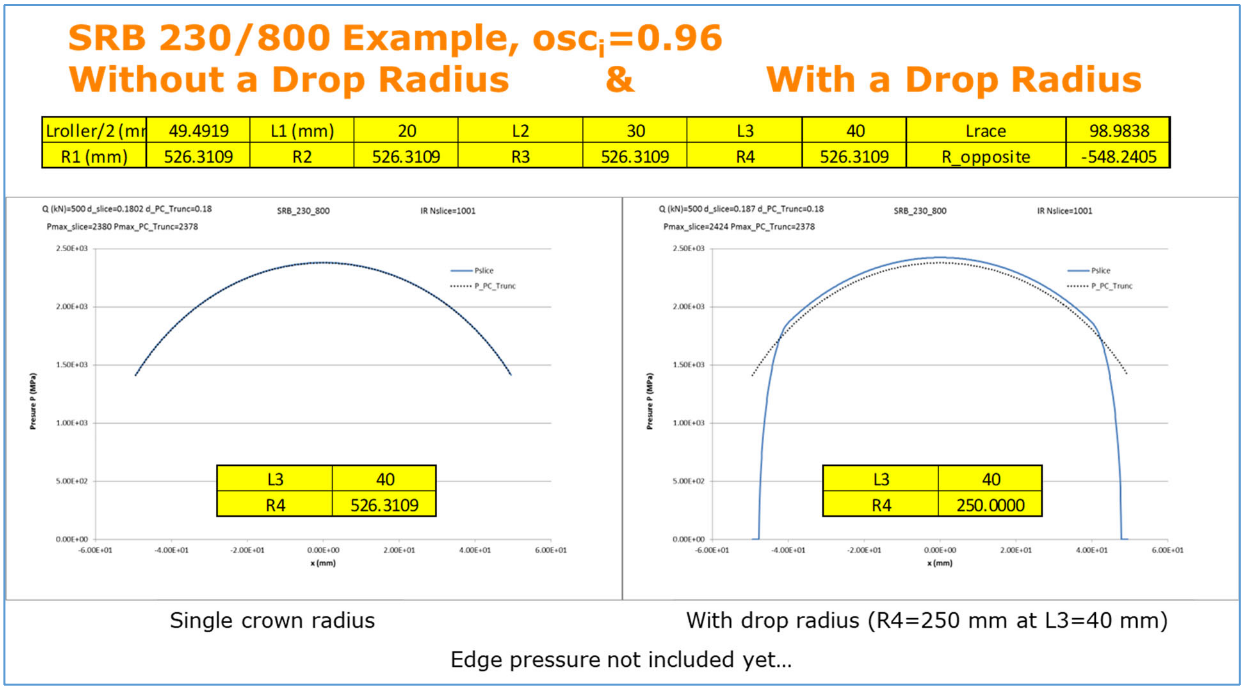

SRB 230/800 Example, osc$_i$=0.96

Without a Drop Radius & With a Drop Radius

Lroller/2 (mr	49.4919	L1 (mm)	20	L2	30	L3	40	Lrace	98.9838
R1 (mm)	526.3109	R2	526.3109	R3	526.3109	R4	526.3109	R_opposite	-548.2405

L3	40
R4	526.3109

L3	40
R4	250.0000

Single crown radius

With drop radius (R4=250 mm at L3=40 mm)

Edge pressure not included yet…

Fig. 7: Example of pressure distribution calculated in an SRB, extracted from [10].

When using a single crown profile, the load and moment (applied on the roller around the inner race center I) in each slice can be integrated analytically for obtaining:

$$Q_{pc\_trunc} = E_{eq}.f_1 \cdot \left[\Delta_0\left(y_{2end} - y_{1end}\right) - \frac{r^2}{6\cdot R_{y\_eq}}\left(y_{2end}^3 - y_{1end}^3\right) - \frac{\theta.r}{2}\left(y_{2end}^2 - y_{1end}^2\right)\right]$$

$$M_{pc\_trunc/I} = E_{eq}.f_1 \cdot \left[\frac{\Delta_0}{2}\left(y_{2end}^2 - y_{1end}^2\right) - \frac{r^2}{8\cdot R_{y\_eq}}\left(y_{2end}^4 - y_{1end}^4\right) - \frac{\theta.r}{3}\left(y_{2end}^3 - y_{1end}^3\right)\right] \tag{37}$$

where θ is the relative roller – inner race tilting angle. The latter should be considered as the initial analytical load and moment relationships because the coupling between slices, as well as pressure spikes, are not included.

At this stage of the study, it is interesting to demonstrate that, when studying very truncated point contact, the corresponding maximum contact pressure is close to the ideal line contact pressure.

When no misalignment is considered, the truncated point contact load can also be written:

$$
\begin{aligned}
Q_{pc\_trunc} &= E_{eq}.f_1 \cdot \left[\Delta_0 L - \frac{r^2.L^3}{24 \cdot R_{y\_eq}}\right] = E_{eq}.f_1 \cdot \Delta_0 L.\left[1 - \frac{r^2.L^2}{24 \cdot R_{y\_eq}.\Delta_0}\right] \\
&= E_{eq}.f_1.L.\cdot \Delta_0.\left[1 - \frac{L^2}{12 \cdot a_{NT}^2}\right] \approx E_{eq}.f_1.L.\cdot \Delta_0
\end{aligned}
\tag{38}
$$

Note that we lost the exponent 1.5 applied on the deformation because of the severe truncation considered.

The corresponding truncated maximum point and line contact pressure values or analytical relationships become then very similar, thanks to the approximation $2.\sqrt{\frac{CP}{CB}} \approx 1$ used in the next equations. This demonstrates the possibility of describing line contact results using a truncated point contact model:

$$
\begin{aligned}
&Q = E_{eq}.f_1.L.\delta_{\max} \\
&P_{pc} = E_{eq}.\frac{CP}{\sqrt{CD}}.\sqrt{\frac{\delta_{\max}}{R_{x\_eq}}} = E_{eq}.\frac{CP}{\sqrt{CD}}.\sqrt{\frac{Q}{R_{x\_eq}.E_{eq}.f_1.L}} \\
&\quad = 2.\sqrt{\frac{CP}{CB}}.E_{eq}.\sqrt{\frac{Q}{2.\pi.E_{eq}.R_{x\_eq}.L}} \approx E_{eq}.\sqrt{\frac{Q}{2.\pi.E_{eq}.R_{x\_eq}.L}} \quad because \quad 2.\sqrt{\frac{CP}{CB}} \approx 1 \\
&P_{lc} = E_{eq}.\sqrt{\frac{Q}{2.\pi.E_{eq}.R_{x\_eq}.L}}
\end{aligned}
\tag{39}
$$

In the latter first approach, the moment has been calculated relative to the race center point *I*, an approach recommended for TRB with the roller seated in the race-rib (or flange) corner.

When studying SRB, a second approach can also be used as suggested in [10] since roller tilt induces a shift of the contact ellipse (due to roller rocking). Exact calculations of the roller axial shift and contact ellipse shift can be conducted by following the centers of curvature of the roller and races as done by Houpert et al. in [11]. But a simplified approach has been suggested in [10] for calculating this shift without including the ratio *r* at this time. Including now this ratio *r* (for keeping a certain consistency with eq. (35)), the abscissa corresponding to the maximum elastic deformation is equal to the abscissa of the shifted contact ellipse center. Misalignment can then be included for defining the *shift* and maximum deformation, as well the left and right contact boundaries (function of the shift, hence misalignment). The subsequent SRB load and moment can then be calculated with zero misalignment. For example, at the roller – IR contact:

$$
\begin{aligned}
&Shift \approx -\frac{\theta}{r}.R_{y\_eq} \qquad \delta_{\max} \approx \Delta_{\max} \approx \Delta_0 + \theta^2.\frac{R_{y\_eq}}{2} \\
&\delta \approx \delta_{\max} - \frac{r^2.(y - shift)^2}{2.R_{y\_eq}} \\
&Y_{Left} = Max\left\{\frac{-\frac{L}{2} - shift}{a_{NT}}, -1\right\} \qquad Y_{Right} = Min\left\{\frac{\frac{L}{2} - shift}{a_{NT}}, 1\right\}
\end{aligned}
\tag{40}
$$

In the latter, the index NT means non-truncated and is used for calculating the non-truncated ellipse dimension *a* defined as a function of the maximum deformation, see eq. (38).

Y is a dimensionless abscissa equal to y/a_{NT}.

The SRB roller load and moment (calculated around the contact ellipse center *CI* or race center *I*) corresponding to this second approach are then:

$$\begin{aligned}
Q_{pc\_trunc} &= \frac{3}{4}.Q_{NT}\cdot\left(Y_{Right}-Y_{Left}-\frac{Y_{Right}^{3}-Y_{Left}^{3}}{3}\right)\\
M_{pc\_trunc/CI} &= \frac{3}{16}.Q_{NT}.a_{NT}.\left\{2.\left(Y_{Right}^{2}-Y_{Left}^{2}\right)-\left(Y_{Right}^{4}-Y_{Left}^{4}\right)\right\} \qquad (41)\\
M_{pc\_trunc/I} &= M_{pc\_trunc/CI} \pm Q_{pc\_trunc}.y_{shift} \quad (+\ on\ IR)
\end{aligned}$$

Note that the latter relationships are incomplete (the correction factor *Coef*, described later, is missing) although benchmarked relatively successfully in [10]. The accuracy was about 10% and considered satisfactory at this time when comparing our results against the numerical TRB and SRB results calculated using Hoeprich's tool CST as reference. The next Figure shows the calculated load in a TRB and SRB example:

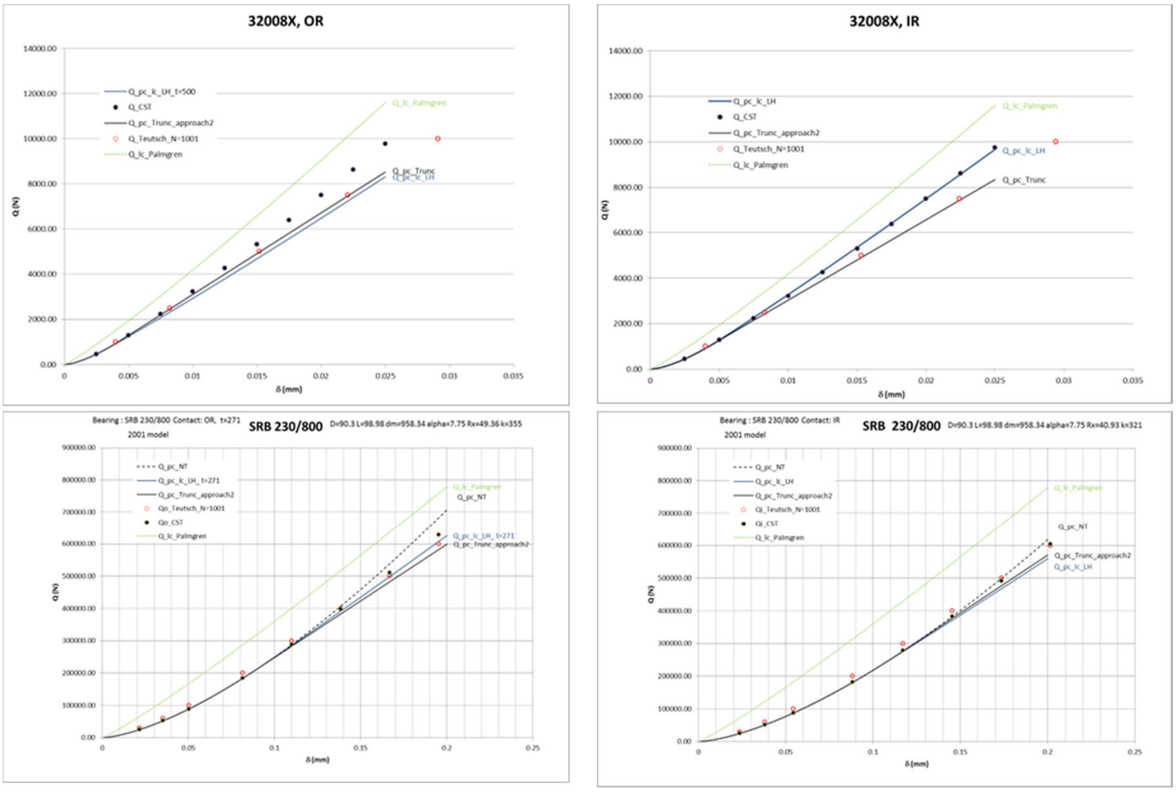

Fig. 8: Example (derived from [10] of load calculated using a TRB and SRB example.

The Palmgren line contact load is also shown (as too large) in the latter figure, as well as the load calculated using the initial point to line contact transition model with an appropriate outer race - housing section thickness *t*.

Also shown in the latter Figure is the calculated numerical load *Q_Teutsch* (including pressure spikes) described later.

2.5.2. Introduction of the correction factor called *Coef*:

What is missing in all latter relationships is the introduction of a correction factor called *Coef*, introduced in [4] and accounting for additional truncation effects on the load and moment, effects due to the coupling between slices and existence of pressure spikes at the edges of the contact.

Ref. [4] is mainly describing the load calculated in truncated point contact using a single crown radius and no misalignment.

The index *NT* is used for describing what the contact ellipse dimension *a* and the load *Q* would be when calculating them as a function of the deformation δ_{max} (and not limiting the contact boundaries because of the finite roller or race length).

$$Q_{NT}=\frac{E_{eq}.\sqrt{R_{x\_eq}}}{CD^{1.5}}.\delta_{\max}^{1.5}=f_3.E_{eq}.\sqrt{R_x}.\delta_{\max}^{1.5}=K_{PC}.\delta_{\max}^{1.5}$$

$$a_{NT}=CA.R_{x\_eq}.\left(\frac{Q_{NT}}{E_{eq}.R_{x\_eq}^2}\right)^{\frac{1}{3}}=\frac{CA}{\sqrt{CD}}.\sqrt{R_{x\_eq}.\delta_{\max}}=\frac{f_2}{2}.\sqrt{R_{x\_eq}.\delta_{\max}} \tag{42}$$

$$b_{NT}=CB.R_{x\_eq}.\left(\frac{Q_{NT}}{E_{eq}.R_{x\_eq}^2}\right)^{\frac{1}{3}}=\frac{CB}{\sqrt{CD}}.\sqrt{R_{x\_eq}.\delta_{\max}}$$

Also, a dimensionless deformation D and truncation level T have been introduced in [4]:

$$D=\frac{\delta_0.R_{x\_eq}}{L^2}=\frac{\Delta_0.R_{x\_eq}}{L^2}\qquad T=\frac{2.a_{NT}}{L}=f_2.\sqrt{D} \tag{43}$$

In which T is limited to 1 when no truncation occurs.

δ_o is the deformation at abscissa y=0, hence equal to δ_{max} when no misalignment occurs.

The previously described non-truncated or truncated point contact load (without using the factor *Coef*) then reads:

$$\frac{Q_{pc\_trunc}}{\frac{E_{eq}.L^3}{R_{x\_eq}}}=f_1.D.Min(1,T).\left[1-\frac{1}{3}.\left(\frac{Min(1,T)}{T}\right)^2\right] \tag{44}$$

The initial problem discovered in [4] is illustrated by the following Figure in which a scan on D and k has been conducted.

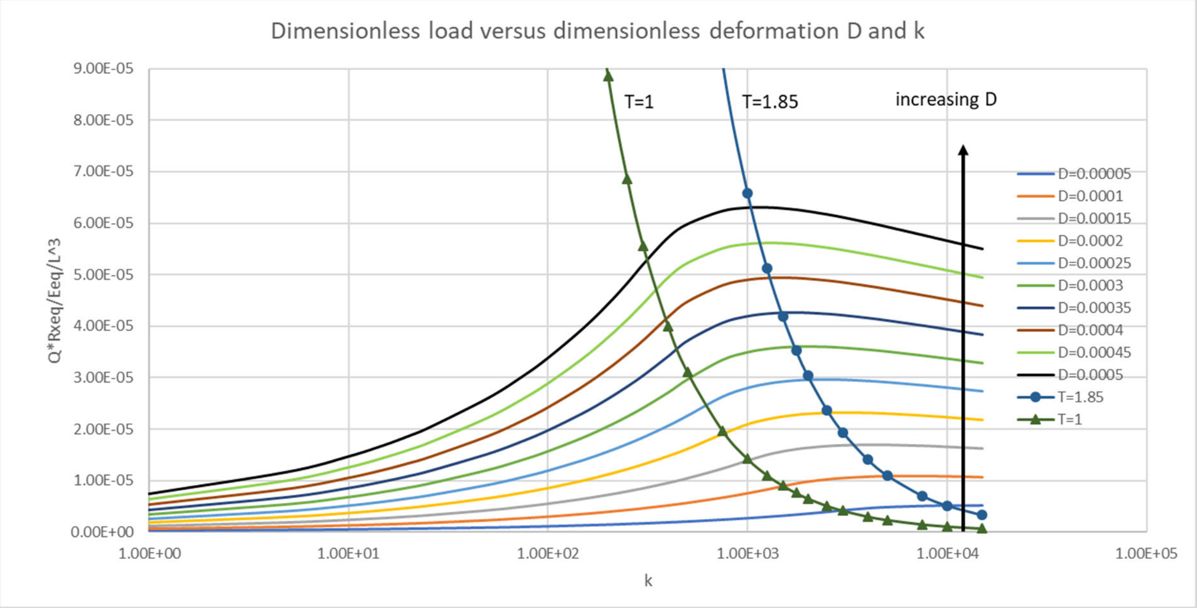

Fig. 9: Initial results obtained when scanning D and k (without using the correction factor Coef).

As expected, for a given deformation D, the load and contact stiffness are increasing when increasing the k ratio (at small to moderate k ratio), but an unacceptable drop of load is observed at large k ratio when the truncation level exceeds 1.85

For solving this problem, CST results have been used as reference for studying a cylinder-on-cylinder reference case (R_{x_eq} = 10 mm, L =30 mm) subjected to a constant deformation (δ_o =0.045 mm, D=5*10^{-4}) with a k ratio (hence equivalent crown radius) varying from 1 to 13577. When k exceeds 313, the contact gets truncated.

When conducting this exercise, one can confirm the drop of load above a certain truncation level and introduce the ratio $Coef = Q_{CST}/Q_{pc\_trunc}$ to curve fit versus the truncation level T for matching the new or corrected analytical truncated point contact load (including the correction factor *Coef*) to the CST load.

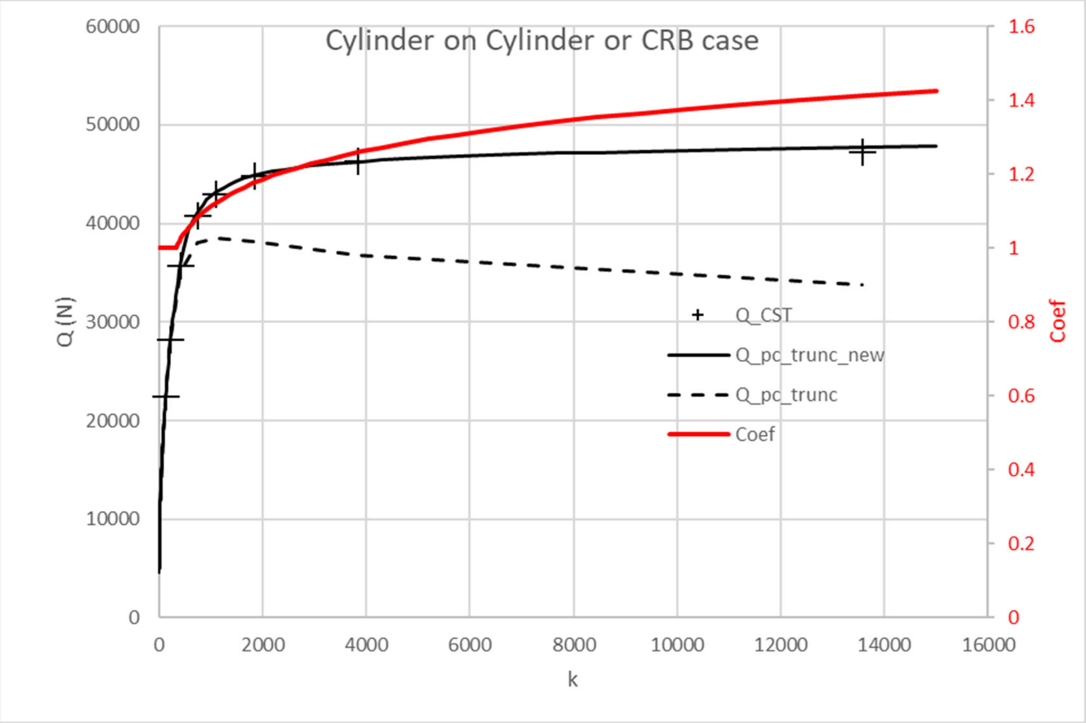

Fig. 10: New results obtained using Coef and scanning on k only, with D fixed to 0.0005

For information, the calculated Palmgren load (which does not account for the *k* ratio) is equal to 51405 N in this case, hence about 7.7% larger than the numerical CST load at the largest *k* value.

$$Coef = Max(1, T^{0.18})$$

$$\frac{Q_{pc\_trunc\_new}}{\dfrac{E_{eq}.L^3}{R_{x\_eq}}} = Coef.f_1.D.Min(1,T).\left[1 - \frac{1}{3}.\left(\frac{Min(1,T)}{T}\right)^2\right] \qquad (45)$$

When using *Coef* and scanning on *k* and *D,* one now obtains the following two Figures:

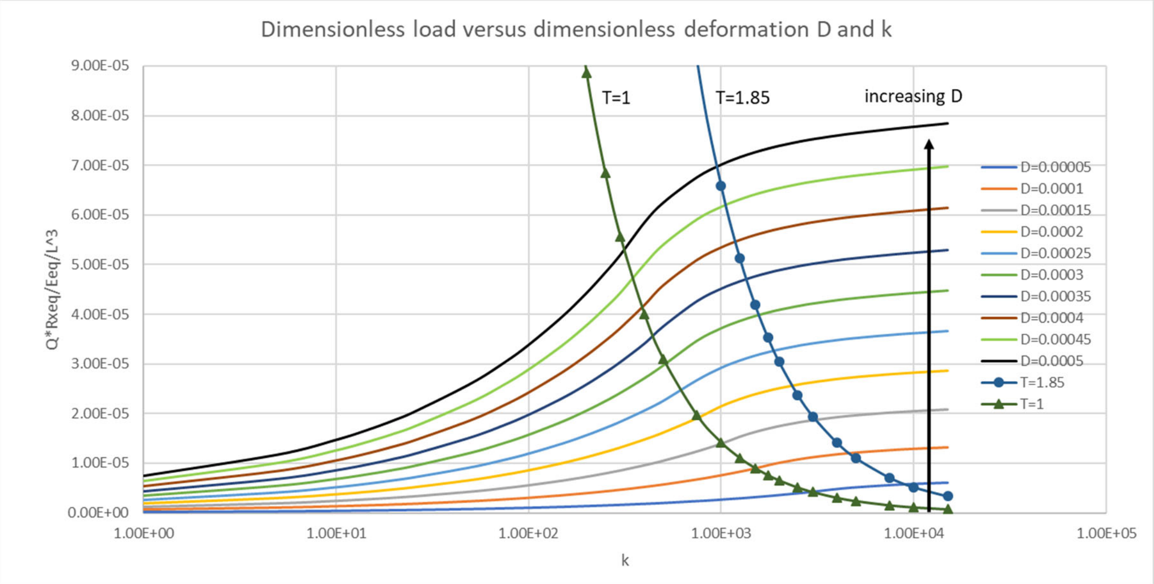

Fig. 11 : When using Coef and scanning on k and D, one obtains the following two Figures:

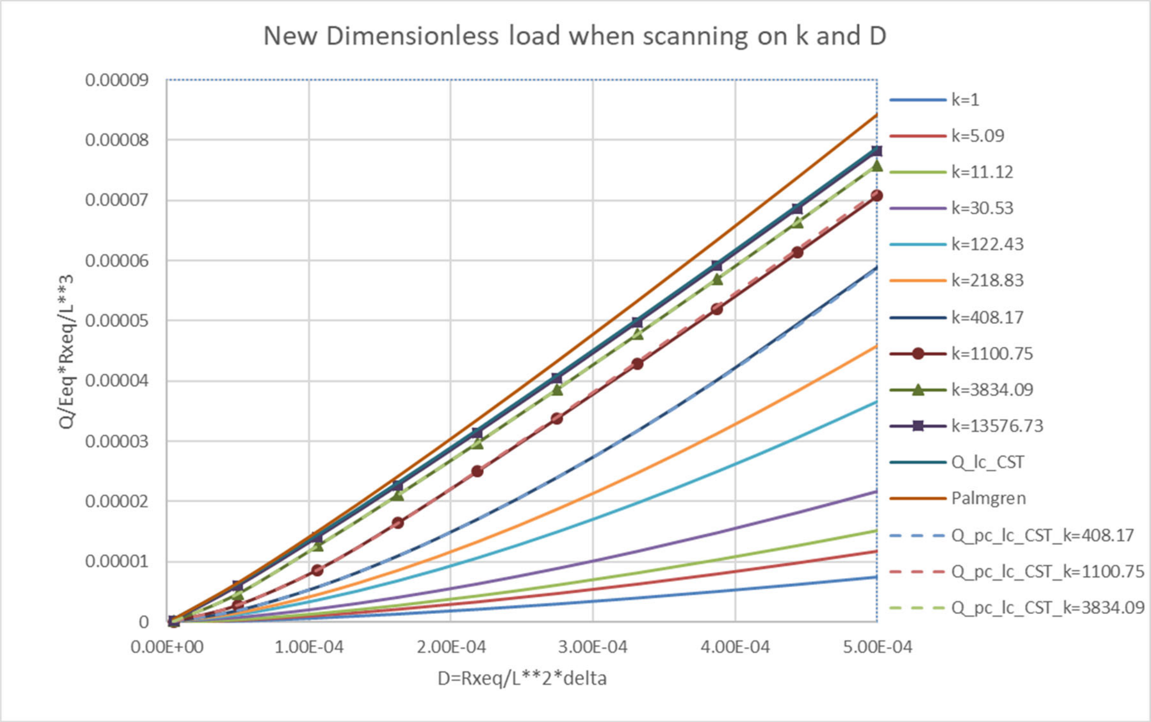

Fig. 12: The new dimensionless load (using Coef) obtained when scanning on k and D

Also shown in the latter Figure are:

- the Palmgren load (upper curve)
- a new suggested line contact load (Q_*lc_CST* described later)
- the loads *Q_pc_lc_CST*, dotted line curves, calculated with eq. (23) and accounting for a smooth transition from point to line contact load.

The latter perfectly matches the new truncated point contact load. As demonstrated above, the Palmgren load is again too large.
Also, using now the new suggested truncated point contact load (including the factor *Coef*) and our last TRB and SRB example, the match with CST results becomes excellent.

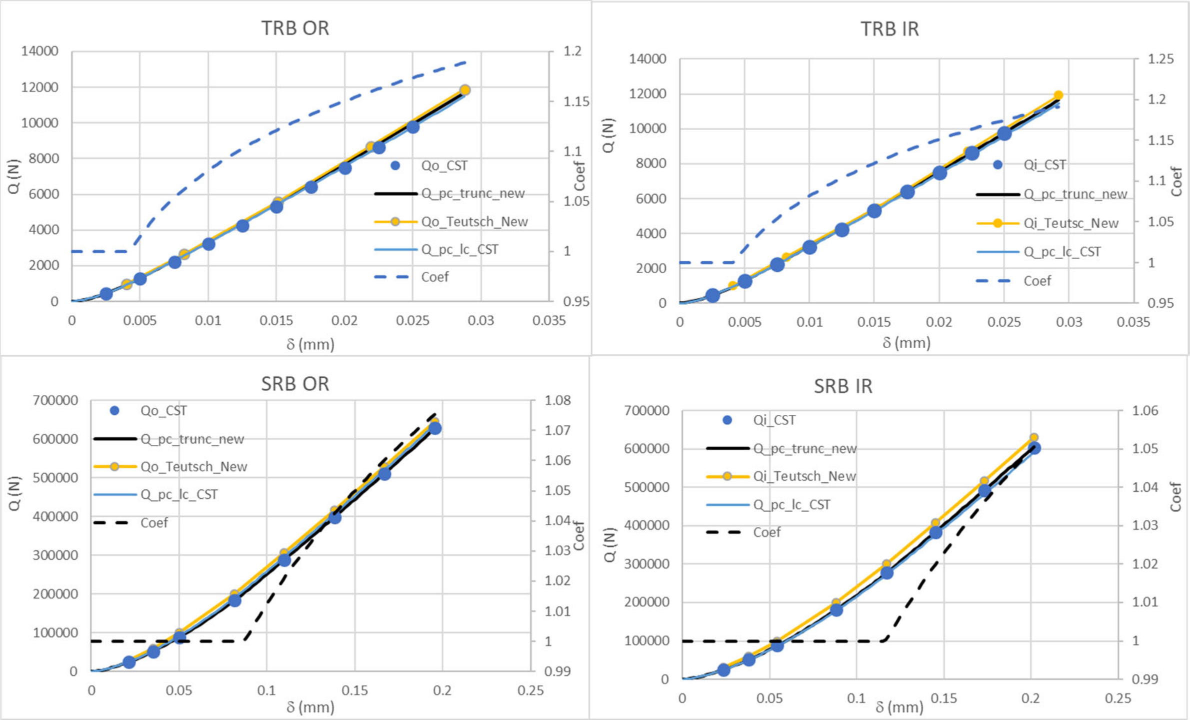

Fig. 13: Results obtained with the newly suggested model (with the correction factor Coef)

Note that the factor *Coef* also needs to be included when calculating the load *dQ*, pressure *P* and half width *b* in each slice (for retrieving the final load) leading finally to:

$$dQ = Coef.f_1.E_{eq}.\delta.dy = Coef.f_1.E_{eq}.\left(\Delta_0 - \theta.r.y - \frac{(r.y)^2}{2.R_{y\_eq}}\right).dy \quad or$$

$$dQ = Coef.f_1.E_{eq}.\delta.dy = Coef.f_1.E_{eq}.\left(\Delta_0 - \theta.r.y - \text{Profile}(Geometry\ \&\ r.y)\right).dy \tag{46}$$

When using single crown profiles and ignoring pressure spikes, the pressure can finally be approximated at any (*x,y*) point using:

$$P(x,y) = \sqrt{Coef}.\frac{CP}{\sqrt{CD}}.E_{eq}.\sqrt{\frac{\delta_{\max}}{R_{x\_eq}}}.\sqrt{1-\left(\frac{x}{b}\right)^2-\left(\frac{y}{a}\right)^2}^{\,2}$$

$$with \quad b = \sqrt{Coef}.\frac{CB}{\sqrt{CD}}.\sqrt{R_{x\_eq}.\delta_{\max}} \quad and \quad a = \frac{CA}{\sqrt{CD}}.\sqrt{R_{x\_eq}.\delta_{\max}}$$

(47)

When truncation occurs, the *y* values are of course limited to ± *L*/2.

A double integration of *P(x,y).dx.dy* leads to the appropriate load *Q*.

Once the load *dQ* is known, the maximum pressure in any slice can be calculated using a point contact (recommended) or line contact relationship and the same correction factor *Coef*:

$$P_{pc} = \frac{\sqrt{Coef}.CP}{\sqrt{CD}}.E_{eq}.\sqrt{\frac{\delta}{R_{x\_eq}}} = \sqrt{Coef}.\frac{E_{eq}.L}{R_{x\_eq}}.\frac{CP}{\sqrt{CD}}.\sqrt{\frac{\delta.R_{x\_eq}}{L^2}} \quad or$$

$$P_{lc} = E_{eq}.\sqrt{\frac{dQ}{2.\pi.E_{eq}.R_{x\_eq}.dy}} = \sqrt{Coef}.\frac{E_{eq}.L}{R_{x\_eq}}.\sqrt{\frac{CP.CB}{4.CD}}.\sqrt{\frac{\delta.R_{x\_eq}}{L^2}} \tag{48}$$

Since the previously described dimensionless load is a function of *D* and *T* and since *T* is also a function of *D* and f_2 (hence *k*), it is also possible to define another dimensionless load only function of the truncation level *T* (when no misalignment occurs):

$$Q_{Dimensionless} = \frac{f_2^2}{f_1}.\frac{Q_{pc\_trunc\_new}}{\frac{E_{eq}.L^3}{R_{x\_eq}}} = Max(1,T^{0.18}).T^2.Min(1,T).\left[1-\frac{1}{3}.\left(\frac{Min(1,T)}{T}\right)^2\right]$$

$$= T^3.\left[\frac{2}{3}\right] \qquad if \quad T \le 1$$

$$= T^{2.18}.\left[1-\frac{1}{3}.\left(\frac{1}{T}\right)^2\right] \quad if \quad T > 1 \tag{49}$$

$$with$$

$$\text{T}=f_2.\sqrt{\frac{\delta_0.R_{x\_eq}}{L^2}} \qquad \frac{f_2^2}{f_1} = \frac{16}{3}.CA^3$$

The latter relationship is simple to use and is certainly the most compact one for calculating the contact load in the non-truncated and truncated case, dimensionless load described by a single master curve, see next Figure:

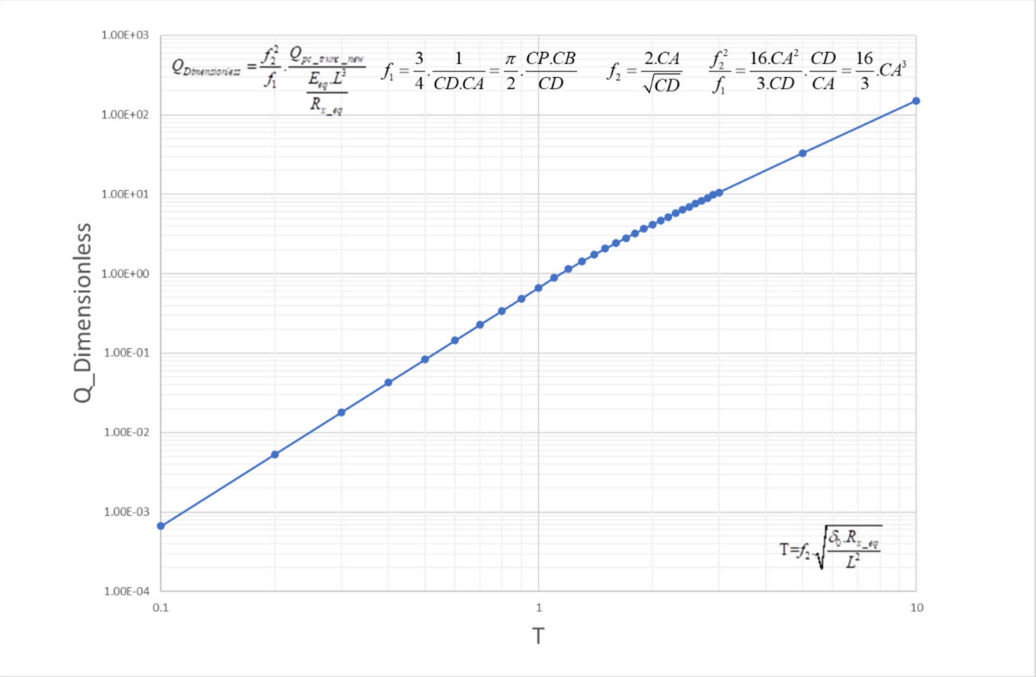

Fig. 14: Dimensionless load described by a single master curve (without misalignment)

One can recognize the exponent 3 applied on T, hence 1.5 applied on the deformation, when calculating the load in non-truncated point contact ($T \leq 1$). At large T values, this exponent tends towards 2.18, hence 1.09 applied on the deformation, a typical value for line contact.

f_1 and f_2 can be calculated as a function of k, via the use of eq. (9) and table 2 or can be calculated using the following simplified curve-fitting conducted in the frame of this project:

$$f_2 \approx 2 * \exp\left\{-2.2330293E-03 * [\ln(k)]^2 + 5.5202690E-01 * [\ln(k)]\right\} \tag{50}$$

$$\frac{f_1}{f_2^2} \approx 0.125 * \exp\left\{1.3389969E-02 * [\ln(k)]^2 - 1.3524301 * [\ln(k)]\right\} \tag{51}$$

In summary, when studying single crown contact subjected to a deformation δ_0 and no misalignment, the following analytical load (accounting for non-truncated and truncated contact) can be suggested:

When no misalignment occurs :

$$\text{T}=f_2.\sqrt{D} \quad and \quad D = \frac{\delta_0.R_{x\_eq}}{L^2} \quad \text{(Dimensionless truncation and deformation)}$$

$$f_2 \approx 2 * \exp\left\{-2.2330293 * 10^{-3} * [\ln(k)]^2 + 0.55202690 * [\ln(k)]\right\}$$

$$\frac{f_1}{f_2^2} \approx 0.125 * \exp\left\{1.3389969 * 10^{-2} * [\ln(k)]^2 - 1.3524301 * [\ln(k)]\right\}$$

$$\begin{aligned} Q_{pc\_trunc\_new} &= \frac{f_1}{f_2^2}.\frac{E_{eq}.L^3}{R_{x\_eq}}.Max(1,T^{0.18}).T^2.Min(1,T).\left[1-\frac{1}{3}.\left(\frac{Min(1,T)}{T}\right)^2\right] \\ &= \frac{f_1}{f_2^2}.\frac{E_{eq}.L^3}{R_{x\_eq}}.T^3.\left[\frac{2}{3}\right] \qquad if \quad T \leq 1 \quad (non\ truncated\ contact) \\ &= \frac{f_1}{f_2^2}.\frac{E_{eq}.L^3}{R_{x\_eq}}.T^{2.18}.\left[1-\frac{1}{3}.\left(\frac{1}{T}\right)^2\right] \qquad if \quad T > 1 \quad (truncated\ contact) \end{aligned} \tag{52}$$

3. Houpert's improved Teutsch model

As explained above, the load and pressure on any slice can be calculated as a function of the central deformation δ and relative roller – race misalignment θ, using any profile.

The calculation of pressure spikes at the edge of the contact is however missing. Pressure spikes can be calculated using the complex numerical models of Hoeprich, Cretu, Reusner and Guo cited earlier.

Using Houpert's line contact model [3] (including the outer race – housing thickness *t*), Teutsch and Sauer [10] developed an interesting simplified approach applicable to line contact only.

Their approach has been improved by Houpert in [10] and [4] for being also applicable to point contact (non-truncated or truncated) and easier to use, thanks to a newly suggested dimensionless approach.

The modified Teutsch model suggested by Houpert is certainly not as accurate as the more rigorous model developed by Hoeprich (CST tool), Cretu, Reusner or Guo, (see comparisons conducted in chapter "5. NEW MODELS") but can be recommended because of its simplicity to use. It is certainly sufficient for warning the user about the risk of pressure spikes at the edge of the truncated contact.

The following set of relationships summarizes the *modified* (sometimes also listed as *new* in the legend) Teutsch model, see also [10] and [4].

$$
\begin{gathered}
\text{Geometrical interference: } \Delta_i = \delta_0 - \text{Profile}(y_i) - \theta . y_i \\
\\
\textit{Use in each slice Houpert's load - deformation } \text{model:} \\
\Delta_i = s.dQ_i \quad \textit{with} \quad s = \frac{2}{Coef.\pi.E_{eq}} . \frac{CD}{CP.CB.dy} = \frac{1}{Coef.E_{eq} f_1.dy} = f(k, E_{eq}, dy) \\
\textit{Use a } \text{dimensionless } \textit{approach}: \; w_{i,j} = \left(\frac{1}{|i-j|} \right) \quad \textit{and} \quad w_{i,i} = 4 \; (\textit{when } i = j) \\
\textit{Define } \left[S_{i,j} \right] = \frac{N_{slice}}{\sum\limits_{i,j} w_{i,j}} . \left[w_{i,j} \right] \; (\textit{only once as a function of } N_{slice}) \\
\textit{Define } \left[S_{i,j} \right]^{-1} \quad (\textit{only once as a function of } N_{slice}) \textit{ to read as input} \\
\\
\textit{Calculate load } dQ_i \; \& \; Q \textit{ as}: \; \{dQ_i\} = \frac{1}{s} . \left[S^{-1}_{i,j} \right] \{\Delta_j\} \qquad Q = \sum_{i=1,N_{slice}} dQ_i \\
\\
\textit{Multiply } dQ_1 \; \& \; dQ_{N_{slice}} \textit{ by } 1.25 \textit{ for matching CST results} \\
\\
(\textit{solve for } \delta_0 \textit{ if load } Q \textit{ is imposed}) \\
\textit{Calculate the } \text{Pressure } P(i) = E_{eq} . \sqrt{\frac{dQ(i)}{2.\pi.R_{x\_eq}.E_{eq}.dy}} \qquad (\textit{LC relationship})
\end{gathered}
\tag{53}
$$

Note that use is made of the geometrical interference *Δ*, not elastic deformation, and that the matrix $[S_{i,j}]$ and its inverse only need to be calculated once, being read as input later on.

Also, as a result of the slice coupling introduced via the matrix $[S_{i,j}]$ and its inverse, the final elastic contact length will always be shorter than the geometrical contact length when no truncation occurs.

The modified Teutsch approach can also be used for defining the optimum profile:

$$
\mathrm{dQ_i} = \frac{Q}{L}.dy \qquad \{\Delta_i\} = s.\left[S_{i,j} \right].\{\mathrm{dQ_i}\} \qquad \{\text{Profile}_i\} = \Delta_{\max} - \{\Delta_i\} \tag{54}
$$

Several examples of calculated pressure distribution have been given by Houpert in [4] see for example the next Figures:

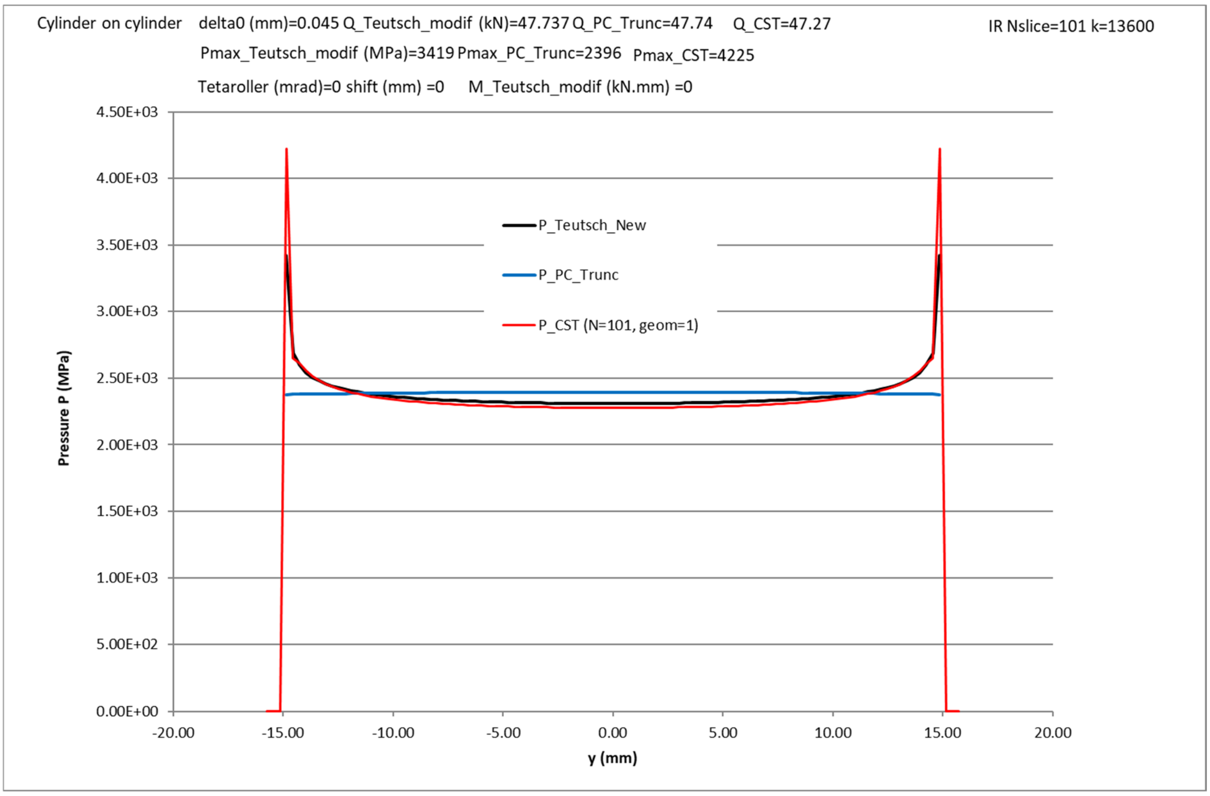

Fig. 15: Pressure distribution along the cylinder-on-cylinder contact, δ*= 0.045 mm and* $k = 13.6*10^3$

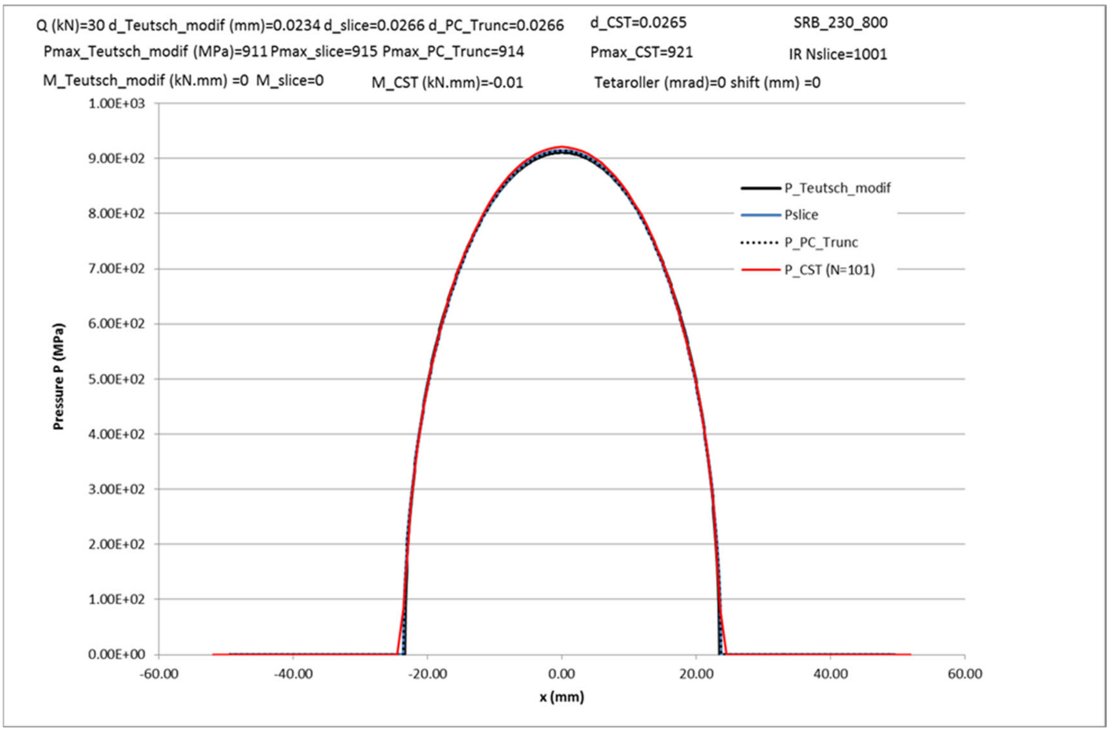

Fig. 16: SRB example at low load as presented in Ref. [10] (constant load imposed)

Note how the *Modified Teutsch* model (initially developed by Teutsch and Sauer for line contact only) is now also appropriate for describing point contact. It is however compulsory to keep all slices loaded (except the first and last one when describing a non-truncated point contact) because the matrix *[*$S_{i,j}$*]* and its inverse have been calibrated using the sum of all $w_{i,j}$ and all slices expected loaded. *dy* and *L* should therefore be defined in an appropriate manner ($L \approx 2*A_{Geom}$) for obtaining only the first and last slice unloaded when describing a non-truncated point contact. Note that when studying standard non-truncated point contact cases, it is recommended to use the previously described analytical non-truncated point contact model, certainly more accurate than the modified Teusch model.

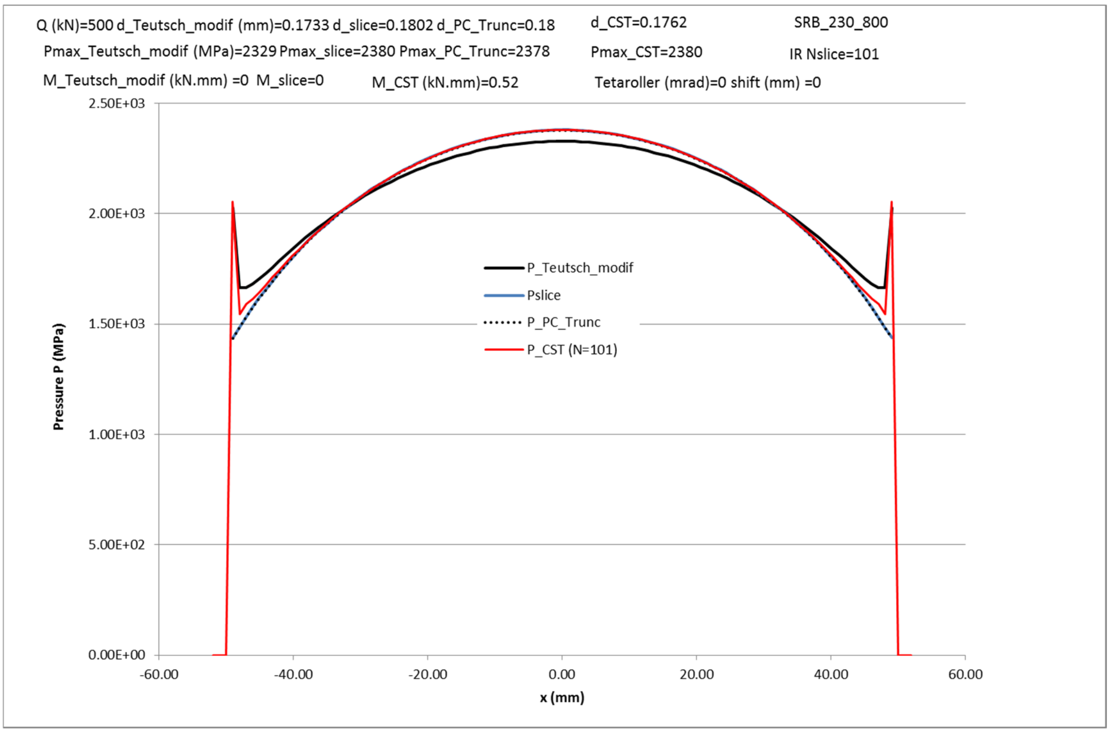

Fig. 17: SRB example at large load as presented in Ref. [10] (constant load imposed)

4. Additional developments

4.1. Q_{LC_CST} load

As explained in [4], it is interesting to use the suggested proposal at large *T* values for developing another line contact relationship.

Using the subscript CST (because the correction factor *Coef* ($Coef{=}f_2^{0.18}.D^{1.09}$) has been defined using the tool CST as reference), the truncated load Q_{LC_CST} reads:

$$\frac{Q_{LC\_CST}}{\dfrac{E_{eq}.L^3}{R_{x\_eq}}} = f_1.f_2^{0.18}.D^{1.09}.\left(1-\frac{1}{3.T^2}\right) = f_1.f_2^{0.18}.D^{1.09}.\left(1-\frac{1}{3.f_2^2.D}\right) \approx f_1.f_2^{0.18}D^{1.09} \tag{55}$$

where the bracket terms can be neglected at large *T* values; perhaps not when seeking for a high accuracy.

The product $f_1.f_2^{0.18}$ is plotted next against *k*. It can be fixed to 0.3 when *k* is large when using realistic large *k* ratio (k values larger than 15000 are seldom in the bearing industry because flat profiles are avoided). The small increase observed at very large *k* values is due to pressure spikes (introduced via the factor *Coef* using $f_2^{0.18}$). This increase can be considered when using $f_1.f_2^{0.18}$ instead of 0.3

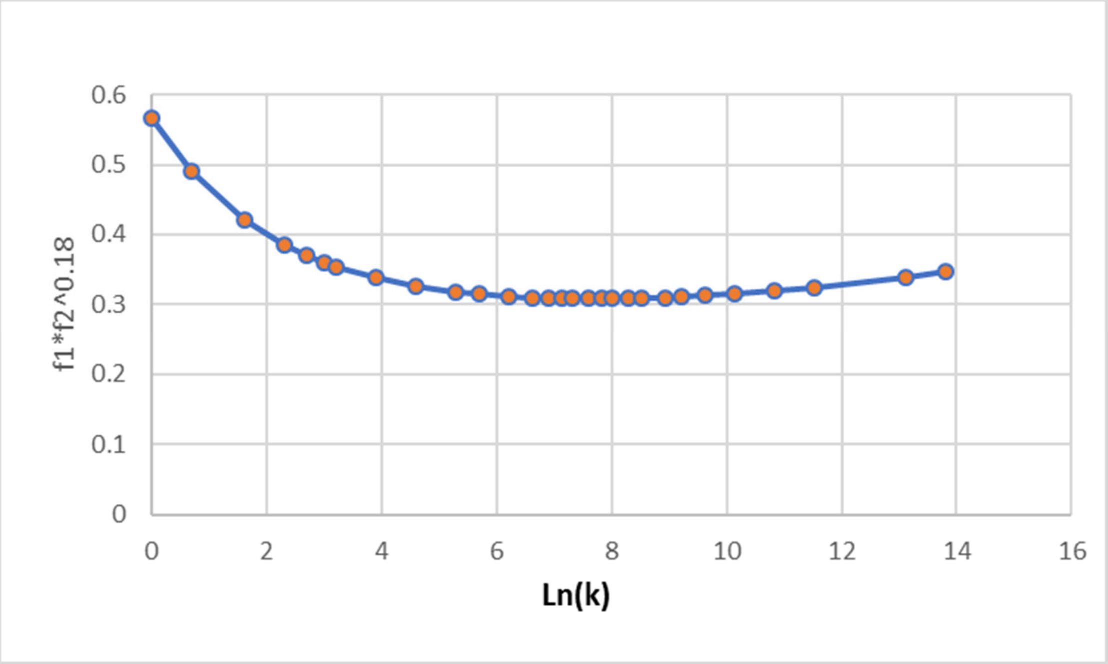

Fig. 18: Factor to use when defining Q_{LC_CST}

The simplified *CST* line contact load can therefore be defined as:

$$\frac{Q_{LC\_CST}}{\frac{E_{eq}.L^3}{R_{x\_eq}}} \approx 0.3 * D^{1.09} \tag{56}$$

or

$$Q_{lc\_CST} \approx 0.3 * \frac{E_{eq}.L^3}{R_{x\_eq}}.D^{1.09} = 0.3 * E_{eq}.L^{0.82}.R^{0.09}_{x\_eq}.\delta^{1.09} \tag{57}$$

The latter relationship accounts for a minor effect of R_{x_eq} on the load and is close to the well-accepted "empirical" relationship of Palmgren given in eq. (15):

$$Q_{Palmgren} \approx 0.347 * E_{eq}.L^{\frac{0.8}{0.9}}.\delta^{\frac{10}{9}} \tag{15}$$

When using our case of reference (δ=0.045 mm, L=30 mm and R_{x_eq}=10 mm) one obtains a CST line contact load of 46182 N versus 51404 N for the Palmgren load, hence a drop in load of more than 10 %.

At an unrealistic, very large *k* ratio (*k*=1.E7), using 0.3786 instead of 0.3 when defining the product $f_1 * f_2^{0.18}$, one obtains a load of 58281 N.

4.2. Comparing Hoeprich transition model and *T*=1 transition

The results described in this sub-chapter have been derived in the frame of this project (hence are not part of the previous models) and can be considered as interesting remarks only.

Hoeprich's point to line contact transition and final truncated load described by eq. (22) and (23) can also be written using the following general approach:

$$Q_{lc} = x_1.E_{eq}.L^{x_2}.R^{x_3}_{x\_eq}.\delta^{\,n} = K_{lc}.\delta^n \quad with \quad K_{lc} = x_1.E_{eq}.L^{x_2}.R^{x_3}_{x\_eq} \tag{58}$$

$$Q_{pc} = f_3.\frac{E_{eq}.L^3.}{R_{x\_eq}}.D^{1.5} = f_3.E_{eq}.\sqrt{R_{x\_eq}}.\delta^{1.5} = K_{pc}.\delta^{1.5} \quad with \quad K_{pc} = f_3.E_{eq}.\sqrt{R_{x\_eq}} \tag{59}$$

The local slope and deformation of transition then reads:

$$\frac{dQ_{lc}}{d\delta} = n.K_{lc}.\delta^{n-1} \qquad \frac{dQ_{pc}}{d\delta} = 1.5*K_{pc}.\delta^{0.5}$$

$$\delta_{Trans} = \left[\frac{n.K_{lc}}{1.5*K_{pc}}\right]^{\frac{1}{1.5-n}} \tag{60}$$

The latter can be used for calculating the dimensionless truncation level at Hoeprich's transition:

$$T_{Trans} = f_2.\sqrt{\frac{R_{x\_eq}.\delta_T}{L^2}};\ after\ \ some\ \ developments:$$

$$T_{Trans} = f_2.\left[\frac{n.x_1}{1.5*f_3}\right]^{\frac{0.5}{1.5-n}}.L^{\frac{0.5*x_2-1.5+n}{1.5-n}}.R_{x\_eq}^{\frac{0.5*(x_3-05)}{1.5-n}+0.5} \tag{61}$$

The interesting idea tested next is the analytical derivation of the exponent x_2 and x_3 for obtaining T_{Trans} independent of L and R_{x_eq}, a reasonable assumption. When imposing the exponents on L and R_{x_eq} to be nil, one obtains:

$$\begin{aligned} x_2 &= 2.(1.5-n)\ =\ 0.82\quad if\quad n=1.09\ \ (Houpert\ \ proposal)\ \ or \\ &=\ 0.778\ if\ \ n=\frac{10}{9}\quad (Palmgren) \\ x_3 &= n-1\ =\ 0.09\ \ if\ \ n=1.09\ \ (Houpert\ \ proposal)\ \ or \\ &=0.111\ \ if\ \ n=\frac{10}{9}\quad (Palmgren) \end{aligned} \tag{62}$$

One sees therefore that Palmgren relationship does not respect this possible constraint (i.e., T_{Trans} should be independent of L and R_{x_eq}) since Palmgren is suggesting x_2= 0.8/0.9=0.8889 and x_3=0.

When respecting the latter constraint and using Q_{LC_CST}, the truncation level at Hoeprich's transition reads:

$$T_{Trans} = f_2.\left[\frac{n.x_1}{1.5*f_3}\right]^{\frac{0.5}{1.5-n}} = f_2.\left[\frac{n.f_1.f_2^{0.18}}{1.5*f_3}\right]^{\frac{0.5}{1.5-n}} \tag{63}$$

Using the following table, one sees that the truncation level T_{Trans} is constant (at any k level) and equal to 1.11, hence not equal to 1.

FINAL Proposal using two steps integration and Tripp's results when k > 3000								exponent for Coef:	0.18	n (line contact)	1.09	
								factor for K_LC	L exponent	Rx_exponent		
k	CA	CB	CP	CD	f1	f2	f3	x1 for T_trans=1	x2	x3	f1*f2^0.18	T_Trans
1.00E+00	1.14471424	1.14471424	0.36437386	1.31037070	0.50000000	2.00000000	0.66666667	0.51967151	0.82000000	0.09000000	0.56644194	1.11
5.00E+00	2.46053706	0.85134358	0.22793269	0.96781720	0.31494739	5.00222517	1.05029184	0.38606542	0.82000000	0.09000000	0.42081130	1.11
1.00E+01	3.33986185	0.74228269	0.19259435	0.83322566	0.26950705	7.31774349	1.31478896	0.35377857	0.82000000	0.09000000	0.38561864	1.11
1.50E+01	3.97089212	0.68467792	0.17561717	0.75999140	0.24852180	9.10990283	1.50933965	0.33935205	0.82000000	0.09000000	0.36989373	1.11
2.00E+01	4.47978509	0.64655670	0.16484569	0.71072964	0.23555897	10.62759414	1.66895012	0.33069791	0.82000000	0.09000000	0.36046072	1.11
2.50E+01	4.91342257	0.61851121	0.15711212	0.67411249	0.22643564	11.96872603	1.80676406	0.32476327	0.82000000	0.09000000	0.35399196	1.11
5.00E+01	6.51084808	0.53937279	0.13596114	0.56937293	0.20231444	17.25715303	2.32758086	0.30992373	0.82000000	0.09000000	0.33781687	1.11
7.50E+01	7.65098079	0.49822729	0.12525549	0.51436526	0.19057789	21.33591598	2.71076928	0.30330953	0.82000000	0.09000000	0.33060739	1.11
1.00E+02	8.56832945	0.47112118	0.11828035	0.47805893	0.18309803	24.78480088	3.02536546	0.29937157	0.82000000	0.09000000	0.32631501	1.1108
1.50E+02	10.03544718	0.43562375	0.10921772	0.43058469	0.17356652	30.58703869	3.53925718	0.29473804	0.82000000	0.09000000	0.32126446	1.11
2.00E+02	11.21529527	0.41221732	0.10327720	0.39941868	0.16742572	35.49167710	3.96147977	0.29202394	0.82000000	0.09000000	0.31830609	1.11
2.50E+02	12.21896450	0.39500829	0.09892380	0.37662196	0.16297509	39.82094651	4.32654813	0.29021163	0.82000000	0.09000000	0.31633067	1.11
3.00E+02	13.10133968	0.38152865	0.09552093	0.35885723	0.15952320	43.74061196	4.65176168	0.28890605	0.82000000	0.09000000	0.31490759	1.11
4.00E+02	14.61741123	0.36126617	0.09041565	0.33234251	0.15438493	50.71162320	5.21940687	0.28714268	0.82000000	0.09000000	0.31298552	1.11
5.00E+02	15.90668494	0.34635345	0.08666469	0.31300298	0.15063750	56.86374232	5.71054147	0.28600722	0.82000000	0.09000000	0.31174787	1.11
7.50E+02	18.53194145	0.32093108	0.08028024	0.28045362	0.14430431	69.98748602	6.73299723	0.28441760	0.82000000	0.09000000	0.31001519	1.11
1.00E+03	20.64104761	0.30411515	0.07606268	0.25926943	0.14014519	81.07483456	7.57483225	0.28362937	0.82000000	0.09000000	0.30915601	1.11
1.25E+03	22.43391678	0.29172286	0.07295681	0.24386336	0.13709121	90.85771703	8.30386271	0.28319673	0.82000000	0.09000000	0.30868443	1.11
1.50E+03	24.00922260	0.28199847	0.07052069	0.23190916	0.13469928	99.71239398	8.95412491	0.28295255	0.82000000	0.09000000	0.30841828	1.11
1.75E+03	25.42388151	0.27404636	0.06852917	0.22222892	0.13274520	107.86276927	9.54551016	0.28281942	0.82000000	0.09000000	0.30827316	1.11
2.00E+03	26.71409639	0.26735087	0.06685275	0.21414898	0.13110063	115.45492918	10.09080897	0.28275645	0.82000000	0.09000000	0.30820453	1.11
2.50E+03	29.01273490	0.25654714	0.06414836	0.20125597	0.12844695	129.34340063	11.07584397	0.28275565	0.82000000	0.09000000	0.30820365	1.11
3.00E+03	31.03197496	0.24806372	0.06202528	0.19126505	0.12636192	141.91281072	11.95491713	0.28284833	0.82000000	0.09000000	0.30830468	1.11
4.00E+03	34.49819571	0.23527614	0.05882570	0.17644312	0.12321403	164.25704841	13.49251507	0.28315744	0.82000000	0.09000000	0.30864161	1.11
5.00E+03	37.44302076	0.225837215	0.056464436	0.165699204	0.120884317	183.9673121	14.82584193	0.28352854	0.82000000	0.09000000	0.30904611	1.11
7.50E+03	43.43223094	0.209691781	0.052426135	0.147742567	0.116880883	225.9900473	17.60927753	0.28448087	0.82000000	0.09000000	0.31008414	1.11
1.00E+04	48.23784308	0.198974222	0.049745831	0.136139846	0.114205792	261.4720362	19.90774728	0.28536334	0.82000000	0.09000000	0.31104604	1.11
1.50E+04	55.90271418	0.184832185	0.04620946	0.121251917	0.110647029	321.0839401	23.684656	0.28688286	0.82000000	0.09000000	0.31270232	1.11
5.00E+04	86.38684272	0.148687643	0.037172255	0.085680874	0.101328071	590.2495361	39.8725647	0.29314986	0.82000000	0.09000000	0.31953335	1.11
1.00E+05	110.8118104	0.131282444	0.032820764	0.070013827	0.096669929	837.5758337	53.97893067	0.29785798	0.82000000	0.09000000	0.32466520	1.11
5.00E+05	196.8368809	0.098502499	0.024625648	0.043596129	0.08739908	1885.439089	109.8570946	0.31164102	0.82000000	0.09000000	0.33968871	1.11
1.00E+06	251.7627473	0.087097332	0.021774343	0.035485213	0.083950324	2672.992597	149.5990631	0.31875388	0.82000000	0.09000000	0.34744173	1.11
5.00E+06	444.6916228	0.065534682	0.016383672	0.021922461	0.07693306	6006.815447	308.0817944	0.33794224	0.82000000	0.09000000	0.36835704	1.11
1.00E+07	567.6039966	0.058006673	0.014501669	0.017791102	0.074269923	8510.871175	421.4011625	0.34736159	0.82000000	0.09000000	0.37862414	1.11

Table 3: Miscellaneous Hertzian parameters defined using elliptical integrals function of k.

This means that when using Hoeprich transition, a point contact relationship is erroneously used in the range 1 < T < 1.11 since a non-truncated Hertzian point contact relationship is used while truncation occurs.

The error observed is, however, minor.

Also, for avoiding this error when using Hoeprich's concept, x_1 should simply be equal to 0.28 (instead of about 0.3) for obtaining the same slope at a transition corresponding to a truncation level equal to 1, but the final line contact load used (never reached because of the translation ΔQ) has been artificially reduced by about 2%.

5. NEW MODELS

As explained above, the previous values of the factor *Coef* have been defined at several truncation levels *T* using zero misalignment, CST tool as numerical reference and a cylindrical-on-cylindrical case of reference. *Coef* has then be curve-fitted versus *T*, see eq. (45)).

Although not studied numerically in [4], Houpert suggested some relationships for including misalignment when deriving the factor *Coef.*

The first suggested model was to keep the previous model, replacing however *D* by D_{max} when calculating *Coef*:

$$Model\ 1: Coef_1 \approx \left(f_2.\sqrt{D_{\max}}\right)^{0.18} \quad with\ D_{\max} = D_0 + \frac{k.\theta^2.R_{x\_eq}^2}{2.L^2} = \frac{\delta_{\max}.R_{x\_eq}}{L^2} \tag{64}$$

where D_0 is the dimensionless deformation at the roller-race center while the maximum deformation has already been given in eq. (40):

$$\delta_{\max} = \delta_0 + \frac{\theta^2.R_{y\_eq}}{2} = \delta_0 + \frac{\theta^2.k.R_{x\_eq}}{2} \tag{40}$$

In the latter model, it is implicitly assumed that the maximum deformation occurs between -*L*/2 and *L*/2 and that the full contact length *L* is loaded. These conditions are not fulfilled when studying large *k* ratio and large misalignment, but one will show how to adjust the latter two equations (when deriving $Coef_4$).

Using the appropriate contact boundaries and misalignment, y_{Left} is not equal to $-y_{Right}$, a second suggestion for deriving *Coef* has been given in [4] using a mean value of the truncation level.

It has been demonstrated in the previous chapter that the maximum deformation occurs at abscissa $y_0 = shift = \frac{-\theta.R_{y\_eq}}{r}$ while the left and right abscissa of the non-truncated contact are respectively equal to

$$\begin{aligned} y_{Left} &= y_0 - a_{NT} \\ y_{Right} &= y_0 + a_{NT} \\ with\ \ y_0 &= \frac{-\theta.R_{y\_eq}}{r} \\ a_{NT} &= \frac{f_2}{2}.\sqrt{R_{x\_eq}.\delta_{\max}} \end{aligned} \tag{65}$$

The truncation level on the left and right side is then equal to:

$$T_{Left} = Max\left\{1, \left|\frac{y_0 - a_{NT}}{y_{1end}}\right|\right\} \qquad T_{Right} = Max\left\{1, \left|\frac{y_0 + a_{NT}}{y_{2end}}\right|\right\} \tag{66}$$

(±*L*/2 was suggested in [4] instead of y_{1end} and y_{2end} now)

The second suggestion given in the 2019 paper (ref. [4]) was therefore:

$$Model\ 2: Coef_2 \approx T_{mean}^{0.18} \quad with\ \ T_{mean} = \frac{1}{2}.\left(T_{Left} + T_{Right}\right) \tag{67}$$

In the frame of this project and paper, another idea has been tested and will finally be suggested:

$$Model\ 3: Coef_3 \approx \frac{1}{2}.\left(T_{Left}^{0.18} + T_{Right}^{0.18}\right) = 0.5*\left(Coef_{Left} + Coef_{Right}\right) \tag{68}$$

Meaning that each side of the truncated contact contributes to the load coefficient via a summation of $0.5*T_{Left}^{0.18}$ and $0.5*T_{Right}^{0.18}$, T_{Left} and T_{Right} being as least equal to 1.

A fourth model (using $Coef_4$), close to Model 1, will also be suggested later.

For testing these suggestions, it was however compulsory to have access to numerical results to be used as reference when including misalignment in one extreme case: -10 mrad of misalignment with *k* = 13577.

No access to CST and Cretu’s tools (initially used for defining *Coef*) has unfortunately been obtained, so that the authors used Reusner’s results and model (programmed by O. Menck in the frame of this project) and Dr. Guo’s results who provided graciously his results in the frame of some private communications.

But before calculating results under misalignment, it was interesting and necessary to compare the numerical results obtained next and to benchmark them against ‘exact’ point contact results when no truncation occurs (corresponding to k < 313), see next Table.

Cylinder length = 30 mm								
Total Deformation at contact center = 0.045 mm, zero misalignment								
				Houpert_Analytical	CST Numerical	Numerical	Numerical	Numerical
Rx_eq (mm)	Ry_eq (mm)	k	old Coef	Q_Houpert (N)	Q_CST (N)	Q_Cretu	Guo_Half_101*91	Q_Reusner
10	10	1	1.00	4548				4730
10	1224.33932	122.433932	1.00	22315	22426	22287	22316	
10	2188.28534	218.8285337	1.00	28005	28144		28002	
10	4081.65303	408.1653028	1.02	35941	35641		35449	
10	7397.40741	739.7407407	1.08	41155	40794	40453	40493	
10	11007.4627	1100.746268	1.12	43194	42987		42620	
10	18433.3788	1843.337883	1.18	44873	44842		44404	
10	38340.9108	3834.091083	1.26	46264	46296		45801	
10	135767.325	13576.73252	1.41	47725	47274	46702	46739	49799

Table 4: Miscellaneous results obtained at zero misalignment.

One sees that_CST, Cretu and Guo’s results match quite well for the standard non-truncated point contact case corresponding to $k = 122.43$, while Reusner model deviates slightly from the analytical solution at $k = 1$.

Also, CST, Cretu, Guo’s results and Houpert’s analytical one (calibrated using CST results) are close in the truncated case $k = 739.7$ and $k = 13577$, (the case of reference used next when studying misalignment effects on the load and moment), while a slightly different load is obtained with Reusner’s model at the largest k value.

For all the reasons mentioned above, it has been decided to pursue the calibration effort (including misalignment) with Guo’s results.

Prior to this exercise and for information purposes, some pressure distributions calculated along the contact with zero misalignment are shown next:

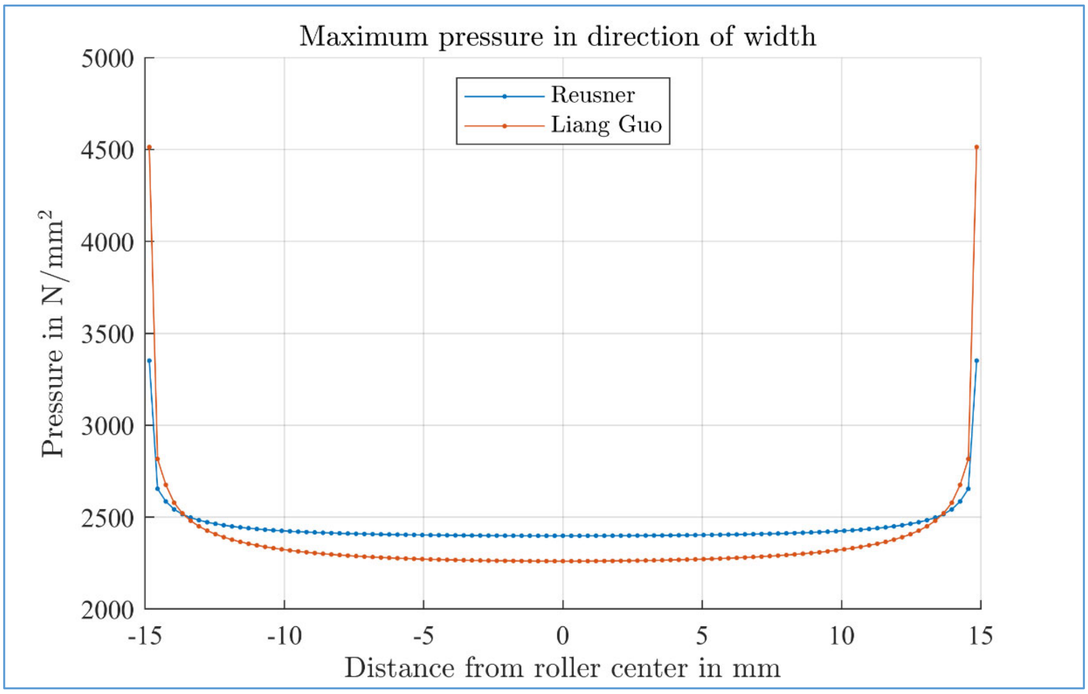

Figure 19 : Reusner’s model and Guo’s results obtained with k=13576

Reusner’s load is equal to 49799 N while Guo’s load is equal to 46737 N.

One should not pay too much attention on the substantial differences noticed on the pressure spikes amplitudes since it is known that their accuracy is also a function of the number of slices used. Also, all these dry and linear elastic models don’t consider elasto-plastic model, roller hardening and running – in effects as well as EHL effects. The use of a lubricant limiting shear stress also limits the Poiseuille shear stress, hence the film thickness h, pressure gradient dP/dx and dP/dy, hence the pressure spikes as shown for example by Houpert in [11].

Guo also calculated the same cases using 1001 slices (instead of 101 previously used) for obtaining a load of 46854 N (instead of 46739 when using 101 slices)

The CST and Houpert's modified Teutsch results are also shown next, with an analytical load equal to 47725 and Teutsch load equal to 48489 N.

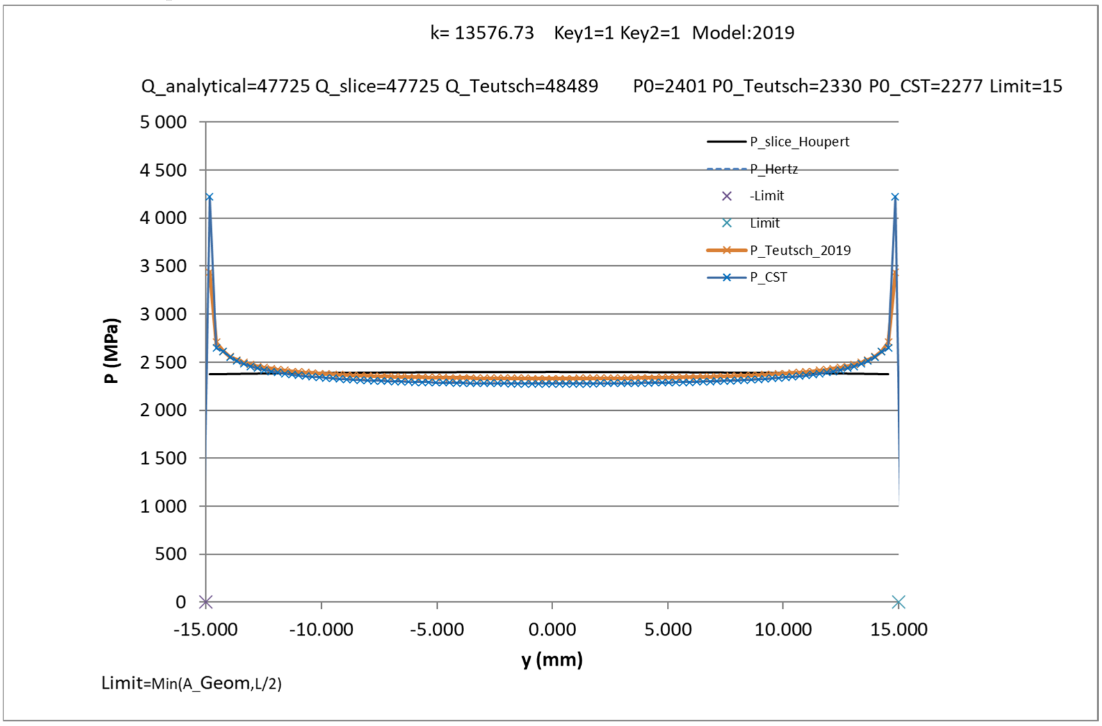

Figure 20 : CST and Houpert modified Teutsch results obtained with k=13576

Following is the load and pressure distribution calculated with Reusner's model and Guo's one when using a relative roller – inner race misalignment fixed to – 10 mrad:

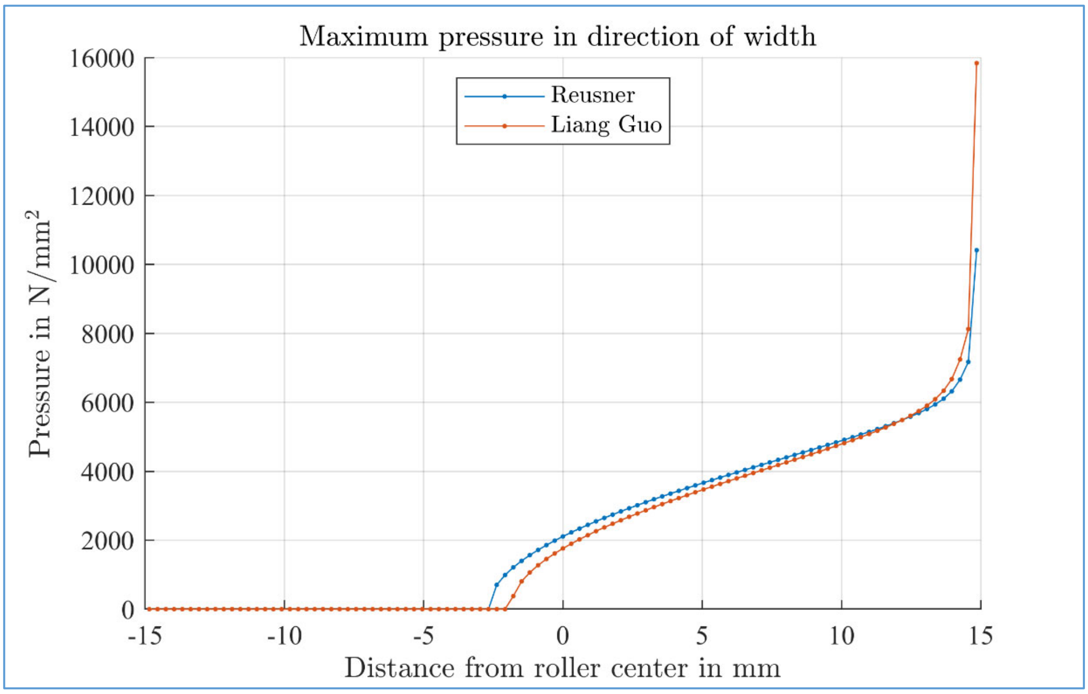

Figure 21 : Reusner and Guo's results obtained with k=13576 and -10 mrad of misalignment

Reusner's load is now 87075 N instead of 49799 N when no misalignment occurs.

Guo's load is 87828 N using his half space model and Guo's corresponding roller tilting moment around the race center is 906613 N.mm

The latter two results will be used next as target when benchmarking and fine-tuning the correction factor *Coef*. The following table summarizes several results obtained:

delta0 (mm)	**0.0450**		D_max	0.0759
D0	5.00E-04		T_max	84.1189
T0	6.83E+00		**Coef_1**	**2.2207**
Exponent used for Coef	**0.1800**			
Coef_old (no Misal & single crown)	**1.41**		T_mean	84.4802
			Coef_2	**2.2224**
Tilt (mrad)	**-10.00**			
Q_old (N) includ. Misaligment	**70443**		Coef_Left	1.00
			Coef_Right	2.51
delta_max (mm)	6.8334		**Coef_3**	**1.76**
Q_NT_PC (N)	289694246		**Q_Anal. Trunc_PC_single Crown (N)**	**87615**
a_NT (mm)	1261.7841		**Q_Slice_MRD (N)**	**87615**
shift y0 including θ/r (mm)	1257.62		**Q_Anal_MRD (N)**	**87615**
y_Left_NT (mm)	-4.16		Selected y_Left for Teutsch	-4.16
y_Right_NT (mm)	2519.41		Selected y_Right for Teutsch	15.00
T_Left	1.00E+00		**Q_Mod_Teutsch_2019 (N)**	**85887**
T_Right	1.68E+02		**Q_ISO_16281 (N)**	**83781**
			Coef_4	**1.76**
			Exponent used for Coef'3	**0.229**
			Coef'_3	**2.11**
			M_Anal. Trunc_PC_single Crown (N.mm)	**906613**
			Moment Teutsch_2019 (N.mm)	**963747**
			M_ISO_16281 (N.mm)	**731276**

Table 5: Results obtained at large misalignment and large crown radius.

Several outputs are printed in this table:

- the analytical load defined using a single crown radius
- the load obtained using any MRD profile and slices
- the analytical load using analytical relationships for deriving the left and right contact boundaries as well as a summation of the analytical loads calculated in 8 MRD zones. In our case, the MRD profile is using 4 equal radii and corresponds to a single crown contact.
- The final analytical load calculated with the previously described three options

The previous tabel shows that the targeted load (Guo's load of 87828 N) is almost retrieved when using $Coef_3$ ($Coef_3$ = 1.76) calculated with the previously suggested exponent 0.18. The final analytical load is then equal to 87615 N.

This is a remarkable result when realizing the severity of the test conducted: the large crown radius and misalignment lead to a theoretical maximum deformation and shift (occurring out of the contact) of 6.83 mm and 1257.62 mm respectively (see left column of the previous table), with a non-truncated contact ellipse half-length of 1261.78 mm and a left and right theoretical contact boundaries of -4.16 mm and 2519.41 mm, physically limited to -4.16 and + 15 mm for obtaining a final left and right truncation level of T equal to 1 and 168 respectively.

Also shown in the latter table is the load obtained using Houpert's modified Teutsch approach (85887 N) as well as the load obtained when using the ISO16281 approach with 101 lamina and the Palmgren contact stiffness 83781 N).

The pressure distribution calculated by Houpert's miscellaneous models are shown next, including the Hertzian contact pressure distribution of the very shifted truncated point contact (dotted line), remarkably close to the pressure obtained using Houpert's load in each slice.

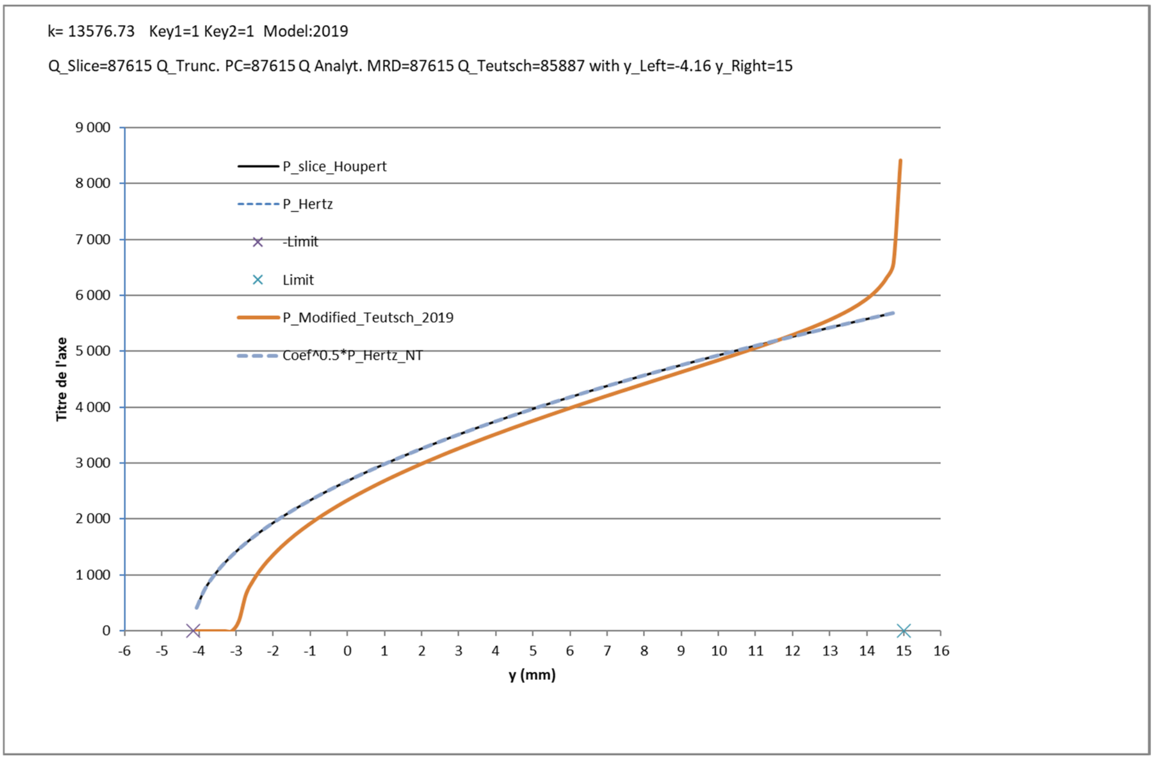

Figure 22 : Houpert's pressure distribution calculated with k=13576 and -10 mrad of misalignment

Table 5 also shows the factor *Coef*$_4$, defined using the real maximum deformation and contact length (when using a single crown profile):

$$Coef_4 = Max\left\{1, \left[f_2\sqrt{\frac{\delta_{\max\_real}.R_{x\_eq}}{y_{Right}-y_{Left}}}\right]^{0.18}\right\}$$

$$with:$$

$$\delta_{\max\_real} = \delta_0 + \frac{\theta^2.R_{y\_eq}}{2} \qquad if\ \ |y_0| \le \frac{L}{2}\ \ and\ \ y_0 = -\frac{\theta.R_{y\_ea}}{r} \tag{69}$$

$$\delta_{\max\_real} = Max\left\{\delta_0 - r^2.\frac{L^2}{8.R_{y\_eq}} - \theta.r.\frac{L}{2}, \delta_0 - r^2.\frac{L^2}{8.R_{y\_eq}} + \theta.r.\frac{L}{2}\right\}\ if\ |y_0| > \frac{L}{2}$$

The left and right contact bounds (and real max deformation) can also be defined using an MRD profile if needed. The latter fourth model (using *Coef*$_4$) is similar the first model (using *Coef*$_1$), the difference being that the real maximum deformation δ_{max_real} calculated in the range -*L/2* to +*L/2* is used, as well as the real contact length, (y_{Right}-y_{Left}), now replacing *L*. The use of *Coef*$_4$ could be recommended for keeping a certain consistency with the previous suggestion (in [4], defining *Coef* using the maximum deformation under misalignment), but it is difficult to physically explain why *Coef*$_4$ is almost equal to *Coef*$_3$ and certainly easier to promote the use of *Coef*$_3$ because of its plausible physical explanation (differentiating the left and right truncation effects on the load magnification). *Coef*$_3$ can of course be used at zero misalignment, being then equal to the previously described factor *Coef.*

The latter table also shows the calculated analytical roller moment defined using *Coef'*$_3$ for which it was necessary to update, in a first step, the exponent used *T*. This exponent is now equal 0.2287 instead of 0.18 for matching Guo's moment taken as targeted moment (906613 N.mm).

$$Coef'_3 = 0.5*\left[T_{Left}^{0.229} + T_{Right}^{0.229}\right]\ \ (To\ use\ \ for\ \ calculating\ \ the\ \ moment) \tag{70}$$

The physical explanation of why *Coef'*$_3$ is larger than *Coef*$_3$ is that a pressure spike effect on the moment is larger than its effect on the load because of its effect on the moment is magnified by the largest distance of the spike relative to the race center. The derivation of *Coef'*$_3$ could however be fine-tuned in a second step for considering including the roller length if needed.

In conclusions, a suggested analytical load and moment, using *Coef₃ and Coef'₃* have been validated at large misalignment and zero misalignment using the following proposals:

$$Q_{pc\_trunc} = E_{eq}.Coef_3.f_1 \cdot \left[\Delta_0 \left(y_{2end} - y_{1end} \right) - \frac{r^2}{6 \cdot R_{y\_eq}} \left(y_{2end}^3 - y_{1end}^3 \right) - \frac{\theta.r}{2} \left(y_{2end}^2 - y_{1end}^2 \right) \right] \quad with$$

$$y_{1end} = \max \left[\frac{R_{y\_eq} \cdot \left(-\theta - \sqrt{\theta^2 + 2.\frac{\Delta_0}{R_{y\_eq}}} \right)}{r} ; -\frac{L}{2} \right] \qquad y_{2end} = \min \left[\frac{R_{y\_eq} \cdot \left(-\theta + \sqrt{\theta^2 + 2.\frac{\Delta_0}{R_{y\_eq}}} \right)}{r} ; \frac{L}{2} \right] \tag{71}$$

$$M_{pc\_trunc} = Coef'_3.f_1.E_{eq} \cdot \left[\frac{\Delta_0}{2} \left(y_{2end}^2 - y_{1end}^2 \right) - \frac{r^2}{8 \cdot R_{y\_eq}} \left(y_{2end}^4 - y_{1end}^4 \right) - \frac{\theta.r}{3} \left(y_{2end}^3 - y_{1end}^3 \right) \right] \tag{72}$$

with:

$$\begin{gathered} Coef_3 = 0.5 * \left[T_{Left}^{0.18} + T_{Right}^{0.18} \right] = T_{Right}^{0.18} \quad when\ misalignment\ is\ nil \\ Coef'_3 = 0.5 * \left[T_{Left}^{0.229} + T_{Right}^{0.229} \right] \\ with: \\ T_{Left} = Max \left\{ 1, \left| \frac{y_0 - a_{NT}}{y_{1end}} \right| \right\} \qquad T_{Right} = Max \left\{ 1, \left| \frac{y_0 + a_{NT}}{y_{2end}} \right| \right\} \\ with\ \ y_0 = \frac{-\theta.R_{y\_eq}}{r} \qquad a_{NT} = \frac{f_2}{2}.\sqrt{R_{x\_eq}.\delta_{\max}} \qquad and \quad \delta_{\max} = \delta_0 + \frac{\theta^2.R_{y\_eq}}{2} = \delta_0 + \frac{\theta^2.k.R_{x\_eq}}{2} \end{gathered} \tag{73}$$

Where M is the moment applied on the roller (at the roller – inner race contact) relative to the inner race center and θ is the relative roller – inner race misalignment or tilting angle. Appropriate signs corrections must of course be considered when calculating the roller moment corresponding to the roller – outer race contact. When using a complex profile (not a single crown profile), the left and right contact boundaries y_{1end} and y_{2end} should be replaced by the MRD contact boundaries defined analytically (relationships not given in this report) or corresponding to the min and max y abscissa of the loaded slices.

6. Conclusions

A comprehensive summary of contact models is given in this report, Houpert's contribution being outlined in a chronological or logical order.

When zero misalignment is assumed and a simple crown profile is used, analytical dimensionless relationships have been shared for describing in a uniform manner point contact, truncated point contact and line contact models (load, pressure, and contact dimensions), thanks to the newly suggested linear load – deflection model used and possibility of integrating analytically the load in all slices.

When complex profiles are used, the loads and moment in each slice can be added numerically.

The suggested model also accounts for the coupling effects and pressure spike effects on the load, effects included via a correction factor called *Coef* and curve-fitted versus some numerical results obtained with appropriate tools including these pressure spikes. In the frame of this study, misalignment has been included for defining the coefficient *Coef₃* and *Coef'₃* used for calculating the roller load and tilting moment respectively, *Coef₃* remaining equal to *Coef* when no misalignment occurs.

Acknowledgments

The author would like to thank Prof. Poll, from IMKT department at Leibniz University and Dr. Matthias Stammler, from the IWES department of the Fraunhofer Institute, who sponsored this work.

A special thanks is also given to Dr. Liang Guo, who shared in the frame of some private communications his numerical results obtained with and without misalignment.

References :

1. J.H. Tripp, “Hertzian contact in two and three dimensions,” NASA technical paper 2473 (July 1985)
2. G. Dalmaz, “Le Film Mince Visqueux dans les Contacts Hertziens en Regime Hydrodynamique et Elastohydrodynamique” (“Thin Viscous Film in Hertzian Contacts in Hydrodynamic and Elastohydrodynamic Regimes”), Docteur d’Etat Es Sciences Thesis, INSA, Lyon, France (1979)
3. L. Houpert, “An Engineering Approach to Hertzian Contact Elasticity – Part I”, Jour. Tribology, Vol. 123, pp. 582-588, July 2001
4. L. Houpert, “Novel analytical and numerical calculations in truncated point contact: Single crown profile and no misalignment”, Bearing World Journal Vol. 4 (2019) page 39 – page 58, https://www.vdma-verlag.com/home/bearingworld19.html
5. L. Houpert, J. Clarke & C. Penny (2023) “Tribological Models for Advanced Ball Bearing Simulation”, Tribology Transactions, DOI: 10.1080/10402004.2023.2213470
6. M. Hoeprich, “Numerical procedure for designing rolling element contact geometry as a function of load cycle,” SAE technical paper, series 850764 (1985)
7. S. Cretu, “initial plastic deformation of cylindrical roller generatrix stress distribution analysis and fatigue life tests”, Acta Tribologica, Vol. 4, 1-2, p.1-6, 1996.
8. H. Reusner, “Druckflächenbelastung und Oberflächenverschiebung im Wälzkontakt von Rotationskörpern, Dissertation T H Karlsruhe, 1977
9. W. Wang, L: Guo, P.L. Wong, Z.M. Zhang, “Surface normal deformation in elastic quarter-space“ Tribology International, Volume 114, October 2017, Pages 358-364
10. L. Houpert, “Miscellaneous Engineering Approaches to Contact Elasticity Calculations”, Bearing World International Bearing Conference, Kaiserslautern, Germany, 6–7 March 2018
11. L. Houpert, C. Penny & J. Clarke (2023), “Bearing Models for Advanced Ball Bearing Simulation”,
12. L. Houpert, “An Engineering Approach to non-Hertzian Contact Elasticity – Part II “, ASME Jour. Tribology, Vol. 123, pp. 589-594, July 2001
13. R. Teutsch and B. Sauer, “An alternative slicing technique to consider pressure concentrations in non-Hertzian contacts,” *J. Tribol* 126(3), 436-442 (June 28, 2004)
14. L. Houpert , B. Hamrock, “Elastohydrodynamic calculations used as a tool to studying scuffing”, Proc. 12th Leeds-Lyon Symp., 1985

Tool chain for wear prediction of journal bearings in planetary gears in wind turbines

Benjamin Lehmann[1], Georg Jacobs[1], Mattheüs Lucassen[1], Thomas Decker[2],
Anuj Khare[1], Dennis Bosse[2], Shiqi Wang[1]

[1] *Institute for machine elements and systems engineering, RWTH Aachen University*
[2] *Chair for Wind Power Drives, RWTH Aachen University*

Abstract – To increase the power density of the mechanical drive train of wind turbines, journal bearings can be used as planetary gear bearings instead of rolling bearings. This technological change presents new challenges. For example, wind turbine drive trains are subject to dynamic and low-speed operating conditions, which can lead to accelerated abrasive wear of the journal bearings. In addition, oil supply failure or peak loads due to wind gusts and grid and power converter faults could potentially result in catastrophic failure due to adhesive wear in a very short time. Such operating characteristics are, therefore, critical regarding the journal bearing wear and must be considered in the design. The successful implementation of journal bearings in wind turbines depends on a reliable estimation of wear. In this paper, a multiscale tool chain for the wear calculation of planetary gear bearings in wind turbines is presented. The tool chain consists of a combined multi-body and elasto-hydrodynamic (EHD) simulation model of the sliding contact as well as different wear models for the wear calculation. The tool chain is parameterized on a component test rig. In addition, the tool chain will be validated on a system test rig under wind-typical load conditions. The results of this paper will show that the developed tool chain can be applied to reliably predict the wear-related roughness smoothing and contour change of journal bearings for planetary gears in wind turbines. Furthermore, on the basis of the developed tool chain it is possible to make important design decisions, which are related to the use of journal bearings in wind turbine drivetrains.

Keywords – wear calculation, journal bearing, wind turbine, planetary gear

1. Introduction

Wind energy is one of the mainstays of renewable power generation. In order to realize increasing economic efficiency of wind power one important objective is the decrease of levelized costs of electricity (LCOE). This can be achieved through an increase in wind turbine power rating and reduction of costs during operation and maintenance. The reduction of operational expenses (OpEx) is especially important for the offshore wind sector where maintenance and repair of damaged components is estimated to impact the LCOE with up to 30 % [1]. An increased reliability of wind turbine drive trains can therefore aid in reducing the LCOE. Due to their unlimited fatigue lifetime journal bearings are advantageous in terms of drive train reliability.

A second advantage of journal bearings is the compact design. In order to increase the power density of modern wind turbine drive trains, the size of the planetary gears in the installed planetary gearboxes is reduced and the number of planetary gears is increased at the same time. Since the installation space available for planetary gear bearings is limited, journal bearings are increasingly being used. The two aforementioned advantages of journal bearings over the conventional rolling element bearings have led to a technology change in the wind turbine: In recent years journal bearings have been replacing rolling element bearing as planetary bearings in wind turbine gearboxes [2].

Planetary gears with journal bearings are already established in the wind industry, however, these journal bearings can be subject to wear due to the operating conditions typical for wind turbines. The quality of the wear prediction methods for those bearings is poorly quantified. In addition, experience regarding the use of journal bearings in wind turbines over the total turbine lifetime of up to 20 years is not yet available. Furthermore, unsteady wind conditions result in frequent start-ups of the WT or low speeds. Such operating conditions are of particular relevance for journal bearings in terms of wear.

Wear is the progressive loss of material from the surface of a body caused by tribological stress [3]. Depending on the structure of the tribological system and the kinematics of the tribological stress, a distinction is made between different types of wear. According to CZICHOS [3], the four wear mechanisms for journal bearings are adhesion, abrasion, micro fatigue and tribochemical reaction. In order to predict the bearing wear analytically, different models have been developed in the past, which are based on different wear mechanisms. HOLM [4] developed a wear model, by assuming the contact between atoms of opposing surfaces as the cause of wear. ARCHARD [5] developed this model further and considered not the contact of atoms, but the contact and the resulting plastic deformation of asperity peaks of the surfaces. ROWE [6] extended the model developed by ARCHARD to include the influence of the lubricant used in the wear calculation. CHUN [7] used the model created by ROWE to predict wear of journal bearings in start-stop operations of a reciprocating engine by means of simulation. Besides ARCHARD, the most widely used model for wear calculation is the energetic model developed by FLEISCHER [8]. In this model, it is assumed that friction energy is generated during the sliding process, which is accumulated in the material. If the accumulated energy has reached a critical limit, the lattice energy of the material is overcome and wear occurs.

The wear models according to ARCHARD and ROWE assume a linear wear process in their calculation, which means that the wear rate does not change during the wear process. However, when observing real wear processes in journal bearings, a deviation from this prediction can be observed. It can be seen that the wear rate $\dot{H}_W$ is initially higher than the one predicted by the linear wear calculations and only approaches the wear behavior of the linear forecasts after a run-in phase has been completed [9]. Simultaneously with the change in the rate of wear, the coefficient of friction also changes. In lubricated friction contacts, the friction process usually starts with increased coefficients of friction until wear leads to a smoothing of the surfaces and the value of the coefficient of friction decreases [10].

In the recent past, attempts have been made to take the run-in phase of a journal bearing into account in the wear calculation and thus to be able to predict the entire course of wear more accurately. In FLEISCHER'S wear model, the behaviour of the friction coefficient is not specified in more detail. Therefore, FLEISCHER'S wear model can be implemented both linearly, with a time-constant friction coefficient, and with transient behaviour, using a time-varying friction coefficient. KÖNIG [10], using FLEISCHER'S approach, developed a numerical method for wear prediction of radial loaded journal bearings with a diameter of 30 mm for static operating conditions and certain dynamic conditions (e.g. start-stop operation), iteratively considering both the journal bearing wear at macroscopic level and at roughness level. In this way, a simulative prediction of run-in wear became possible using the FLEISCHER model. By means of the developed method, agreements of the wear in the run-in process between simulation and experiment could be shown. Nevertheless, the approach according to KÖNIG uses input parameters for the wear calculation, which were determined experimentally on a 30mm journal bearing under radial load. The transfer to a planetary journal bearing has not yet been carried out. In addition, KÖNIG takes global roughness smoothing into account, but does not resolve it locally depending on the differently loaded zones in the journal bearing. Another model that enables transient wear calculation was developed by XIANG ET AL. In this model, two mechanisms are assumed to contribute to wear [11]. First, wear is considered to be caused by the plastic deformation of asperity peaks in contact; this affects the material above contact surface. On the other hand, it is assumed that fatigue cracks develop below the contact surface and lead to the breakout of material after a certain accumulation. As an alternative to these mechanical models, the wear model according to LIJESH [12] based on the work of BRYANT [13] uses a thermodynamic approach to describe wear. The free enthalpy is assumed to decrease proportionally to the degradation of the tribological system until an equilibrium state is reached at the minimum free enthalpy. Since the decrease in free enthalpy is coupled to the generation of entropy, the increase of entropy is regarded as the driving variable of wear in the model. The wear behaviour is described with the aid of a degradation coefficient, which sets the wear volume created in relation to the entropy produced. A summary of the wear models for journal bearing wear calculation is shown in Table 1.

Table 1: Wear models for journal bearing wear calculation and basic wear mechanism

Wear model	Year	Damage mechanism considered	Wear rate
Holm	1946	Adhesion	Constant
Archard	1953	Adhesion/Abrasion	Constant
Rowe	1966	Adhesion	Constant
Fleischer	1980	Adhesion/Abrasion	Constant/ Transient
Bryant	2008	Adhesion	Constant/ Transient
Chun	2016	Adhesion	Transient
Lijesh	2018	Adhesion/Abrasion	Transient
Xiang	2019	Ahesion/Micro fatigue	Transient

In [14] LEHMANN implemented the wear models according to ARCHARD, FLEISCHER, CHUN, LIJESH and XIANG and coupled them with an EHD/MBS simulation model of a journal bearing in order to create a tool chain for the prediction of wear of journal bearings in planetary gears. Since the models according to HOLM, ROWE and BRYANT only represent preliminary development stages of the previously mentioned models, they were not considered further. The aim of LEHMANN's study was a screening and evaluation of the different wear models regarding their suitability for the wear calculation of planetary gear bearings in wind turbines. The evaluation criteria were parameter uncertainty, the effort for parameter determination, the number of parameters, the load case dependency of the wear models and the calculation time. The results of this study showed that the wear calculation according to LIJESH is the overall best model for wear calculation according to the previously mentioned evaluation criteria. Nevertheless, the calculation results of the implemented wear models have not yet been compared with experimental data for a final evaluation of the wear models. In recent months, a wear calculation toolchain has been developed that enables a transient wear calculation of planetary gear journal bearings in wind turbines under consideration of the continuous local contour and roughness adaption. This tool chain uses the aforementioned wear models. In [15] a first test of the functionality of the tool chain and a first parameterization of the wear models according to FLEISCHER based on first experimental results of a component test rig could already be carried out. However, the further parameterization and evaluation of the wear models as well as the transfer and validation of the tool chain on a planetary gear journal bearing have not yet been carried out.

In this work, the working procedure of tool chain is presented and a parameterization strategy of the wear models according to ARCHARD, FLEISCHER, CHUN, LIJESH and XIANG is presented. For the parameterization of the wear models the wear results from a component test rig are used. Furthermore, a transfer of the tool chain to the real application is conducted by comparing the results of the tool chain to the results of an experiment on a subsystem test rig, which represents a planetary gear journal bearing. In this way the transfer of the parameterized tool chain to a real system is demonstrated as the subsystem test rig is able to reproduce real load situations of a planetary journal bearing.

2. Simulation Methodology of the tool chain

The tool chain used in this work consists of a combined multi-body and elastohydrodynamic (EHD) simulation model of the sliding contact, which is implemented in the commercially available software AVL Excite power Unit.

The EHD simulation is coupled with the different wear models, which are implemented in MATLAB and allow a data transfer via a Python interfaces between AVL Excite Power Unit and MATLAB. By applying wind typical loads to the multi-body/EHD model of the planetary journal bearing the structural deformation of the pin and the planetary gear are calculated as well as the contact conditions in the sliding contact such as hydrodynamic and asperity contact. Wear critical contact conditions occur when the roughness peaks come into contact within the journal bearing and lead to asperity contact and therefore mixed friction and wear. For the calculation of the asperity contact pressure p_a the surface roughness is modelled with the statistical model of GREENWOOD and WILLIAMSON [16]. For modelling the near-surface flow and pressure behaviour of the fluid in narrow gaps the average flow model according to PATIR and CHENG [17] is used. The average flow considers the influence of the surface properties in the Reynolds equation extending the Reynolds equation by pressure and shear flow factors. The wear generated by asperity contact leads to a material removal and thus a continuous change in the contour and roughness of the journal bearing over time which can be calculated by the tool chain as follows (see also Figure 1):

First the local oil film height and hydrodynamic pressure are calculated by the multi-body/EHD model and transferred to the contact model. Based on the contact model the wear-influencing variables, such as the local asperity contact pressure and shear stress are calculated and transferred to the wear models. The wear models are then used to calculate the wear height of the bearing contour. The calculated wear height is transferred to the surface model, which maps the local roughness via patches on the bearing surface. Based on the local calculated wear height the local surface roughness parameters are updated using the algorithm published in [10]. This allows a physically based consideration of the roughness smoothening during the wear process. The resulting change in the bearing contour and roughness is fed back into the multi-body/EHD calculation. The change in contour and roughness influences the pressure distribution developing in the journal bearing and thus the further progress of wear. An iterative calculation was implemented in order to model the interaction between contour and roughness change and the wear generation. The data exchange between the EHD model and the wear model takes place at defined iteration intervals. The iteration criterion can be the accumulated iteration step duration or maximum wear height per iteration step. In this work a constant maximum wear height per iteration step is chosen as the iteration criterion. The simulation is terminated automatically after the overall accumulated simulation time reaches a predefined value $t_{acc,max}$.

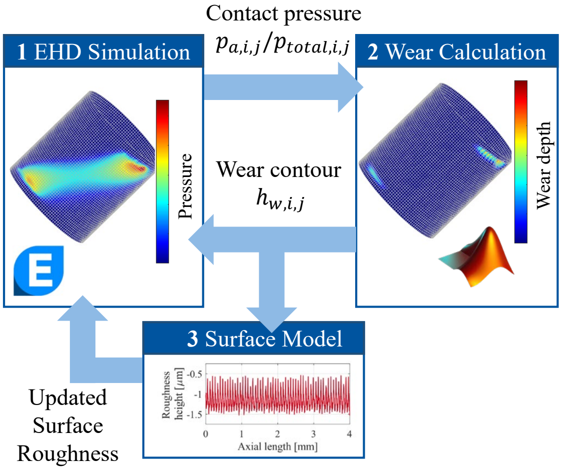

Figure 1: Schematic visualization of the functional workflow of the wear calculation

3. Parameterization and Validation methodology

The wear models presented here follow a physical approach, but contain one empirical parameter that require prior determination based on experiments. In the following the methodology to determine the empirical parameter for each wear model and the methodology to validate the wear calculation is presented. The parameters of the considered wear models including the empirical wear parameters, which have to be determined experimentally, are presented in Table 2. When the wear calculation models developed by FLEISCHER and LIJESH were used, the coefficient of friction is calculated using the formula by OFFNER and KNAUS [18] describing the friction in mixed lubrication regimes.

Table 2: Parameters of the wear models

Wear model	Parameter	Parameter name	Value
ARCHARD	k	Wear coefficient	Empirical parameter
	H	Hardness	932 N/mm^2
FLEISCHER	e_R^*	Friction energy density	Empirical parameter
	μ	Friction value	Calculated according to [18]
LIJESH	$B(t)$	Degradation coefficient	Empirical parameter
	μ	Friction value	Calculated according to [18]
XIANG	α	Propagation angle fatigue fracture	0,314 [-]
	E	Modulus of elasticity	70,000 N/mm^2
	β	Asperite radius	1.5 µm
	D	Asperite density	Calculated from roughness measurement
	κ	Fatigue coefficient	Empirical parameter
	μ	Friction value	Calculated according to [18]
CHUN	t_0	Vibration time Lubricant in adsorbed state	7.03·10^{-17} s
	E_a	Adsorption energy	48,116 J/mol
	α_χ	Diameter Influence area of a lubricating film molecule	1.13·10^{-9} m
	k_C	Wear coefficient	Empirical parameter

For the determination of the empirical parameters of the wear models a component test rig is used, which is described in more detail in section 4.1. Although the component test rig does not reproduce the real load situation of a planetary gear journal bearing, it allows wear experiments to be carried out quickly and reproducibly by applying circumferential speeds, pressures and temperatures comparable to those in the field. The results of the wear experiments are used to determine the empirical wear parameters. To determine the empirical wear parameters, the generated wear height and wear volume is determined over time in the test bearing. Based on the generated wear height and wear volume over time the wear rate is calculated. The focus for the parameterization is on the linear wear phase after completion of the run-in process, as the surface roughness and contour of the bearing barely change here and the wear rate is stationary (cf. Figure 2). The stationary wear rate allows a simple calculation of the empirical wear parameters as presented in the following.

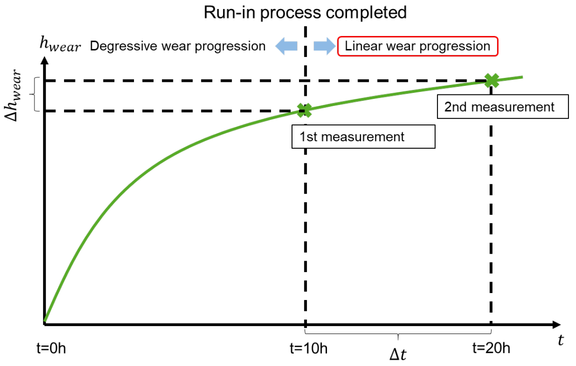

Figure 2: Wear process over time and times of measurement of the journal bearings to determine wear

In order to determine the stationary wear rate the following procedure is used. The journal bearing is removed and measured after ten hours, when the run-in process has been completed and a second time after twenty hours, when the journal bearing has been operated ten more hours in the mixed friction regime with a stationary wear rate. The equations of the wear models are rearranged according to the empirical wear parameter. The empirical wear parameter can then be determined by inserting the stationary wear rate resulting from the experiments.

The calculation of the wear parameter is demonstrated exemplarily on the wear model according to ARCHARD. In the model according to ARCHARD [19] the wear volume is related to the contact force acting on a body F_{asp}, the sliding distance s_R, the reciprocal of the hardness H and a proportionality factor k. The proportionality factor k describes the probability of material removal due to plastic deformation of the asperity peaks and is the wear parameter which has to be determined experimentally.

$$V_V = \frac{k}{H} \cdot F_{asp} \cdot s_R \qquad \textit{Eq. 1}$$

By dividing the equation by the journal bearing surface and the time, the correlation between the wear rate $\dot{h}_{wear}$, the acting asperity contact pressure p_{asp} and the sliding speed u can be established.

$$\dot{h}_{wear} = \frac{k}{H} \cdot p_{asp} \cdot u \qquad \text{Eq. 2}$$

Finally, the equation is rearranged according to the wear parameter k.

$$k = \frac{\dot{h}_{wear} \cdot H}{p_{asp,max} \cdot u} \qquad \textit{Eq. 3}$$

The contact conditions, such as the asperity contact pressure, are required to calculate the wear parameters. Here, the maximum asperity contact pressure occurring at the maximum worn point is considered. The maximum asperity contact pressure results from an EHD calculation considering the real contour and roughness.

For an initial validation of the parameterized wear model, the first 20 hours including the run-in process are simulated on the component test rig using the tool chain. Afterwards the resulting wear progress is compared with the experiment. Parameterization and validation are considered successful if the resulting wear rate, wear height, wear contour and roughness match the experiment.

4. Wear calculation and comparison to experimental results

The parameterization of the wear models is carried out on a component test rig due to the simple design and the rapid reproducibility of the wear results. The component test rig enables the testing of radially loaded journal bearings under mixed friction conditions.

4.1. Component test rig

The component test rig for radially loaded journal bearings is displayed in Figure 3. It comprises of an electric motor-driven shaft which rotates around the inner circumference of the radially-loaded journal bearing. The bearing itself is mounted into a rotatable enclosure which is pulled against the shaft by a hydraulic actuator to apply pressure. The test rig can exert up to 60 MPa of specific pressure $\bar{p} = F_N/(B \cdot D)$ on the journal bearing at sliding speeds ranging from 0.03 to 3.66 m/s. A force transducer and a lever connected to the bottom of the bearing enclosure forms a friction gauge that measures the friction torque induced in the bearing.

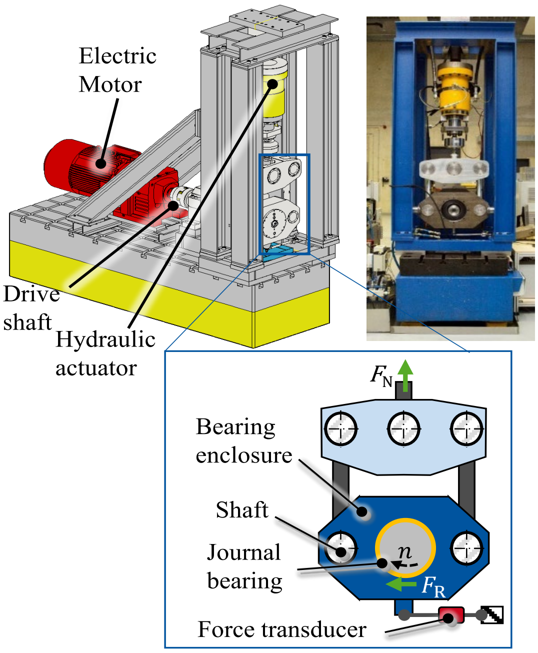

Figure 3: Component test rig for journal bearings

An oil supply unit ensures lubrication of the gap between shaft and journal bearing. Additionally, bearing and lubricant temperatures can be controlled using heating cartridges.

4.1.1. Testing procedure

The test bearings are manufactured from continuously casted CuSn12Ni2-C alloy. The shaft material is 18CrNiMo7-6 steel. For lubrication a typical wind turbine gearbox oil (Castrol Optigear 320 CT, a PAO with viscosity class of ISO VG 320) is used. Further specifications of the journal bearings used for the experiments are given in Table 3.

Table 3: Specifications of the test bearings

Parameter	Property
Bearing diameter	120 mm
Bearing width	30 mm
Bearing clearance (radial)	90 µm
Bearing material	CuSn12Ni2-C
Shaft material	18CrNiMo7-6
Oil	ISO VG 320

For the wear experiments constant operating conditions (according to speed, specific pressure and temperature) in the mixed friction regime are chosen. A full duration experiment consists of two test runs with a total duration of 10 h each. After each test run the test bearing is dismantled from its enclosure for a tactile surface measurement. The measurements of the surface contour and roughness are compared to an initial measurement of the bearing's surface characteristics performed prior to testing. The tests performed on the component test rig and their operating conditions are shown in Table 4.

Table 4: Tests performed on the component test rig

Load case	Repetitions	Specific pressure	Sliding speed	Temperature
1	2	25 MPa	0.1 m/s	55°C
2		30 MPa		
3		35 MPa		

An exemplary measurement result for the friction moment M_{Fr} and the bearing temperature T for the load case 25 MPa and 0.1 m/s for the first 10 hours is shown in Figure 4. Figure 5 shows the further progression of the friction moment M_{Fr} and the bearing temperature T for the period: 10 to 20 hours.

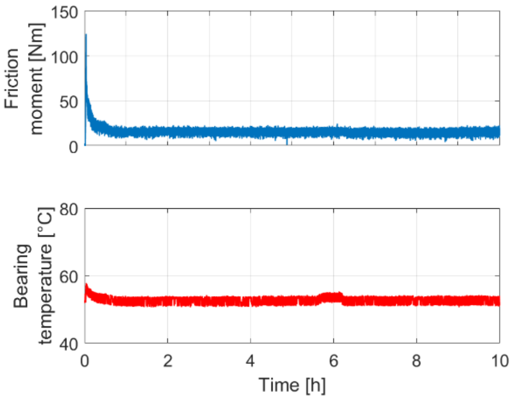

Figure 4: Measurement result for the friction moment and the bearing temperature measured at the test rig for the load case 25 MPa and 0.1 m/s: 0 to 10 hours

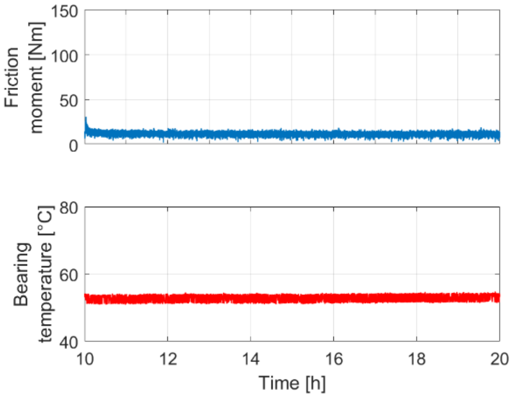

Figure 5: Measurement result for the friction moment and the bearing temperature measured at the test rig for the load case 25 MPa and 0.1 m/s: 10 to 20 hours

The diagrams show the running-in behaviour of the bearing at 25 MPa of specific pressure and 0.1 m/s of sliding speed. During the first hour of operation the highest friction occurs. After 1 to 2 hours the friction moment has converged towards a constant value which indicates a stationary wear rate.

4.1.2. Wear measurement

The occurring wear on the test bearings is determined by means of a tactile surface measurement. The objective of the wear measurement is a quantified wear volume V_W, local wear height h_W and local surface roughness values for different points in time during the test campaign. The wear measurement process is visualized in Figure 6. The axial contour of the bearing and the corresponding local wear heights are measured at specific circumferential positions i. Measurements are taken prior to testing, after 10 hours and after 20h hours of the journal bearing operation in mixed friction.

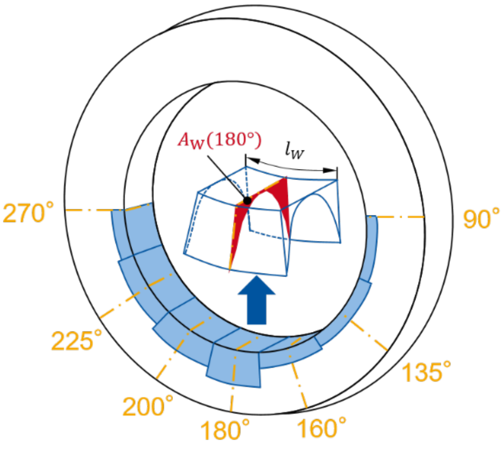

Figure 6: Schematic depiction of the tactile measurement of the planimetric wear

By subtracting the worn bearing profile measurement from the initial measurement, the surface area at each measurement position $A_{W,i}$ is obtained. From this so-called planimetric wear the wear volume V_W is calculated according to Eq. 4

$$V_W = \sum_{i=1}^{N} l_{W,i} \cdot A_{W,i} \tag*{Eq. 4}$$

with $l_{W,i}$ being the bow length between the different measurement positions. In this approach the wear profile $A_{W,i}$ is assumed to be constant within each interval.

Table 5 shows the operating points and the corresponding results of the max. measured wear height and wear volume after 10 and 20 hours. Based on the wear results the wear rate is calculated and additionally shown in Table 5.

Table 5: Determined wear height, wear volume and wear rate from the wear tests on the component test rig

Load case	Wear height/ wear volume after 10h	Wear height/ wear volume after 20h	Wear rate
25 MPa,	4.5 µm	4.9 µm	0.04 µm/h
0.1 m/s	1.7 mm³	2.5 mm³	0.08 mm³/h
30 MPa,	2.6 µm	3.7 µm	0.11 µm/h
0.1 m/s	2.9 mm³	3.4 mm³	0.15 mm³/h
35 MPa,	10.3 µm	12.3 µm	0.20 µm/h
0.1 m/s	14.0 mm³	15.2 mm³	0.12 mm³/h

4.1.3. Parameterization results of the wear models

The wear measured on the test bearings is used to parameterize the different wear models introduced before. The considered wear models are the models according to Archard, Fleischer, Chun, Xiang and Lijesh [3-7]. Since the models according to Holm, Rowe and Bryant only represent preliminary development stages of the previously mentioned models, they are not considered further. In Table 6 the determined experimental wear parameters for the wear models are shown.

Table 6: Determined experimental parameters of the wear models

Wear model	Parameter	Value 25 MPa	Value 30 MPa	Value 35 MPa
ARCHARD	k	$1.392\cdot10^{-8}$ [-]	$3.829\cdot10^{-8}$ [-]	$6.962\cdot10^{-8}$ [-]
FLEISCHER	e_R^*	$1.894\cdot10^{17}$ [J/m³]	$6.885\cdot10^{16}$ [J/m³]	$3.787\cdot10^{16}$ [J/m³]
LIJESH	$\dot{h}_0$	1250.10 µm/h	185.65 µm/h	125.01 µm/h
	$\dot{h}_s$	0.04 µm/h	0.11 µm/h	0.20 µm/h
	τ_{wt}	0,2 h	0,2 h	0,2 h
XIANG	κ	1.753 [-]	1.832 [-]	1.947 [-]
CHUN	k_C	$3.634\cdot10^{-6}$ [-]	$9.997\cdot10^{-7}$ [-]	$1.818\cdot10^{-6}$ [-]

The degradation coefficient $B(t)$ according to LIJESH is a time-dependent value and can be calculated using the following formula:

$$B(t) = \frac{\dot{h}_s \cdot \left(1 + \left(\frac{\dot{h}_0}{\dot{h}_s} - 1\right) \cdot e^{-\frac{t}{\tau_{wt}}}\right) \cdot T}{u \cdot p_{asp,max}} \qquad \text{Eq. 5}$$

The degradation coefficient comprises the initial wear rate $\dot{h}_0$, the stationary wear rate $\dot{h}_s$ (applies after the run-in process) a time constant τ_{wt} to describe the duration of the running-in process, the effective bearing temperature T, the circumferential speed u and the asperity contact pressure p_{asp}. For the determination of the degradation coefficient, the maximum asperity contact pressure $p_{asp,max}$ resulting from an EHD-calculation with the measured bearing contour and bearing roughness was considered.

In the following, the results of the wear simulation are shown exemplarily for the load case 35 MPa and 0.1 m/s. Figure 7 shows the max. experimentally determined wear height compared to the calculated wear height over time. Figure 8 shows the max. calculated wear rate over time in comparison to the experimental wear rate determined in the stationary state. The results of the CHUN and ARCHARD wear models are identical. Therefore, the wear model according to CHUN is not shown here.

The simulated wear height $h_{W,sim}$ after 20 hours is 11.63 µm for the LIJESH wear model, 5.03 µm for the ARCHARD wear model, 3.59 µm for the FLEISCHER wear model and 3.01 µm for the XIANG wear model. The experimentally determined wear height $h_{W,meas}$ within two repetition tests is 11.68 µm and 12.90 µm. The wear models according to ARCHARD, FLEISCHER and LIJESH show a simulated wear rate $\dot{h}_{W,sim}$ after 20 h of 0.15 – 0.25 µm/h, which is corresponding to the experiments. The wear models according to XIANG shows a significantly lower simulated wear rate $\dot{h}_{W,sim}$ of 0.02 µm/h and thus does not show good agreement with the experimental results. Only the wear model according to LIJESH reaches the experimentally determined absolute wear height h_W of 11.6 – 12.2 µm and stationary wear rate $\dot{h}_W$ of 0.2 µm/h at the same time. This is due to the time-variant wear coefficient in the LIJESH model, varying especially during the run-in phase. In this way, the wear generated during the run-in phase can be modelled more accurately by the simulation tool chain.

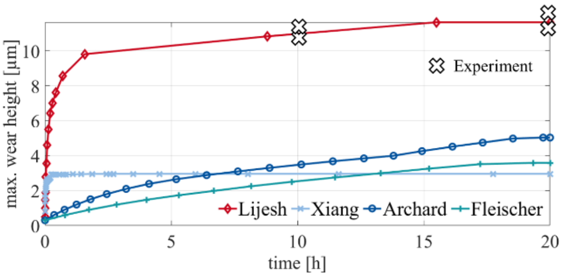

Figure 7: Experimental determined and calculated wear height over time on the component test rig

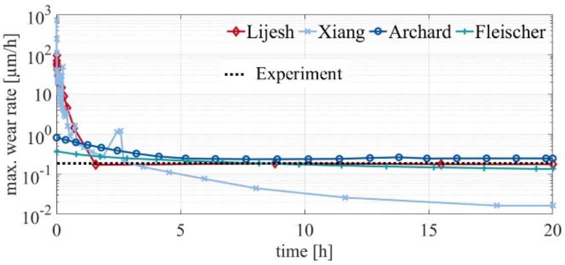

Figure 8: Experimental determined and calculated wear rate over time on the component test rig

Considering the progression of the wear curves in Figure 7 it can be determined after which time the run-in process is complete. In the wear calculation according to ARCHARD and FLEISCHER, the run-in process is completed after approx. 5 to 10 hours. The transient wear rate changes to a constant wear rate after 10 hours and the surface roughness parameters do not change any further. In the wear calculation according to LIJESH, the run-in process is completed after 1 to 2 hours. The friction torque measured in the experiment is used to compare the simulated run-in process with the experiment (cf. Figure 4). Figure 4 shows that the friction torque assumes a stationary value of 11 Nm after approx. 1 to 2 hours. Reaching a stationary value of the frictional torque indicates that the surface properties of the journal bearing in the experiments barely change any further and the run-in process is complete. Since the run-in time of approx. 1 to 2 hours determined experimentally corresponds best with the simulated run-in time of 1 to 2 hours, the wear model according to LIJESH is therefore the most suitable wear model for representing the run-in process.

Figure 9 shows the calculated wear contour of the journal bearing and compares it with the experimentally determined wear contour after 0 hours (initial contour) and 20 hours (worn contour). The wear contour calculated using the LIJESH wear model comes closest to the experimentally determined wear contour.

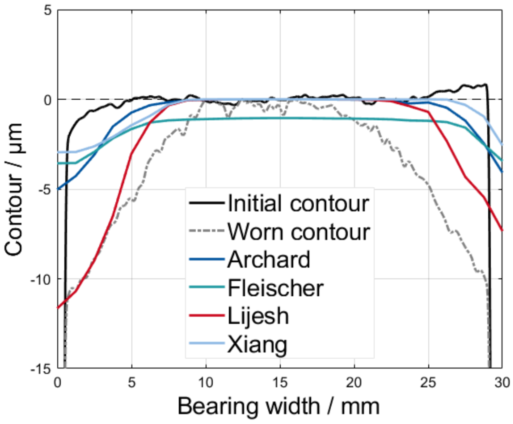

Figure 9: Comparison of experimental determined initial and worn contour of the journal bearing and comparison with the simulation results

Since the wear calculation according to LIJESH corresponds best with the experimental wear results, the wear calculations according to LIJESH are focused in the following. Figure 10 shows the initial roughness of the surface and the according to LIJESH calculated roughness after 10 hours and compares this with the roughness measured in the experiment (see Figure 11). Both the nominal values of the resulting roughness after 10 hours and the areas of smoothing roughness are in good agreement between the simulation and the experiment.

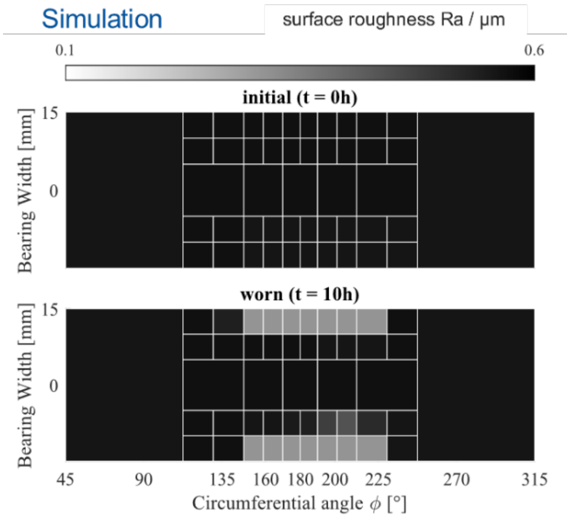

Figure 10: Simulated roughness profile after t=0h and t=10h

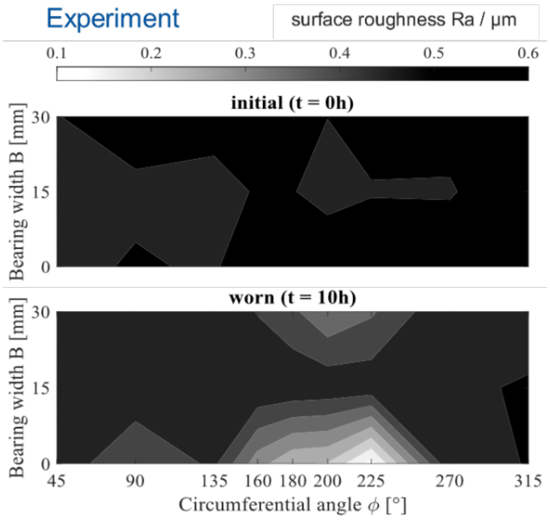

Figure 11: Experimental determined roughness profile after t=0h and t=10h

Figure 12 shows the wear progress calculated using the LIJESH wear model for the load cases 25 MPa, 30 MPa and 35 MPa at 0.1 m/s and compares this with the experimentally determined wear heights. Overall, a good agreement between simulation and experiment can be observed.

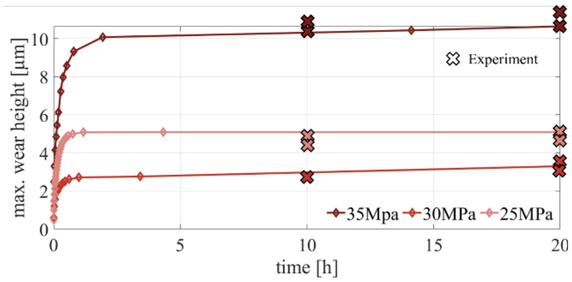

Figure 12: Experimental determined wear height and wear height calculated by the LIJESH model for 25 MPa, 30 MPa and 35 MPa at 0.1 m/s

In order to transfer the wear calculation according to LIJESH to other systems, the locally occurring asperity contact pressure is considered at the three operating points. The hypothesis is that the wear parameter of the LIJESH model can be transferred to systems that experience the same local asperity contact pressure. Figure 13 shows the simulated asperity contact pressure of the component test rig bearing with consideration of the measured worn in bearing profile and roughness after 10 hours. The resulting asperity contact pressure is shown for the three operating points a) 25 MPa, b) 30 MPa and c) 35 MPa at 0.1 m/s.

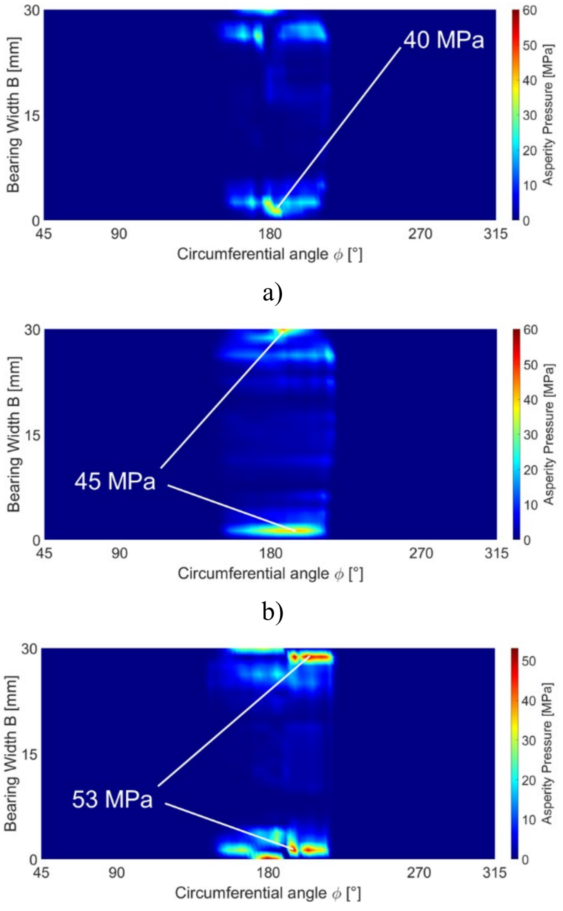

a)

b)

c)

Figure 13: Simulated asperity contact pressure of component test rig bearing with worn in bearing profile and roughness for a) 25 MPa, b) 30 MPa and c) 35 MPa at 0.1 m/s

The maximum asperity contact pressure for load case 35 MPa and 0,1 m/s is 53 MPa, for load case 30 MPa and 0,1 m/s 45 MPa and for load case 25 MPa and 0,1 m/s 40 MPa. The values of the asperity contact pressures are later compared with the values of the asperity contact pressures calculated for the subsystem test rig in order to select the correct parameter set for the Lijesh wear model from Table 6.

4.2. Subsystem test rig

The following section first describes the design and functionality of the subsystem test rig and the conducted experiments, followed by a description of the method for the transfer of the tool chain to the subsystem test rig. The subsystem test rig consists of three gear wheels, which represent the sun, planet and ring gear of a planetary gearbox. The tested journal bearing is positioned in the planet gear. Due to the arrangement of the subsystem test rig it is able to reproduce the real load situations of a planetary journal bearings induced by the forces in the tooth contact, such as radial, planet tilting in case of a helical gearing and planet ovalization (cf. Figure 14).

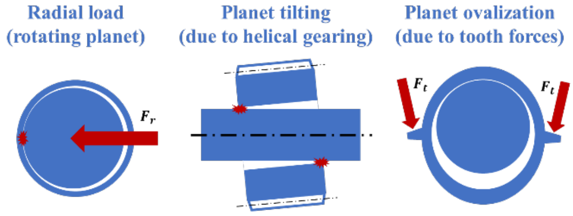

Figure 14: Load situations in a planetary gear journal bearing

An overview of the test rig is given in Figure 15 [8]. The loading on the journal bearing results from the two gear contacts to the sun and ring gear, which leads to comparable bearing loads as in wind turbine planetary gearboxes. This results in the test rig being able to reach specific bearing pressures of up to 15 MPa and sliding speeds of 0.6 m/s.

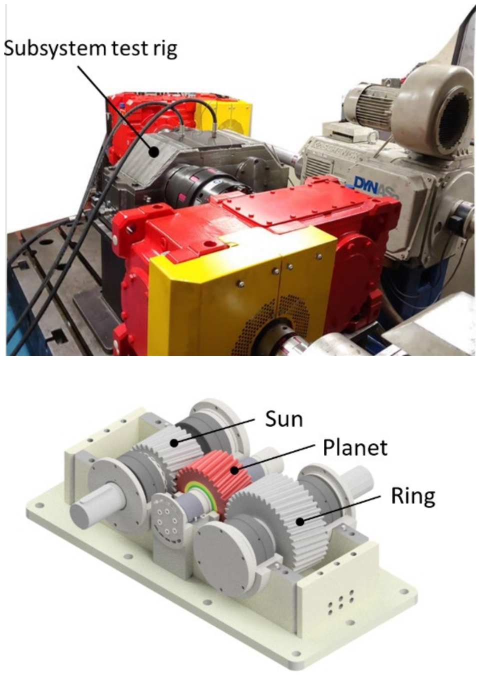

Figure 15: Subsystem test rig (top) and schematic structure of the subsystem test rig (bottom)

The bearing temperature is monitored at two positions. These are placed below the bearing surface at each side of the load zone. The temperature of the lubricant can be controlled by use of heating cartridges. A thermoelectric voltage measurement system (Schaller BEAROMOS®2020) is used at the journal bearing to determine possible mixed friction conditions.

4.2.4. Testing procedure and results

The test bearings are manufactured from continuously casted CuSn12Ni2-C alloy. The gear material is 18CrNiMo7-6 steel. For lubrication the Castrol Optigear 320 CT is used. Further specifications of the journal bearings used for the experiments are given in Table 7.

Table 7: Specifications of the test bearings

Parameter	Property
Bearing diameter	100 mm
Bearing width	112 mm
Bearing clearance (radial)	55 µm
Bearing material	CuSn12Ni2-C
Shaft material	18CrNiMo7-6
Oil	ISO VG 320

At the test rig two types of experiments are carried out to validate the developed tool chain. The first experiment is for determining the Stribeck curve, in particular the transition from hydrodynamic to mixed friction regime. With this experiment it is possible to validate the EHD-model on which the tool chain is based on. The second experiment is for determining the wear volume and wear height after a defined time of operating the journal bearing in mixed friction regime and is used to validate the wear results of the tool chain under realistic load conditions for planetary journal bearings. For the Stribeck curve tests the bearing is operated in the hydrodynamic lubrication regime and the sliding speed is reduced in steps to enter the mixed lubrication state. The change of regime is visible in the contact resistance measurement and is compared to the EHD results. For reasons of scope, the experiments on the Stribeck curve and the validation of the EHD model will be discussed in more detail in a future paper. In this paper, the focus is on the wear experiments to determine the generated wear. For the wear experiments the test rig is operated in the mixed friction regime for several hours (up until 24 h), after which the tested bearing is disassembled. After the testing, the bearing surface is measured considering the surface contour, roundness and roughness. The measurement positions are given in Figure 16. The wear height and wear volume are measured analogue to the aforementioned approach (cf. Figure 6).

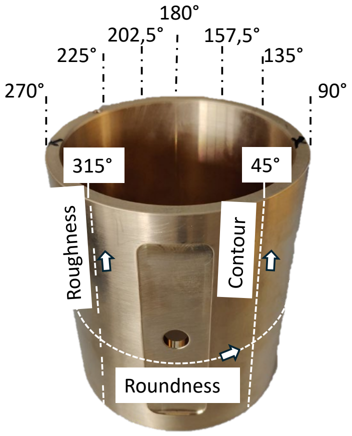

Figure 16. Measurement positions of roughness, roundness and contour of the planetary bearing

Table 8 shows the tests carried out on the subsystem test rig for the transfer and validation of the tool chain at subsystem level. The test bearing was operated for 24 hours at a constant operating point in mixed friction.

Table 8: Tests performed on the subsystem test rig

Load case	Repetitions	Specific press.	Sliding speed	Temperature	Duration
1	1	12 MPa	0.1 m/s	50°C	24h

In Figure 17 the thermoelectric voltage results of the 24-hour wear experiment are given. The subsystem test rig was operated with a constant lubricant temperature of 50 °C. The temperature of the bearing remained at a constant temperature of 50 °C as well. Nevertheless, the thermoelectric voltage signal shows a strong drift of -50 µV to 50 µV in the first hour, which is an indicator of the run-in process. After the first hour, the thermoelectric voltage shows a positive and wavy pattern in the range of 50 µV which indicates constant mixed friction conditions during the entire testing time. It can therefore be concluded that the run-in process was completed within the first hour, that the journal bearing was then operated continuously under mixed friction and that wear was generated continuously during that time.

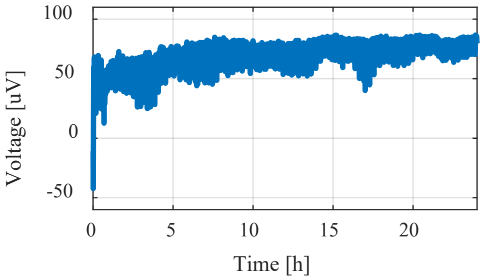

Figure 17. Contact resistance signal for a 24h wear experiment with 12 MPa specific pressure, 0.1 m/s sliding speed and lubricant temperature of 50 °C

4.2.5. Validation of tool chain

In order to validate the tool chain and the wear models with respect to the application to journal bearings in planetary gears in wind turbines, the experimental results of the three-shaft test rig are compared with the results of the calculated wear. For the selection of the correct wear parameters, the aforementioned methodology was used: First the asperity contact pressure occurring in the subsystem test rig under the considered load case of 12 MPa and 0.1 m/s (see Figure 18) was examined and compared with the asperity contact pressure of the component test rig (see Figure 13). Then the wear parameters from Table 6 were selected according to the load case on the component test rig, which leads to similar local asperity contact pressures observed on the subsystem test rig. This applied to the wear parameters of load case 35 MPa and 0.1 m/s since the maximum simulated asperity contact pressure in this load case is 53 MPa, which is comparable to the maximum asperity contact pressure occurring on the subsystem test rig (cf. Figure 13 and Figure 18).

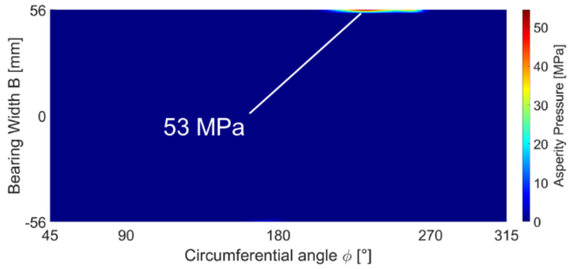

Figure 18: Simulated asperity contact pressure of subsystem test rig bearing with worn in bearing profile and roughness for 12 MPa an 0.1 m/s

Therefore, in the following the wear parameters in Table 6 for the operating point of 35 MPa and 0.1 m/s were used. Figure 19 shows the maximum simulated wear height $h_{W,sim}$ over time for the Archard, Fleischer and Lijesh wear model on the subsystem test rig in comparison with experimental results. Since the Xiang wear model did not show good agreements with the experimental results in regard to the wear height and wear rate in the previous chapter, the wear calculation according to Xiang was neglected here.

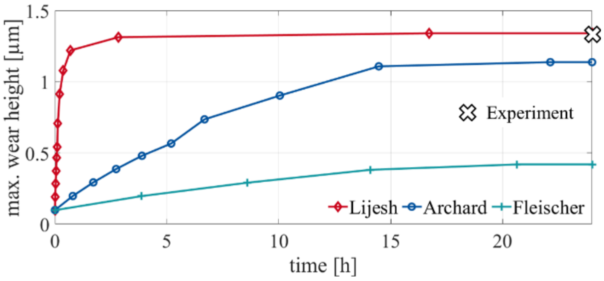

Figure 19: Experimental determined and calculated wear height over time on the subsystem test rig

It can be seen in Figure 19 that the simulated wear height $h_{W,sim}$ is 1.34 µm for the Lijesh wear model, 1.14 µm for the Archard wear model and 0.42 µm for the Fleischer wear model. The experimentally determined wear height $h_{W,meas}$ is 1.31 µm. The run-in process calculated with the Lijesh wear model is completed after 2 h, the run-in process calculated with the Archard and Fleischer wear model is completed after approx. 15 h. The calculated wear height according to Archard and Fleischer again shows a deviation from the experimental determined wear height. Nevertheless, the wear height calculated with the Archard wear model comes very close to the experimentally determined wear height for the subsystem test rig model. The wear calculation according to Lijesh again shows the best agreement between the calculated and the experimentally determined wear height h_W. The wear calculation according to Lijesh also shows good agreement with the experiment in terms of the duration of the run-in process (cf. Figure 17).

Figure 20 shows the initial roughness of the surface and the according to Lijesh calculated roughness after 10 hours. This can be compared with the roughness measured in the experiment (see Figure 21). The nominal values of the resulting roughness after 24 hours are in good agreement between the simulation and the experiment. However, deviations can be seen in the areas of smoothed roughness. While only a smoothing of the roughness at the edges can be seen in the simulation, the roughness in the experiment is smoothed within a larger area, which extends further into the center of the journal bearing. In addition, the area of roughness smoothing at the lower edge of the journal bearing is slightly shifted. This indicates that the calculation of the component deformation in the built-up EHD model of the subsystem test rig differs slightly from reality. The EHD model of the subsystem test rig will therefore be validated and optimized further in future.

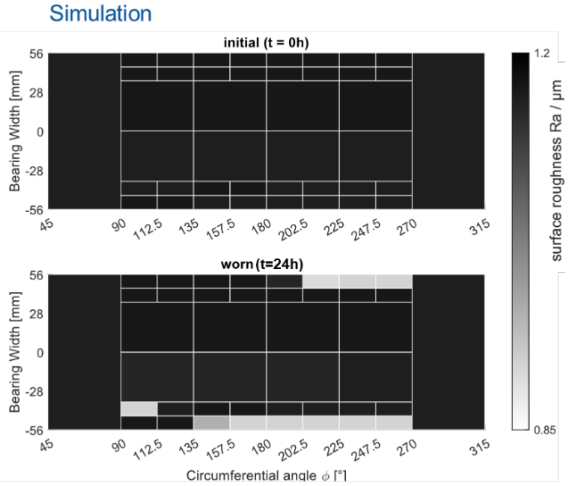

Figure 20: Simulated roughness profile after t=0h and t=24h

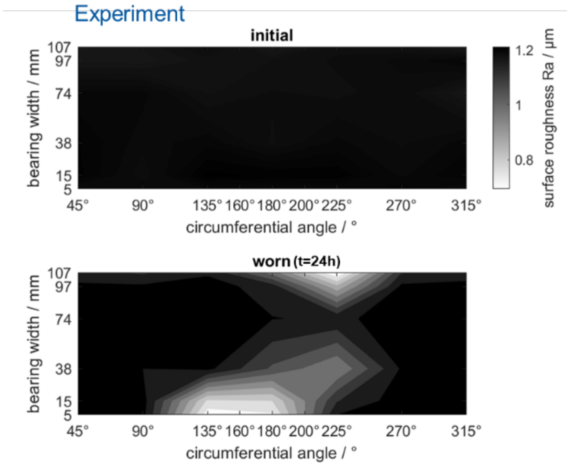

Figure 21: Experimental determined roughness profile after t=0h and t=24h

5. Conclusion

This work presents a multiscale tool chain for the wear calculation of planetary gear journal bearings in wind turbines, its parameterization on component level and its transfer and validation on subsystem level. With a combined multi-body and elasto-hydrodynamic simulation the conditions of the sliding contact such as hydrodynamic pressure and oil film height are calculated. Subsequently using an implemented contact model, the asperity contact is calculated which is input for the wear models according to ARCHARD, FLEISCHER, LIJESH, XIANG and CHUN, which were considered in the tool chain. Based on these wear models the tool chain is able to calculate the resulting wear. Due to a continuous adaption of the journal bearing contour and surface roughness during the wear process an iterative calculation method was implemented in order to account for the continuous journal bearing contour and surface roughness adaption. The wear parameters of the different wear models were parameterized using a developed parameterization method. Input for the parameterization were the wear results generated on a component test rig. This component test rig has a simple design and at the same time can reliably operate the test bearings in a mixed friction condition while simultaneously measuring the frictional torque, thus enabling rapid reproducibility of the wear results. The tool chain was transferred to a subsystem test rig and the wear calculated with the tool chain was successfully validated on a subsystem test rig that reproduces real load conditions comparable to those in planetary journal bearings in wind turbines. In this way, the applicability of the tool chain for use on planetary journal bearings in wind turbines was proven.

The findings can be summarized as follows:

The parameterization of the wear models showed that the models according to ARCHARD and CHUN lead to exactly same wear results. Therefore, the wear model according to CHUN were neglected in the further course. The parameterized models according to ARCHARD, FLEISCHER and LIJESH correctly predict the wear in the stationary wear phase (after the run-in process). The functionality of the parameterization method was therefore fundamentally proven. Nevertheless, only the model according to LIJESH achieves the overall predicted wear height, while ARCHARD and FLEISCHER underestimate the wear height. The XIANG wear model underestimated both: wear height and wear rate. Furthermore, it could be shown that the model according to LIJESH is the only model, which predicts the run-in process accurately. The good agreement of the wear results generated with the LIJESH model can be explained by the degradation coefficient, which can be described as a function of time. The wear calculation using the LIJESH model was then successfully transferred and validated for one load case on the subsystem test rig.

6. Outlook

In future, further parameterization will be carried out in order to consider further wind turbine relevant operating points such as single blade installation or wind turbine start-ups. In addition, the transferability of the tool chain to the subsystem test rig will be further validated by considering these operating points.

In addition to the calculation of the mainly slowly progressing contour and roughness changes due to wear processes considered here, future work will also focus on short-term events leading to spontaneous failures of planetary journal bearings. This includes consideration of seizure of the planetary journal bearings, which results from a disturbance of the thermal equilibrium of the journal bearing. In order to examine the thermal behaviour of the journal bearing under seizure-critical load cases, high thermal inputs due to a lack of lubricant supply or short-term overloads at high sliding speeds are considered.

Acknowledgment

This research was funded by the German Federal Ministry of Economic Affairs and Climate Action

7. References

[1] Tyler Stehly, P. D.: 2021 Cost of Wind Energy Review. 2022

[2] Thys, T. u. Smet, W.: Selective assembly of planetary gear stages to improve load sharing, Bd. 87. 2023

[3] Czichos, H.: Tribologie-Handbuch. Tribometrie, Tribomaterialien, Tribotechnik. Springer eBook Collection Computer Science & Engineering. Wiesbaden: Vieweg+Teubner 2010

[4] Holm, R.: Electric contacts. Alquvist & Wiksells Akademisk Handböker. Stockholm: Gebers 1946

[5] Archard, J. F.: Contact and Rubbing of Flat Surfaces. Journal of Applied Physics 24 (1953) 8, S. 981–988

[6] Rowe, C. N.: Some Aspects of the Heat of Adsorption in the Function of a Boundary Lubricant. A S L E Transactions 9 (1966) 1, S. 101–111

[7] Chun, S. M. u. Khonsari, M. M.: Wear simulation for the journal bearings operating under aligned shaft and steady load during start-up and coast-down conditions. Tribology International 97 (2016), S. 440–466

[8] Fleischer, G.: Verschleiß und Zuverlässigkeit. Verlag Technik 1980

[9] König, F.: Prognose des Verschleißverhaltens ölgeschmierter Gleitlager. Wear Prediction of Plain Bearings under Mixed Friction Conditions, RWTH Aachen Dissertation. Aachen 2020

[10] König, F., Ouald Chaib, A., Jacobs, G. u. Sous, C.: A multiscale-approach for wear prediction in journal bearing systems – from wearing-in towards steady-state wear. Wear 426-427 (2019), S. 1203–1211

[11] Xiang, G., Han, Y., Wang, J., Wang, J. u. Ni, X.: Coupling transient mixed lubrication and wear for journal bearing modeling. Tribology International 138 (2019), S. 1–15

[12] Lijesh, K. P. u. Khonsari, M. M.: On the Modeling of Adhesive Wear with Consideration of Loading Sequence. Tribology Letters 66 (2018) 3

[13] Bryant, M., Khonsari, M. u. Ling, F.: On the thermodynamics of degradation. Proceedings of the Royal Society A: Mathematical, Physical and Engineering Sciences 464 (2008) 2096, S. 2001–2014

[14] Lehmann, B., Trompetter, P., Guzmán, F. G. u. Jacobs, G.: Evaluation of Wear Models for the

Wear Calculation of Journal Bearings for Planetary Gears in Wind Turbines. Lubricants 11 (2023) 9, S. 364

[15] Decker, T., Jacobs, G., Graeske, C., Röder, J., Lucassen, M. u. Lehmann, B.: Multiscale-simulation method for the wear behaviour of planetary journal bearings in wind turbine gearboxes, Bd. 2767. 2024

[16] J.A. Greenwood u. J.B.P. Williamson: Contact of nominally flat surfaces. Proceedings of the Royal Society of London. Series A. Mathematical and Physical Sciences 295 (1966) 1442, S. 300–319

[17] Patir, N. u. Cheng, H. S.: An Average Flow Model for Determining Effects of Three-Dimensional Roughness on Partial Hydrodynamic Lubrication. Journal of Lubrication Technology 100 (1978) 1, S. 12–17

[18] Offner, G. u. Knaus, O.: A Generic Friction Model for Radial Slider Bearing Simulation Considering Elastic and Plastic Deformation. Lubricants 3 (2015) 3, S. 522–538

[19] Archard, J. F.: The wear of metals under unlubricated conditions. Proceedings of the Royal Society of London. Series A. Mathematical and Physical Sciences 236 (1956) 1206, S. 397–410

Influence of deep rolling process at various temperatures on the fatigue life of rolling bearings

Simon Dechant[1], Henke Nordmeyer[2], Florian Pape[1], Bernd Breidenstein[2], Max Marian[1], Gerhard Poll[1]

[1] *Leibniz Universität Hannover, Institute of Machine Design and Tribology, An der Universität 1, 30823 Garbsen, Germany, dechant@imkt.uni-hannover.de*

[2] *Leibniz Universität Hannover, Intitute of Production Engineering and Machine Tools, An der Universität 2, 30823 Garbsen, Germany, nordmeyer@ifw.uni-hannover.de*

Abstract - Global ecological and economic changes necessitate innovative manufacturing technologies that promote resource conservation. In manufacturing, significant potential exists to optimize processes, particularly by targeting residual stresses to enhance the fatigue strength of components. This study investigates an innovative hard turn-rolling process, where the heat generated during hard turning is utilized for a simultaneously conducted deep rolling process. The aim is to gain a deeper understanding of the thermal interactions between these processes and their impact on component service life.

Previous studies have shown that the separate application of hard turning and deep rolling can extend the fatigue life of rolling bearings. In contrast, the combined hard turn-rolling process, despite achieving high compressive residual stresses, did not improve fatigue life and, in some cases, even reduced it. This phenomenon may be attributed to uncontrolled thermal effects in the process, leading to undesirable material changes. To address this, experimental investigations were conducted, focusing on the process parameters and their influence on the material properties of the boundary zone. Detailed material analyses, including microstructural examinations and residual stress measurements, provided insights into the thermal and mechanical effects of the combined process.

This work aims to analyze the interactions between thermal and mechanical effects in the combined hard turn-rolling process. The findings contribute to the development of strategies for process optimization and improving the fatigue life of components.

Keywords – bearings, fatigue life, boundary zone characteristics, hard turning, deep rolling

---

1. Introduction

For bearing fatigue life, the boundary zone characteristics of bearings have a significant impact. The term boundary zone refers to the volume area of the workpiece properties of which are influenced by a machining process [1]. The most important attributes of the boundary zone are hardness, texture, microstructure, residual stresses, and defects like cracks or material faults. Studies have shown, that the functional component behavior under cyclic and quasi-static loading is significantly influenced by these properties [2-5]. According to Sollich, the wear resistance and fatigue life of highly loaded components are significantly influenced by the residual stresses [6]. Thus, compressive residual stresses can lead to an increase in operational strength, as they counteract crack initiation and propagation. Tensile residual stresses, on the other hand, have a negative influence on component life [6- 9]. Denkena et al. were able to show that the fatigue life of rolling bearings can be increased by the targeted induction of compressive residual stresses. However, it should be noted that the achievable increase in fatigue life depends on the strength of the material and the specific residual stress state [10].

The nomenclature used in this paper is listed in Table 1.

Table 1: Nomenclature.

Parameter	Description
f	Feed
HG	Hydrostatical deep rolling tool
p	Pressure
v	Velocity
F	Failure probability
T	Temperature
T_{max}	Characteristic fatigue life
t	Operating time
β	Shape parameter
HV	Vickers hardness
σ	Stress
n	Rotational speed
C	Load capacity
P	Equivalent load
B	Experimental lifetime

2. Hard turning and deep rolling process

The machining process has a significant impact on the properties of components, making the manufacturing process crucial. Typically, rolling bearings are finished through honing and grinding. The combined approach of hard turning and deep rolling is an innovative method and will be described below. Figure 1 illustrates the tool used in the hard turning and deep rolling process. It consists of a cutting tool and a deep rolling tool, arranged in direct succession. This allows the bearing ring to be manufactured in a single process step.

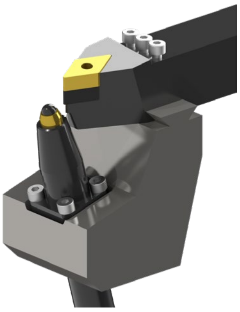

Figure 1: Hard turning and deep rolling tool.

The process can be defined by the parameters feed rate *f*, velocity v_c, and rolling pressure p_W, as shown in figure 2. The listed parameters of the machining process can significantly influence the properties of the boundary zone.

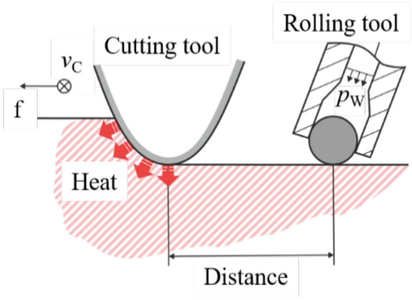

Figure 2: Schematic diagram of the hard turning and deep rolling process.

The cutting edge generates a high local heat input into the component during material removal. The thermally affected zone extends up to the deep rolling tool, thereby influencing the mechanical process of deep rolling. By adjusting the distance between the hard turning tool and the roller deep rolling tool, the overall process can also be influenced.

Given the inherent complexity of the hard turning process and the multitude of parameter variations it involves, this work focuses on understanding the interplay between thermal and mechanical processes. To achieve this, the conventional hard turning process is replaced with an inductive heating source, which enables precise control of the thermal energy input into the workpiece, as shown in figure 3. This approach allows for accurate management of temperature distribution within the workpiece and facilitates a deeper understanding of the interactions between thermal effects and mechanical processing conditions.

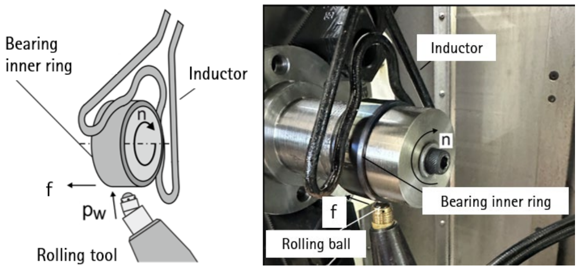

Figure 3: Principle process setup (left) and machine configuration (right).

3. Material analysis

In this study, a cylindrical roller bearing of type NU206 is used as test specimen (see figure 4).

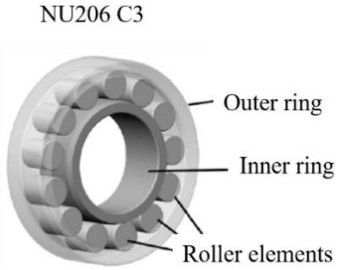

Figure 4: Cylindrical roller bearing of type NU206.

Table 2 shows the key dimensions of the bearing.

Table 2: Dimension of test specimen.

Type:	NU206
Shaft-Ø:	30 mm
Outer-Ø:	62 mm
Width:	16 mm
C_r:	46 kN
Material:	100Cr6

A typical operational load for the bearing corresponds to a load ratio of 4. The resulting maximum Hertzian pressure on the inner ring is approximately 2.5 GPa. Figure 5 shows the Hertzian pressure distribution.

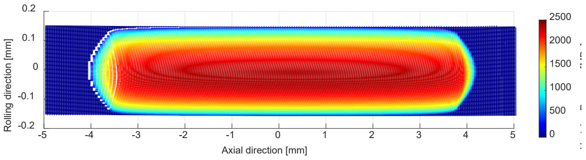

Figure 5: Hertzian pressure distribution for a NU206 bearing and a load ration of 4.

Figure 6 illustrates the resulting stress state below the surface. During rolling contact, the highest stresses occur below the surface. Therefore, the properties of the boundary zone are of particular interest. In this work and for the corresponding bearing, the boundary zone is defined as the first 300 µm beneath the surface. The maximum stress in this case is observed at a depth of 112 µm. The aim is to improve the boundary zone characteristics in this area through a targeted machining process to increase the bearing's fatigue life.

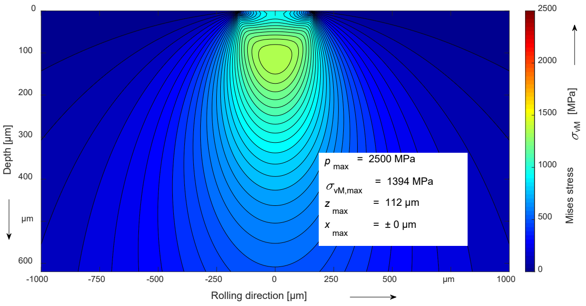

Figure 6: Von Mises stress distribution for maximal Hertzian pressure of 2.5 GPa.

To analyze the thermal influence on the deep rolling process, the experimental setup shown in Figure 3 is used. This setup allows for precise control of the desired surface temperature, as previously described. For the machining process, reference bearing inner rings with a ground and honed surface are used as the test specimen. The relevant machining process parameters are listed in Table 3.

Table 3: Machining process parameters.

Rolling tool:	HG-6
Induction heating:	Himmelwerk SINUS 105
Feed rate *f*:	0.12 mm
Rolling speed v_C:	100 m/min
Rolling pressure p_W:	200 bar
Roll. temperature *T**:	20 – 400 °C

**Surface temperature*

The following sections discuss the relevant surface and boundary zone characteristics, including hardness, residual stress state, and microstructural condition.

3.1. Hardness analysis

The temperature at the component surface was measured using a pyrometer to ensure accurate readings. The surface hardness measurements (see fig. 7) after deep rolling at elevated temperatures show no significant difference between the reference bearing inner ring, which was not deep rolled, and the inner ring that was deep rolled at room temperature. At an elevated deep rolling temperature of 100 °C, an increase in surface hardness of 50 HV1 is observed, reaching approximately 800 HV1. With further increases in deep rolling temperature, the surface hardness decreases and falls below the reference hardness at temperatures above 300°C.

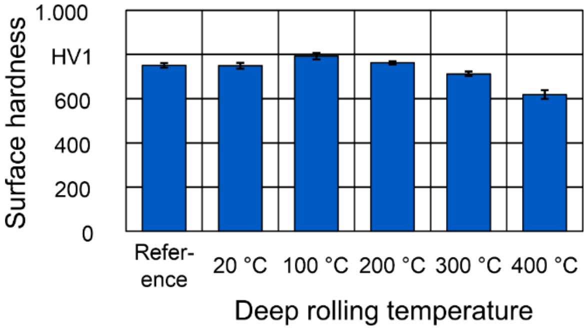

Figure 7: Hardness measurement at the surface after deep rolling at elevated temperatures.

The measurements were conducted in the middle of the raceway. Figure 8 shows the measured hardness-depth profiles. No significant changes are observed up to 200 °C. The hardness is highest close to the surface, ranging between 850 and 900 HV0.02. With increasing depth, the hardness decreases slightly and stabilizes at around 800 HV0.02. For the high deep rolling temperatures of 300 °C and 400 °C, the overall shape of the measured hardness profile remains the same, but at a lower level. At 300 °C, a hardness reduction of 12 % is observed, and at 400 °C, a reduction of 23 % is detectable.

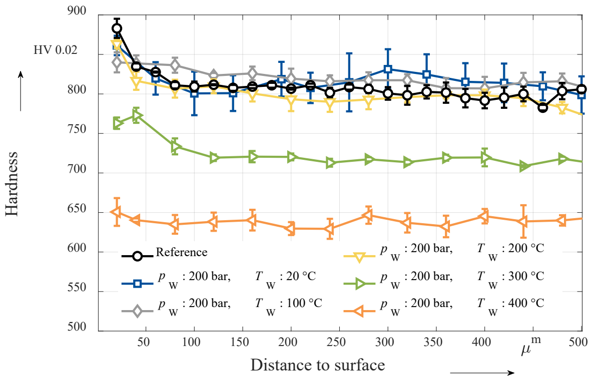

Figure 8: Measured hardness-depth-profiles after deep rolling at different temperatures.

3.2. Residual stress analysis

Figure 9 and 10 show the results of the radiographic residual stress measurement of the deep rolled inner rings at different surface temperatures. Figure 9 shows the measured residual stresses in the circumferential direction, while Figure 10 presents the residual stresses in the axial direction. The measurements were conducted in the middle of the raceway. In both cases the measured profiles show high compressive residual stresses at the surface, which were caused by the honing and grinding processes of the original specimen. Subsequently, the compressive residual stresses decrease briefly before rising again, reaching a maximum at a depth of approximately 100 µm. After this maximum, the compressive residual stresses decrease to zero. No compressive residual stresses are detectable beyond a depth of 350 µm. Additionally, it should be noted that no tensile residual stresses were introduced during the deep rolling process.

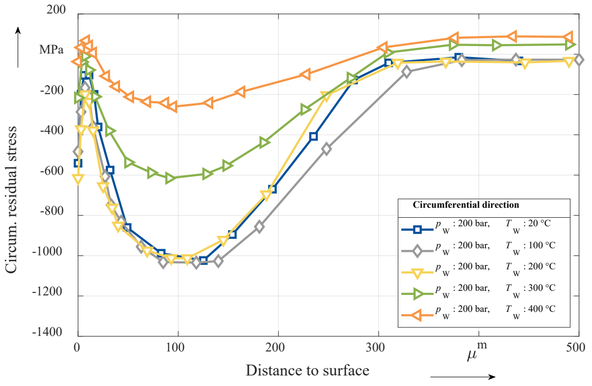

Figure 9: Measured residual stress-depth-profile in circumferential direction.

The residual stress profiles for the deep rolled bearing inner rings show no significant difference in the circumferential direction at temperatures ranging from 20 to 200 °C. It is only at temperatures above 200°C that a noticeable decrease in the maximum introduced compressive residual stress is observed. At a deep rolling temperature of 300°C, the maximum introduced compressive residual stress is reduced by 40%, and at 400°C, it is reduced by 80%. However, the depth of the maximum introduced compressive residual stress does not change compared to lower temperatures.

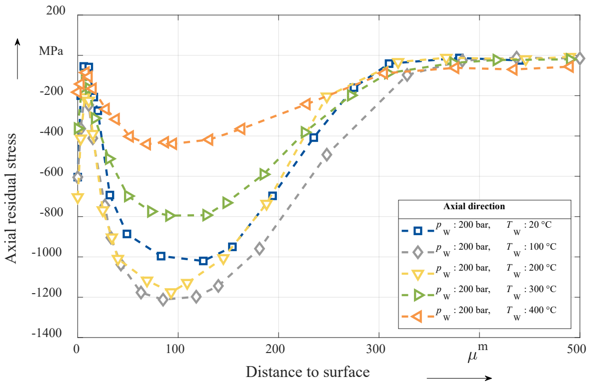

Figure 10: Measured residual stress-depth-profile in axial direction.

The residual stress profiles in the axial direction (see figure 10) are qualitatively similar to those in the circumferential direction (see figure 9). However, it is noteworthy that at 100 and 200 °C, the residual stress profiles exhibit a compressive stress maximum that is 20% higher than the reference value at 20 °C. Figure 11 highlights the measured residual stress profile near the surface at a depth of up to 100 µm.

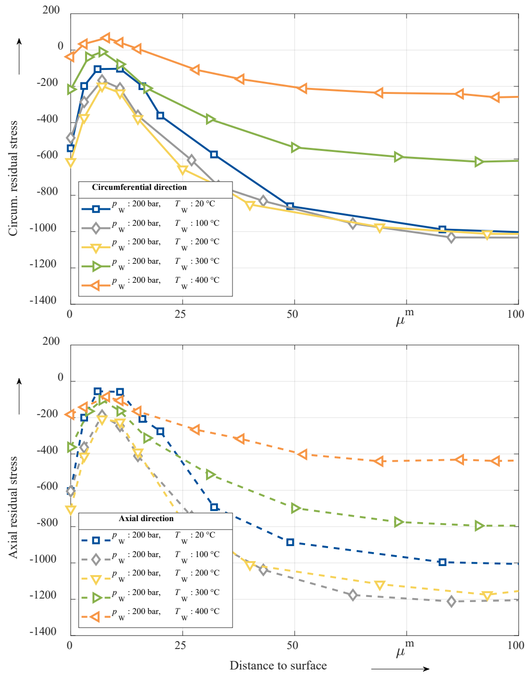

Figure 11: Measured residual stress-depth-profile close to the surface.

This difference is clearly highlighted in Figure 12, which compares the measured residual stress values at a depth of 100 µm in both the circumferential and axial directions. For the reference specimen, deep rolled at 20°C, there is no difference between the axial and circumferential directions. However, at elevated temperatures, a significant difference between the two directions is observed. This may result in a less favorable stress state in the boundary zone, potentially negatively impacting the bearing's fatigue life.

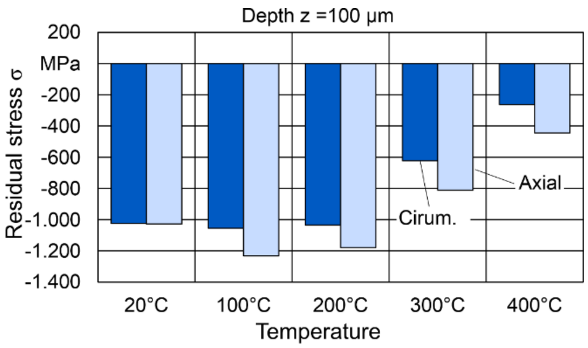

Figure 12: Comparison of the measured circumferential and axial residual stresses at a depth of 100 µm.

3.3. Microstructure

Figure 13 shows the microstructure at different deep rolling temperatures ranging from 100°C to 400°C. The samples were ground, polished, and etched. In all images, the martensitic microstructure is visible. There is no significant difference in microstructure observed with varying temperatures.

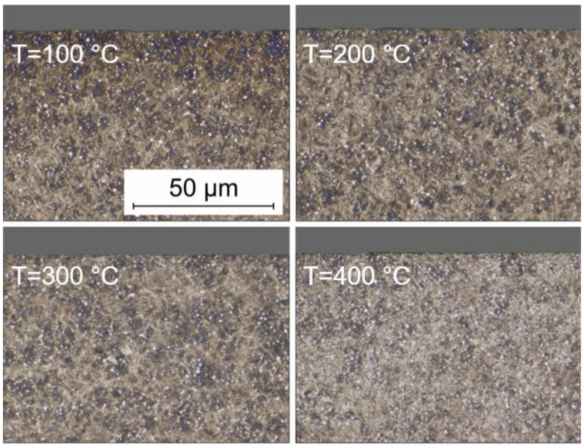

Figure 13: Micrographs of deep rolled inner rings at elevated temperatures.

4. Fatigue tests

To investigate the influence of temperature on the deep rolling process and ultimately optimize the combined process of hard turning and deep rolling, the test plan shown in Figure 14 is implemented.

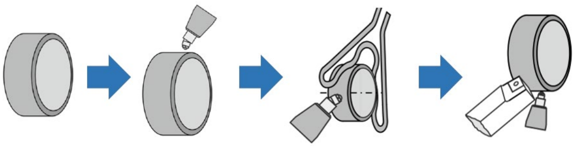

Figure 14: Test plan.

First, reference data are required to compare with the deep rolled samples. Reference bearings with honed and ground surfaces are used for this purpose. In the next step, honed and ground bearings are deep rolled at room temperature (20 °C). This allows for an assessment of the influence of the introduced residual stresses at room temperature, isolating the mechanical component of the combined process. In a third step, bearings are tested with elevated temperatures during the deep rolling process. The effect of temperature can then be compared between step two and step three. The findings can be used in a final step to optimize the actual combined process of hard turning and deep rolling. This report presents the fatigue life tests from the first and second step.

4.1. Test rig and test design

The fatigue life tests were carried out with NU206 cylindrical roller bearings (see figure 4 and table 2). The figure below shows the test rig setup used.

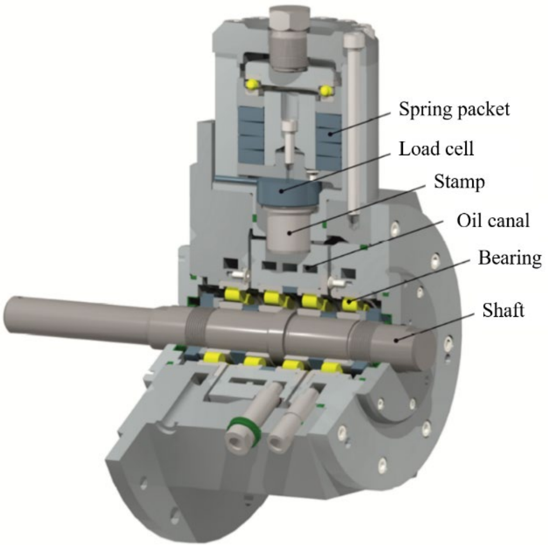

Figure 15: Four-bearing test rig.

The four-bearing design and the use of the sudden death method make it possible to test four bearings simultaneously in one life test. For this purpose, four bearings are operated per test until one bearing fails. The failed bearing is counted as a failure and the other three bearings are included as withdrawals in the Weibull evaluation. The statistical evaluation of the fatigue life tests was performed according to Weibull [11]. Only pitting or spalling damages to the inner ring were evaluated as failures; damages to the outer ring and the rolling elements were included in the evaluation as withdrawals. This is done in order to focus on a defined load situation in the rolling element inner ring contact and only the inner rings were treated with the deep rolling process.

The tests were conducted under a constant load with a load ratio of 4. This resulted in a maximum Hertzian pressure of 2.5 GPa on the inner ring. Full lubrication was maintained at a rotational speed of 4050 rpm and an operating temperature of 51°C. The test parameters are summarized in Table 4.

Table 4: Test parameters.

Load ratio C/P:	4
Max. Hertzian pressure $p_{\max}$:	2.5 GPa
Speed n:	4050 rpm
Operating temperature T:	51 °C
Oil:	Renolin CLP 68
Lubrication:	Full film

Three fatigue life test series were conducted. The first test series (black) serves as the reference. For this series, reference bearings with honed and ground surfaces were used, and no additional processing step or initial residual stress state was introduced before the test. Test series two (red) and three (blue) also used honed and ground bearings, but these were additionally deep rolled at room temperature (20 °C). The difference between test series two and three lies in the deep rolling pressure p_W used. The specific parameters for each test series are detailed in Table 5.

Table 5: Process parameters of the fatigue test samples.

Test series	Surface	Deep rolled	Pressure p_W	Rolling temp. T
1 (black)	honed & ground	no	-	-
2 (red)	honed & ground	yes	400 bar	20 °C (RT)
3 (blue)	honed & ground	yes	200 bar	20 °C (RT)

4.2. Boundary zone characteristics

The measured boundary zone characteristics, such as hardness and residual stress state, of the inner rings used in the test series are shown in figures 15 and 16.

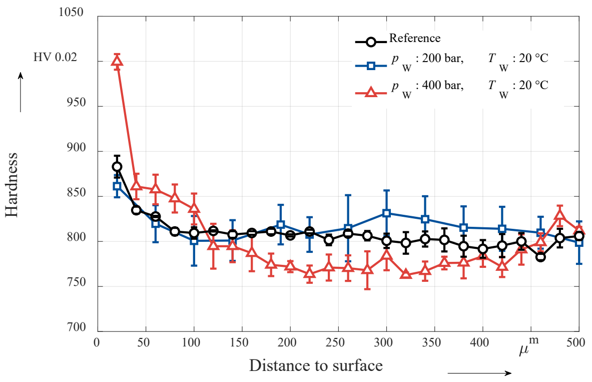

Figure 16: Measured hardness-depth-profiles after deep rolling at room temperature (red) and a reference bearing just honed and ground without deep rolling (black).

As shown in figure 16, there are no significant differences in the hardness depth profiles between the reference bearing and the bearing deep rolled at p_W=400 bar. Differences in hardness values are observed only in the near-surface region.

In contrast, the residual stress states of the samples from the respective test series show significant differences in the initial condition of the fatigue life tests, as seen in figure 17.

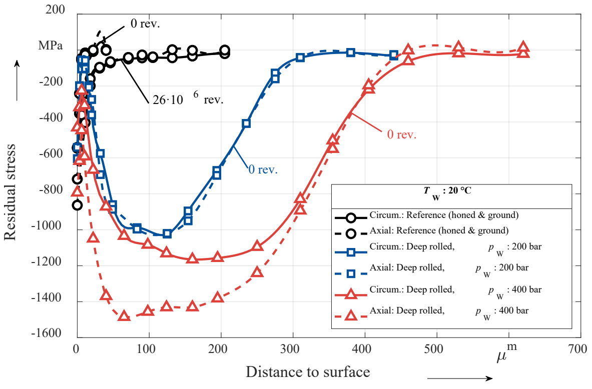

Figure 17: Measured residual stress-depth-profile in circumferential and axial direction.

The initial state of the reference bearing (black) exhibits compressive residual stresses only in the near-surface region, which were introduced by the honing and grinding process. These residual stresses quickly decrease to zero with depth. Further residual stress measurements of the reference bearing after 17 million revolutions at a load ratio of 4 reveal the induced residual stress state. It is evident that the rolling load introduces additional residual stresses into the component, which can influence the resulting stress state. The maximum compressive residual stress is 600 MPa and occurs at a depth of approximately 150 µm.

The additional deep rolling process induced significant initial compressive residual stresses, as evidenced by the red and blue curves. In the second experimental series (red), where the samples were subjected to a rolling pressure of 400 bar, the maximum compressive residual stresses range from 1200 to 1500 MPa. The depth at which these maximum compressive residual stresses occur ranges from 100 to 200 µm. In the third experimental series (blue), where the samples were subjected to a rolling pressure of 200 bar, the maximum compressive residual stresses are 1000 MPa. The depth at which these maximum compressive residual stresses occur is 100 µm.

4.3. Results

The results of the lifetime tests are presented below. Figure 18 displays the Weibull distributions for the three experimental series.

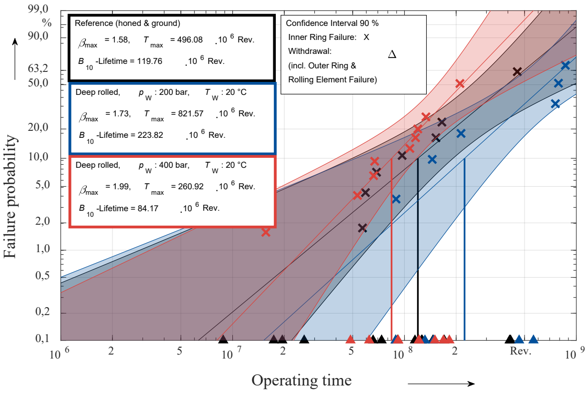

Figure 18: Weibull diagram of the fatigue life tests.

The test series with the reference bearings (black) achieves a fatigue life of 132 million revolutions at a failure probability of 10%. The inner rings of the bearings, which were processed with a rolling pressure of 400 bar (red), achieve a fatigue life of 84 million revolutions. Compared to the reference bearing, the initial residual stress state resulted in a 35% reduction in fatigue life. This suggests that the introduced residual stress state was significantly too high and had a detrimental effect on the fatigue life. Additional effects, such as material embrittlement, may also have played a negative role. At a rolling pressure of 200 bar (blue), the bearings achieve a fatigue life of 223 million revolutions. This represents a 75% increase in fatigue life. This suggests that the initially introduced residual stress state was beneficial for the stress conditions in the boundary zone of the bearing inner ring.

Table 6 summarizes the key results of the fatigue life tests.

Table 6: Fatigue life test results.

Test series	Load ratio *C*/*P*	Pressure p_W	Rolling temp. *T*	Exp. life time B_{10}
1 (black)	4	-	-	132 mio. rev.
2 (red)	4	400 bar	20 °C (RT)	84 mio. rev.
3 (blue)	4	200 bar	20 °C (RT)	233 mio. rev.

It should be noted that the confidence intervals exhibit a substantial overlap. To make well-founded statements, additional experiments are necessary. However, a clear trend can be observed from the experiments. An initial compressive residual stress state can enhance the fatigue life of a bearing. However, it is important to note that this initial compressive residual stress state has an optimum. Exceeding this optimum, particularly due to an excessively high residual stress state, can lead to negative effects on fatigue life.

5. Conclusions and outlook

The results of the material analysis have shown that thermal effects play a significant role in the deep rolling process and cannot be overlooked in the hard turning and deep rolling process. Both hardness and residual stress states are substantially influenced by thermal input into the component. Especially temperatures above 200 °C lead to a significant reduction in both hardness and the residual compressive stresses. These findings provide a better understanding of the interactions between thermal and mechanical effects and offer a basis for future research and development.

The fatigue life tests show that excessively high residual compressive stresses introduced by deep rolling can be detrimental to fatigue life. By reducing the introduced compressive residual stresses, higher fatigue lives can be achieved compared to bearings that are only honed and ground. This indicates that there is an optimal initial residual stress state.

Further lifetime tests that account for the thermal influence during the deep rolling process are necessary. The results will enable the optimization of the combined process of hard turning and deep rolling. The resulting bearing inner rings must be subjected to a final series of tests to evaluate their fatigue life.

Acknowledgment

The German Research Foundation (DFG) funded the presented investigations. We thank the DFG for its support and funding of the project “Functionalized subsurface for load-oriented fatigue behavior of hardened components” (BR 2967/28-1, PO-675/22-1 and PA-3279/8-1).

References

[1] B. Breidenstein, Oberflächen und Randzonen hoch belastbarer Bauteile, Habilitationsschrift, Tewiss, Leibniz Universität Hannover, 2011.

[2] E. Brinksmeier, J.T. Cammett, W, König P. Leskovar, J. Peters, H.K. Tönshoff, Residual stresses – measurement and causes in machining processes, CIRP Annals-Manufacturing Technology 31 (1982) 491-510.

[3] E. Brinksmeier, Prozeß- und Werkstückqualität in der Feinbearbeitung, Habilitationsschrift, Hannover, VDI Düsseldorf, 1991.

[4] K.H. Kloos, Über die Bedeutung der Oberflächen- und Randschichteigenschaften für die Bauteilhaltbarkeit, VDI - Berichte, 506 (1984) 1-14.

[5] D. Radaj, M. Vormwald, Ermüdungsfestigkeit – Grundlagen für Ingenieure, Dordrecht, Springer, Berlin, 2007.

[6] A. Sollich, Verbesserung des Dauerschwingverhaltens hochfester Stähle durch gezielte Eigenspannungserzeugung, Fortschrittsberichte VDI, 5 (376), VDI-Verlag, Düsseldorf, 1994.

[7] M. Habschied, B. de Graaff, A. Klumpp, V. Schulze, Fertigung und Eigenspannungen, HTM Journal of Heat Treatment and Materials 70(3) (2018) 111-121.

[8] F. Klocke, W. König, Fertigungsverfahren 1 – Drehen, Fräsen, Bohren, 8. Edition, Springer, Berlin, 2008.

[9] K. Röttger, G. Wilcke, S. Mader, Festwalzen - eine Technologie für effizienten Leichtbau, Materialwissenschaft und Werkstofftechnik 36 (6) (2005) 270-274.

[10] B. Denkena, G. Poll, O. Maiß, T Neubauer, Affecting the Life Time of Roller Bearings by an Optimal Surface Integrity Design After Hard Turning and Deep Rolling, Advanced Material Research 967 (2014) 425 – 434.

[11] DIN EN 61649: März 2009, Weibull Analyse